Transport of Fast Ions through Solid and Clusters under Intense Laser Pulses: Interaction dynamics probed by X-ray spectroscopy

Emily Lamour

To cite this version:

Emily Lamour. Transport of Fast Ions through Solid and Clusters under Intense Laser Pulses: Interaction dynamics probed by X-ray spectroscopy. Atomic Physics [physics.atom-ph]. Université Pierre et Marie Curie, 2012. tel-01103310

HAL Id: tel-01103310
https://hal.science/tel-01103310

Submitted on 14 Jan 2015

Habilitation à diriger des recherches

Sorbonne Université Pierre et Marie Curie

Emily LAMOUR

Maître de Conférences

Transport of Fast Ions through Solid and Clusters under Intense Laser Pulses: Interaction dynamics probed by X-ray spectroscopy.

Soutenance prévue le 10 décembre 2012

Composition du jury

Henri BACHAU (CELIA)	Directeur de Recherche CNRS	Rapporteur
François De OLIVEIRA SANTOS (GANIL)	Chargé de Recherche CNRS	
Alain DUBOIS (LCPMR)	Professeur UPMC	
Sylvie JACQUEMOT (LULI)	Directeur de Recherche CEA	
Roberto RIVAROLA (INSTITUTO de FISICA)	Professeur (ROSARIO, Argentina)	Rapporteur
Gregor SCHIWIETZ (Helmholtz-Zentrum)	Professeur (BERLIN, Germany)	Rapporteur

CONTENTS

INTRODUCTION

I have started my life of researcher in studying the production and transport of Rydberg states in fast ion-solid interaction. What can be more fascinating that the creation and transport of a Rydberg state with a diameter of typically a few tens of Å in an environment as unfriendly as a solid (with a thickness of a few hundred of Å)?… A lot of other points… and, among them, the ones briefly presented in this manuscript for which I had luck to perform studies with wonderful people. The studies are all related to the understanding of the electronic response of matter submitted to a strong perturbation. **The perturbation is here induced by either fast highly charged ions (HCI) or intense and short laser pulses.**

When studying the interaction between a fast heavy ion projectile and a solid target, we can be interested either by the target itself (for instance, the formation of tracks in insulating materials) or by what happens to the ion. These different studies are obviously strongly connected. In our group, we mainly concentrate on the transport of electrons in ion excited states. Two extreme representations may be used to evaluate, especially, the electronic ion stopping in matter. These two aspects are linked to the response of the target electrons:

- In the first picture, the solid is seen as an assembly of atoms and the HCIs undergo a series of binary ion-atom collisions with the target electrons. This ***pure collisional approach*** has been used in the Bethe theory [1] to calculate the ion stopping power (more details can be found in [2] and [3]). The ensemble of ion-atom cross sections forms the database of any theoretical treatment.
- In the other picture, closer in spirit to the dielectric theory first proposed by Bohr [4], the target electrons are considered to ***respond collectively*** to the passage of the projectile. The HCIs induce a polarization of the medium described as a wake of electronic density fluctuation trailing the ion, the so-called ***wake field***. The gradient of the wake potential leads to the establishment of an electric field, and its local value at the projectile can be used to calculate the stopping power ([5], [6], [7]). Its value can be as high as that of the electric field experienced by an electron on the first Bohr orbit, i.e., 5.4 10^9 V/cm.

Both types of calculations appear to achieve good agreement with stopping power measurements, despite a rather different physical picture for the behavior of the target electrons. It is clear that the response of the target electrons to the passage of the ion has direct consequences on the projectile ion: it is slowed down, but not only, the populations in its excited states are also altered by the presence of the environment (the solid). Notably, the presence of the wake field may mix the ion excited states by Stark effect in a coherent manner while a pure collisional response of target electrons destroys any coherence. Hence, the group tackled the study of the production and transport of projectile excited states. The analysis of the de-excitation of these excited states allow us to probe the solid response

For that, we have chosen:

- for the projectile: i) ions in the MeV/u range fast enough to consider only the electronic stopping power (i.e., the nuclear stopping power is negligible); ii) highly charged ions to induce a strong electron density fluctuation and, consequently, a strong wake field and iii) ions with only one electron for which the excited states and their coupling are well known;
- for the targets: solids easy to produce in thin films and for which the thickness can be varied over a few order of magnitude. For the thinner target, we want to reach the single collision condition giving rise to an ultra-short ion transit time inside the solid (< 1 fs). We choose the thicker target to get the equilibrium in the ion populations (ion transit time of a few 10 fs).

The theoretical description of this interaction has been a real challenge. We have developed several methods: one classical simulation based on a stochastic approach of the ion transport and two quantum simulations implying either the resolution of the stochastic time-dependent Schrödinger equation or master equations as “rate”-like equations.

High values of electric field are also reachable with intense laser pulses inducing also a strong perturbation in the matter. Laser excitation/ionization of nanometer-sized atomic clusters offers opportunity to explore ultrafast many particle dynamics. Indeed, submitted to strong optical fields, the response of free clusters is often very different from that of single atoms/molecules. Large clusters, similarly to solids, couple very efficiently to intense sub-picosecond laser pulses. Near 100 % of the laser radiation can be absorbed giving rise to the observation of highly charged ions with energies reaching MeV [8] and warm electrons with a fraction having keV energies [9]. Another fascinating feature of this interaction is its efficiency for converting photons in the eV range to X-rays with keV energies. This emission is due to the de-excitation of HCIs having inner shell vacancies ([10], [11], [12]). The lifetime of these excited states being very short (down to some fs), their observation gives access to the dynamical evolution of the irradiated cluster on a time scale comparable to that of the laser pulse duration. Our group has performed several experiments to measure the evolution of absolute photon yields and charge state distributions of the emitting ions with different physical parameters governing the interaction; namely intensity, polarization, pulse duration and wavelength of the laser as well as the size of the clusters. These various studies have allowed us to determine the ionization mechanisms in inner shells and their time competition. In this manuscript, I only present the influence of the laser intensity.

Cluster dynamics comprises also a large span of time scales, making their theoretical description a great challenge. Even if at first glance, such dynamics may be seemed very different from that of the ion-solid interaction, it turns out that a description developed for the ion-solid interaction may also be used to model the laser-cluster interaction so as to predict absolute X-ray yields.

In both cases, we have used X-ray spectroscopy techniques to record the de-excitation of excited states of HCIs. In Table 0-1, I just mention some time characteristics to fix the similarities between these two interactions.

Fast (a few MeV/u) highly charged ions in a thin amorphous solid	***Intense laser pulses (800 nm, ≤100 mJ/pulse) irradiating nanometer sized atomic clusters***
Ion transit time: ≤ a few 10 fs (with solid thicknesses between 100 Å and 1 µm)	Pulse duration: ≥ 50 fs Optical cycle: 2.7 fs
Wake field period: a few 0.1 fs	Plasma period: 0.1 – 1 fs
Lifetimes of HCI excited states: $\sim 1.6\ 10^6/Z^4$ (in fs) $\Rightarrow$ for 2p state: 15 fs in argon, 1 fs in krypton	Lifetimes of HCI excited states: 15 fs for the Ar 2p state (only results with argon clusters are presented)
Creation of ion tracks [13]: > 100 fs	Explosion of the heated clusters: ≥ a few 100 fs

Table 0-1: A few characteristics of ion-solid and laser-cluster interactions

I first start this manuscript by describing the context of the studies I performed during the last ten years. In other words, I try to present what the state-of-art was and the questions raised at that time §1. Then, I list the main processes and give the arguments that made us to choose the most appropriate collision systems to be studied §2. The experimental conditions are described in §3: the large scale facilities we used, the various targets, the set-ups, followed by a presentation of typical spectra obtained either with low resolution X-ray detectors or with high-resolution high-transmission X-ray spectrometers (§4). The principles of theoretical approaches are given in §5 while the main results are presented in §6. After a conclusion, I present in the last section the Fast Ion – Slow Ion Collisions (FISIC) project which is part of the S3 Equipex (equipment of excellence for Super Separator Spectrometer) managed by GANIL (Grand Accélérateur National d'Ions Lourds de Caen).

1. CONTEXT OF THE STUDIES DESCRIBED IN THIS MANUSCRIPT

1.1 ION-MATTER INTERACTION

In this sub-section I would like enlighten the reader on the relative importance of the electronic processes occurring during an atomic collision in each collision domain. Then I briefly present the context of the studies detailed in this manuscript. Finally, I end up by mentioning the theories used in our simulations to describe the electronic processes.

1.1.1 DEFINITION OF COLLISION REGIMES

The ion-atom interaction is the first step in the understanding of the ion- matter interaction. The cross sections of mono-electronic processes occurring during the collisions of an ion with an atom such as ionization, excitation and capture (Figure 1.1) depend on the collision velocity and on the asymmetry of the collision system. An example is given Figure 1.2 for the simplest three-body collision system: proton on hydrogen.

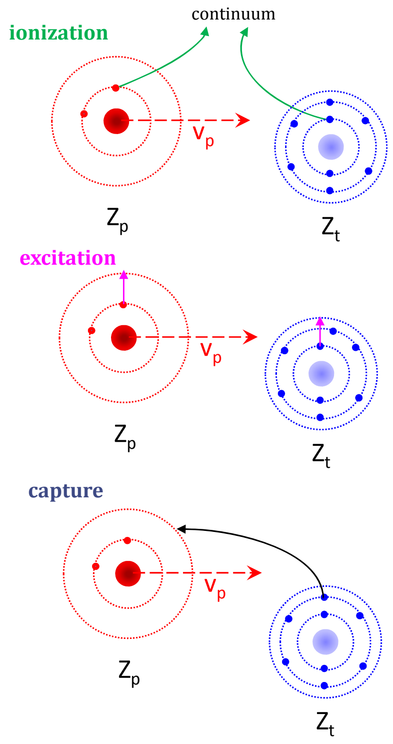

Figure 1.1: Electronic atomic processes.

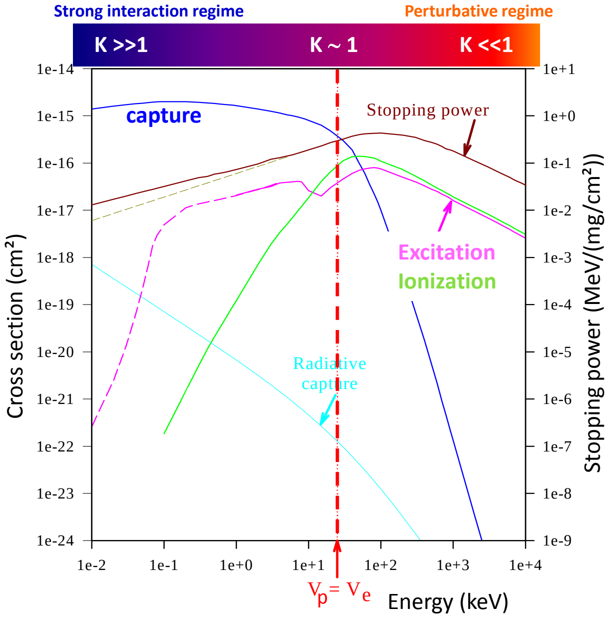

Figure 1.2: Cross sections of elementary atomic collision processes for the system p→ H. The vertical red dotted line indicates the proton energy where its velocity equals the hydrogen electron velocity. The brown line is the stopping power (refer to the right y-axis) for protons in aluminum.

More precisely, we define a parameter K (here for the **projectile** electrons) to distinguish, in fact, three different collision regimes.

Eq. 1

$$K = \frac{Z_t}{Z_p} \times \frac{v_e}{v_p}$$

where Z_t and Z_p stand for the atomic numbers of the target and the projectile, respectively. v_e is the velocity of the active electron while v_p is the projectile velocity.

- The **strong interaction regime (K >> 1)**, often called the “low velocity regime”, is reached for projectile velocities well below the velocity of the active electron when the atomic numbers of the target and projectile are comparable, or for a strong collision asymmetry $Z_t \gg Z_p$. For this regime, the capture process is largely dominant compared to other processes. The well-known classical over-barrier (COB) model [14] and more sophisticated coupled state calculations using basis of either atomic or molecular orbitals [15] [16] [17] provide good predictions of cross sections. The capture of a target electron by a projectile is selective and takes place in a level of high principal quantum number n. Typical values of cross sections around 10^{-15} cm^2 are reached [18].

- The **perturbative regime (K << 1)** is reached for high projectile velocities or when $Z_p \gg Z_t$. In this regime, ionization and excitation have cross sections much larger than capture. Approximate scaling laws can be deduced from perturbative calculations to predict those cross sections σ (§1.1.3):

  For *capture*, when assuming the capture of a target electron by the projectile, we have roughly:
  - $\sigma \propto Z_p^5/v_p^{11}$ and $\sigma \propto Z_t^{4 \text{ or } 5}$
  - for a given collision system: $\sigma \propto 1/\mathrm{n}^3$ from n = 2 with a distribution for which the p (ℓ=1) states are preferentially populated.

  For *ionization/excitation*, when assuming the ionization/excitation of one target electron by a bare projectile, we have roughly:
  - $\sigma \propto Z_p^2$ and $\sigma \propto \mathrm{n}^4/Z_t^4$
  - $\sigma \propto \ln(v_p)/v_p$
- For **the intermediate regime** (**K ~ 1**), the cross sections of the mono-electronic processes are close to their maximum and are all of the same order of magnitude. Multiple processes such as capture-ionization, excitation-ionization, double excitation… have then non-negligible probabilities compared to single processes. The role of the electron-electron interaction and coupling between different collision channels are then crucial. The FISIC project presented in the last section is dedicated to the study of ion-ion collisions in this velocity regime.

1.1.2 *CONTEXT IN THE PERTURBATIVE REGIME*

In the 70's, it was recognized that significant differences in the measurement of cross sections in gaseous targets and solid foils could arise from multiple collision phenomena (Betz et al [19]). Since all cross sections decrease when increasing the velocity in the perturbative regime, it was expected that theses multiple collision processes should vanish. In the 80's, the various works dedicated to the interaction of fast ions with solids have revealed some features remaining significantly different from the ion-atom interaction: for instance, the observation of "anomalous" np populations of deeply bound states (work of Rozet *et al* [20]) as well as the formation of Rydberg states and convoy electrons (work of Betz *et al* [21], [22]). In the following, I first present some studies related to the core states of the fast projectile ion while the second part is dedicated to the Rydberg states.

a) Core states of the ion projectile:

Control of the highly charged ion production after passing through solids is of great interest, especially, for optimizing the operation of accelerators. The group was (and is still) very interested in the study of the evolution of the ion charge state with the solid thickness, usually named the stripper. For that purpose, the group has developed a code named ETACHA that is based on a set of coupled differential rate equations using ion-atom cross sections for capture, ionization and excitation processes. Radiative and Auger de-excitations are included as well. It is worthwhile mentioning that charge state distributions are sensitive to gain/loss of electrons in given nℓ level. For highly stripped ions of high energy, a two-shell model (n= 1 and 2) was first developed [23]. In 1996, an extension to up to 28 electrons (shells with n = 1, 2, 3) has been performed allowing to consider ions such as 30 MeV/u Pb^{56+} as delivered by GANIL [24]. Today, ions up to 60 electrons can be considered involving 1283 coupled differential equations. Using perturbative treatments to calculate *ion-atom cross sections*, this code well suited for the so-called high velocity regime provides relevant predictions of ion charge distributions with the stripper thickness and, in particular, the fractions of the less dominant charge states as well as the evolution of the charge state distribution with very thin strippers (i.e., out of equilibrium). If now we are interested in observables more sensitive to the solid environment, differences between solid and gaseous targets occur. By studying the evolution of the relative Lyman intensities emitted by 33.2 MeV/u Kr^{35+} ions as a function of the target atomic number, Rozet and co-workers have shown an increase of the Lyman α intensity in the case of solids [20] as illustrated in Figure 1.3. For this study, the Kr^{35+} ions are initially populated by the single capture process and the single collision condition (§2.1.2) with respect to this process is fulfilled whatever the target (atomic or solid). As a result, one may wonder what happens inside a solid.

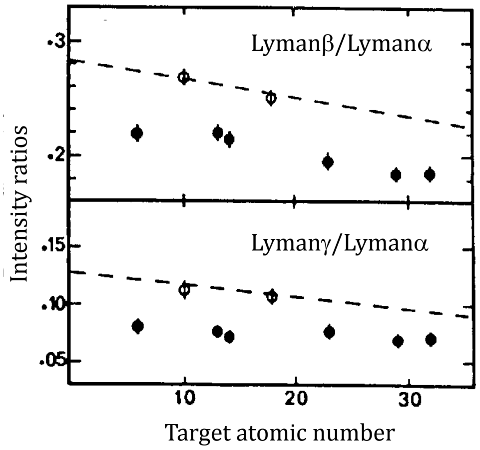

Figure 1.3: Relative intensities of Lyman α, β, and γ lines as a function of the target atomic number [20] for 33.2 MeV/u Kr^{35+} ions initially populated by the single capture process. Black symbols are for solid targets while white symbols are for atomic targets. Broken line is from CDW calculations (see §1.1.3).

Studies of the relative intensity of each Lyman transition were then carried out for the same collision system as a function of the solid thickness. In order to compare to the value obtained with atomic target, the considered Lyman intensity relative to the total Lyman intensity is normalized to this gas value. In Figure 1.4, I have reported two sets of experimental data obtained by the group and issued from Nicolaï *et al* [25] and the PhD thesis of I. Despiney [26]. The experimental data depart significantly from the gas value exhibiting a strong influence of the solid environment. A rate equation model corresponding to a statistical description of the binary ion-atom collisions inside the solid has then been built up (information can be found in [25] and in my PhD thesis [27]). It governs the evolution of the $n\ell$ ion populations through a set of coupled differential equations exactly as the ETACHA code. In the present case discussed here (Kr^{35+} at 33.2 MeV/u on carbon), each $n\ell$ state up to $n = 10$ evolves thanks to collisional processes as ionization and excitation (additionally to the radiative decay). In Figure 1.4, the inter-shell excitation was neglected for $n > 4$ as well as the non dipolar intra-shell excitation (i.e., the $n\ell \rightarrow n\ell' \neq \ell\pm1$ cross sections). One way to reproduce the experimental evolution is to artificially increase the $n\ell \rightarrow n\ell' = \ell\pm1$ cross sections.

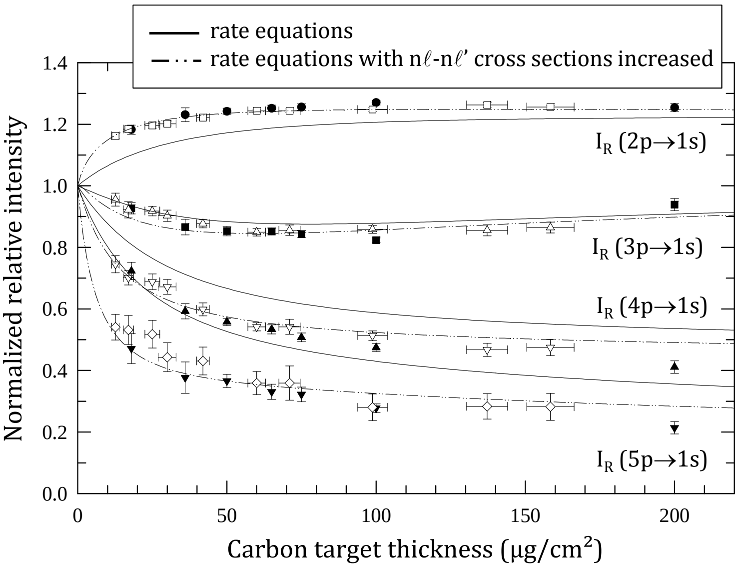

Figure 1.4: Normalized relative intensities of Lyman lines as a function of target thickness for the collision system Kr^{36+} at 33.2 MeV/u on carbon. The value "1" corresponds to the gaseous value. Experiment is given as points with error bars: back symbols for the data from [25] and white symbols from [28](i.e., Despiney's PhD thesis [26]). The full curves correspond to predictions from the rate equation model (see text) when using ion-atom cross sections calculated with PWBA (see §1.1.3). The double dashed curve is obtained by increasing the intra-shell excitation cross sections to fit the predictions to the experimental data.

In §5.2.1, an improved version of the rate equation model is presented including the missing cross sections. Nevertheless, this pure collisional approach could not account for the evolution of the $n\ell_j$ fine structure populations as observed by Despiney [26] and the collective response of the target electrons was then considered. The group has first developed a simple two-state model (see Vernhet *et al* [29] and Rozet *et al* [30]) where only the Stark mixing induced by the wake field is accounted for revealing its crucial role in the evolution of the $3\ell_j$ sublevel intensities for Kr^{35+} at 33.2 MeV/u ions on carbon foils initially populated by capture. From there, we have developed a more complete model named the Master Equation Approach and presented in this manuscript (§5.2.1). This new approach is part of the PhD thesis of C. Fourment [31] performed in our group (2000). With the group of J. Burgdörfer, we have participated to the elaboration of another theoretical method based on quantum Monte Carlo calculations (§5.2.2) and detailed in the PhD thesis of M. Seliger [32] (2005). In the following, I present also experimental data obtained for two additional collision systems: Kr^{35+} at 60 MeV/u (populated initially by the *single excitation* process) and Ar^{18+} at 13.6 MeV/u (populated initially by the *single capture* process) on carbon foils.

b) Rydberg states of the ion projectile:

In beam-foil experiments, the study of the delayed photon emission of short lifetime excited states (as 2p or 3p for hydrogen-like ions) is one important tool for investigating Rydberg states emerging from solid (see Figure 1.5). It has been observed that the intensity of the delayed emission of short lifetime np states (n = 2 or 3) decreases with the ion time of flight behind the solid as $I(t) \propto t^{-a}$ with $t \gg \tau_{n\ell}$ [33]; $\tau_{n\ell}$ being the radiative decay time of the 2p or 3p state. This behavior is caused by cascades from excited states with high n and ℓ quantum numbers mainly via the Yrast cascade. This contrasts sharply with the primary binary ion-atom collision (here the capture) at similar high collision velocities in which small ℓ values (mainly 0 and 1) are populated. Due to the large orbital size of Rydberg states (proportional to n^2), it was claimed that these states were produced by capture in the last layer of atoms in the solid (just when the ion exits into vacuum). Betz *et al* [21] have demonstrated that this process could not explain the observed ℓ-populations. Later on, Kemmler and co-workers suggested that the production of ℓ-Rydberg-state populations for the collision system O^{2+} (v_p = 9 a.u.) on a carbon foil of 20 µg/cm^2 could be interpreted by transport of projectile electrons through multiple scattering effects ([34] and references therein). However, in that case, the understanding of the projectile electron transport was far to be clear since:

i) capture of the target electron and excitation or ionization of the 1s projectile initial state are of the same order of magnitude. Thus, different processes are involved in the “primary” production of excited states and those processes are also involved in the transport phase making the distinction between the “initial” excited-state population and transport effects impossible.

ii) the target was thick enough to reach equilibrium for the charge-state distribution and the use of only one target thickness restricted the possibility to really test the transport effects.

We have then performed a systematic experimental study of the delayed photon emission with the ion time of flight and, this, for a range of target thickness from single-collision conditions (for which in average only one collision occurs in the solid) to equilibrium (regime reached when the ion populations do not evolve anymore). In parallel, simulations based on Monte Carlo methods have been developed to test the influence of the collisional processes but also the sensitivity of the population of long-lifetime states to the wake field during the transport. This work is part of my PhD thesis and also the result of collaboration with B. Gervais (CIMAP, Caen).

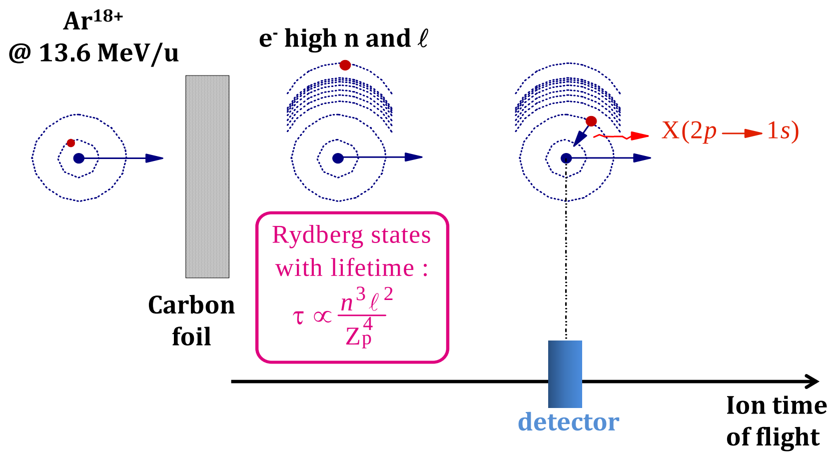

Figure 1.5: Principle of a beam-foil experiment. The detection system can be moved.

1.1.3 THEORIES USED IN THE PERTURBATIVE REGIME FOR THE CAPTURE AND EXCITATION/IONIZATION PROCESSES

For a given quantum system, when we know only the probability distribution to be in a particular state, this system is described by the density operator ρ, also called the density matrix, and not by a wave function. Hence, when dealing with state mixing processes, as we do in ion-matter interaction, any system has to be represented, after the collision, by the density matrix whose diagonal elements are named *populations* while off-diagonal elements are *coherences*.

Common approaches to treat the capture process are the continuum distorted wave (CDW) approximation ([35] and references therein) and the classical transport Monte Carlo method ([36], [37]). Experiment shows that CDW and CTMC results agree reasonably well for charge transfer in many ion-atom collision systems regarding the total and n-level resolved cross sections for the dominant channels but, typically, do not agree for ℓ-resolved cross sections: for instance, CTMC predicts a population in p states twice as large than CDW in the case of the capture of a 1s carbon electron from a bare argon at 23 a.u.. The situation is even less clear for coherences, i.e., off-diagonal elements of the density matrix. Therefore, a benchmark calculation by employing a three dimensional lattice time-dependent Schrödinger equation (LTDSE) approach has been performed ([38] and references therein, [39]). For the states within the $n \leq 3$ manifolds, the LTDSE results lie in between those from CDW and CTMC, with CTMC practically always above LTDSE and CDW always below (see Figure 1.6). These three approaches reasonably agree for the relative magnitudes and phases of coherences, nevertheless we have again the LTDSE results lying generally between those of CTMC and CDW and more closely to CDW than to CTMC. These three approaches have been used to evaluate the initial density matrix and have been tested in the case of the capture of a 1s carbon electron by a bare argon ion at v_p = 23 a.u.. This is the primary population process also named the source term in the study of the Ar^{17+} excited state transport.

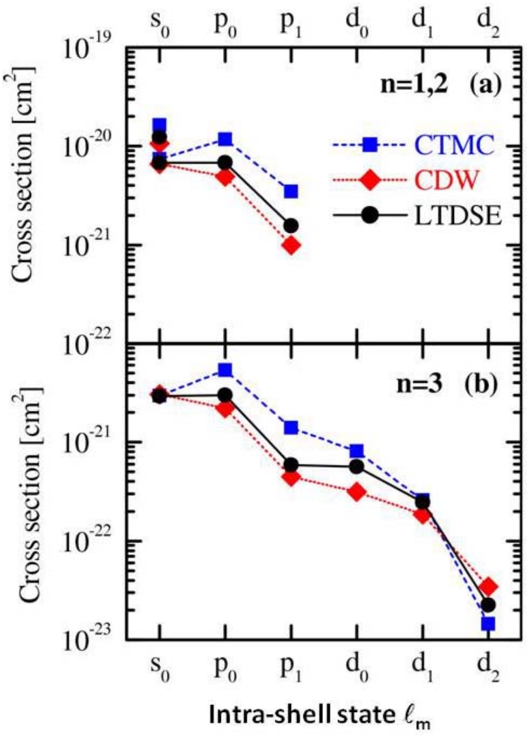

Figure 1.6: State selective charge transfer cross sections computed using the LTDSE, CDW, and CTMC approaches (see text) for Ar^{18+} on C at a projectile velocity of 23 a.u. for different shells: n=1, n=2(a) and n=3 (b).

For the excitation and ionization processes, we have used the Plane Wave Born Approximation (PWBA, [40] and references therein) to calculate the cross sections by taking into account the screening and anti-screening effects. Indeed, the role of the other electrons during the ion-atom collision (modeled by a mean field) affects the cross sections through two contributions: i) the passive role of electrons that screen the perturbative potential (screening effect) and ii) the ionization/excitation processes directly generated by electron-electron interaction (anti-screening effect) [41]. The screening effect reduces the cross sections while the anti-screening increases them. Some processes, such as intra-shell excitation, are very sensitive to these effects leading, in this case, to a saturation with the principal quantum number n as it is illustrated in Figure 1.7 for Ar^{17+} at v_p = 23 a.u. on carbon. The 1s → nℓ excitation process is the primary population process in the study of the Kr^{35+} (v_p = 47 a.u.) excited state transport. The single excitation process is "easier" to describe theoretically than the capture because the active electron remains linked to his parent center. In Figure 1.8, PWBA calculations are presented for 1s → 2ℓ, 3ℓ, 4ℓ showing that the screening and anti-screening effects are negligible for the present case. Close coupling calculations [42] have been also used to describe the initial density matrix giving very similar predictions and proving the reliability of calculations. The very good knowledge of the primary density matrix, in this case, allows testing only the transport phase itself in our simulations.

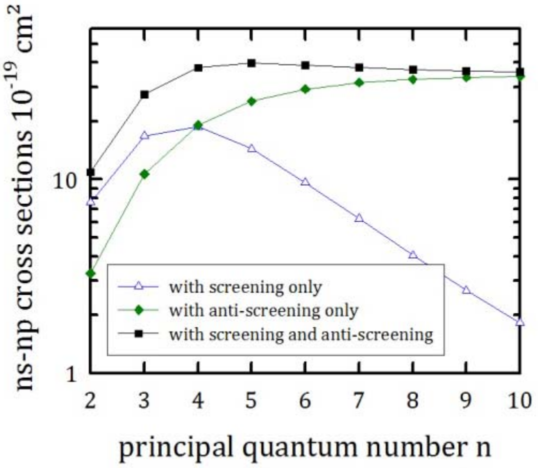

Figure 1.7: Intra-shell ns-np excitation cross sections of Ar^{17+} (v_p = 23 a.u.) with PWBA calculations.

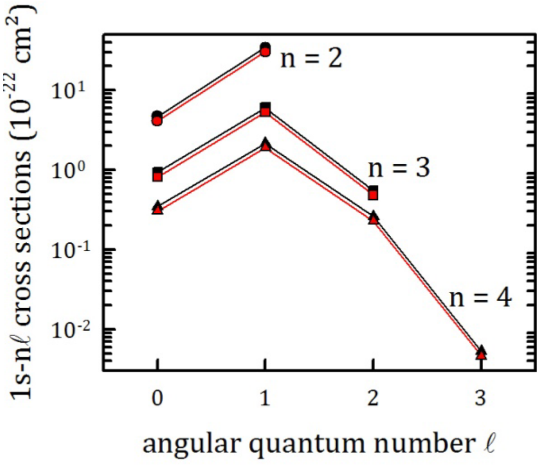

Figure 1.8: 1s→nℓ excitation cross sections for Kr^{35+} at 47 a.u. using PWBA: black lines with screening and anti-screening and red lines without any of those effects included.

1.2 LASER-CLUSTER INTERACTION

For a large overview on the laser-cluster interaction, I recommend the following review papers: "*Mechanisms of cluster ionization in strong laser pulses*" from Saalmann and co-workers [43] and "*Laser-driven nonlinear cluster dynamics*" from Fennel and co-workers [44]. In the following I only present a few results linked to the emission of hard X-rays coming from the de-excitation of highly charged ions produced during the laser-cluster interaction so as to give the context of the results presented in this manuscript.

1.2.1 PRODUCTION OF HIGHLY CHARGED IONS

As mentioned in the introduction, the experiments using ion spectroscopy techniques have revealed the production of highly charges ions (HCI). For instance, high energy xenon ions (100 keV) with a mean charge state between 18+ and 25+ have been observed at a laser intensity of 2 10^{16}W/cm^2 [45] (with a small fraction of ions having even a charge state of 40+). In the case of argon clusters irradiated by pulses of the same laser intensity, ions with a charge state up to 14+ have been observed with a distribution centered around 8+[46] (see [47] for additional results). It is then interesting to compare these ion charge state distributions with what can be measured in X-ray spectroscopy, provided that the identification of spectroscopic transitions is correct. In the case of xenon clusters with laser intensities from a few 10^{16} W/cm^2 up to 10^{19} W/cm^2, 4 – 5 keV X_L photons issued from the de-excitation of excited $Xe^{q}+$ ions have been measured (Figure 1.9 and Figure 1.10). In [10], the authors have assigned the two group of lines (Figure 1.9) to 3d → 2p transitions in multi-charged Xe ions with either one vacancy in 2p shell ($2p^{-1}$) or two vacancies in 2p ($2p^{-2}$). We have also irradiated xenon clusters (see Figure 1.10) at lower laser intensities and recorded spectra having the same shape. Nevertheless, multi-configuration Dirac–Fock calculations contradict the previous analysis. Indeed, they show that the energy splitting between the two main lines (~ 320 eV, i.e., 0.20 Å) is due to the relativistic splitting between $3d_{5/2} \rightarrow 2p_{3/2}$ and $3d_{3/2} \rightarrow 2p_{1/2}$ transitions in multi-charged (24+ to 32+) Xe ions with only one shell vacancy [48].

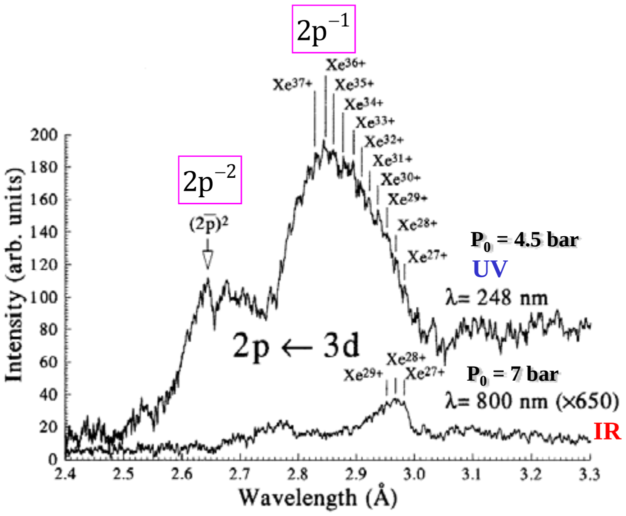

Figure 1.9: Comparative Xe(L) spectra observed by irradiation of Xe clusters with wavelengths of 248 nm (at 10^{19} W/cm^2) and 800 nm (at 1.4 10^{18} W/cm^2). The positions of the Xe^{q+} charge states are indicated by the authors [10]. The location of the "supposed" (see text) double 2p vacancy species ($2p^{-2}$) is shown on the upper curve.

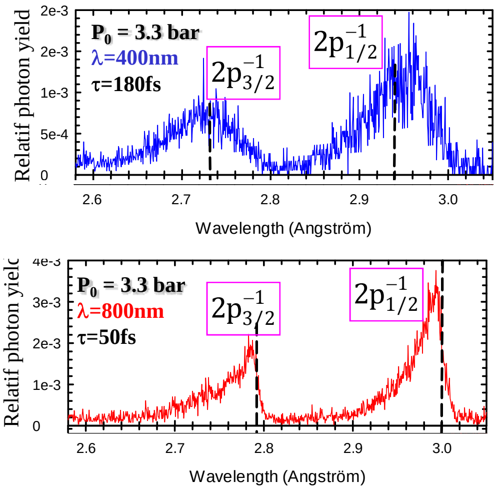

Figure 1.10: Comparative Xe(L) spectra observed by irradiation of Xe clusters with wavelengths of 400 nm (at 8 10^{15} W/cm^2) and 800 nm (at 3.4 10^{16} W/cm^2). The two broad peaks corresponds to 3d → 2p transitions in highly charged Xe^{q+} ions ($24 \leq q \leq 32$) with only one 2p ($2p_{1/2}$ or $2p_{3/2}$) vacancy [48].

With argon clusters, the assignment of the spectroscopic lines is much easier. The observed ~ 3 keV X-rays are emitted by highly charged argon from Ar^{12+} to Ar^{16+} with a K shell vacancy ([12], [49], [50]). The transition lines are well identified and, consequently, the charge state of emitting ions. In Figure 1.11 an example is given with argon clusters irradiated by 790 nm laser pulses of 5 10^{17}W/cm^2. These charge states are also produced when using lower laser intensities as shown in §4.2. With those two examples (xenon and argon clusters), we may note that highest charge states are observed when X-ray diagnostics are used compared to the charge states measured by ion spectroscopy. In fact, the de-excitation of ionic species responsible for the X-ray emission occurs on time scale down to some fs (see §**Erreur ! Source du renvoi introuvable.**). As a result, its study provides a direct insight into the early evolution of heated clusters. In the case of ion spectroscopy information is recorded on a µs time scale and electronic recombination processes can play a role, after the laser pulse and the cluster disintegration; this explains the slightly lowest charge state production.

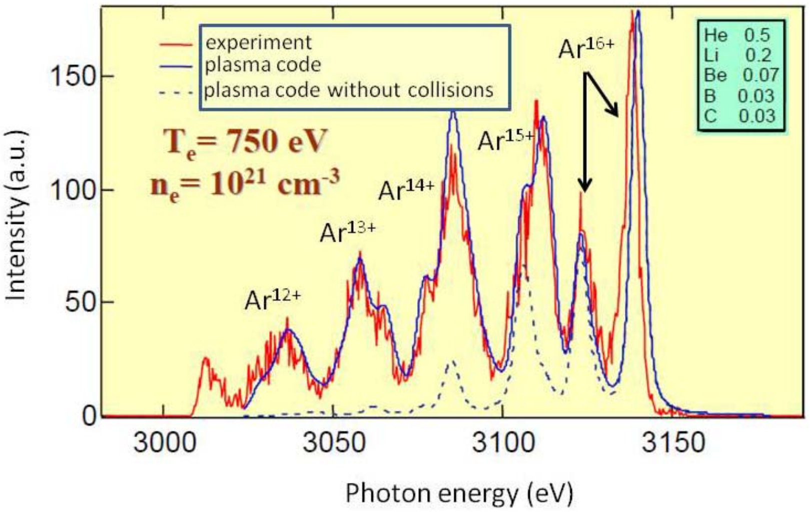

Figure 1.11: High resolution X-ray spectrum (I_{peak}= 5 10^{17} W/cm^2, pulse duration = 80 fs and argon clusters with P_0 = 30 bar) compared to the predictions of the HULLAC code (see text) including or not the collisional excitation processes. The best fit is obtained for an electron temperature of 750 eV, an electronic density of 10^{21} cm^{-3} and the initial charge state fractions (ions with a K-shell vacancy) given in the inset [12].

With high resolution spectra as in Figure 1.11, the use of plasma codes may provide an estimation of the electron temperature and density at the time of the X-ray emission. In the present case, we have used the HULLAC code [51] as a database for a collisional-radiative model solving the time evolution of populations due to competing processes such as collisional excitation and ionization, dielectronic recombination, auto-ionization and radiative processes. A stationary thermal distribution of electrons has been assumed. The predictions of such a simulation is also plotted in Figure 1.11 for which the electronic temperature and density as well as the initial relative charge state fractions of ions with a K-shell vacancy are adjusted to get the best fit with the experimental spectrum. With the dashed blue curve, we measure the crucial role of the collisional excitation and ℓ-mixing processes in the interaction. The extracted electronic density indicates that the expansion of the cluster compared to its initial volume is rather limited at the time of the X-ray emission (in the case of Figure 1.11 an increase of the cluster radius of a factor of 5 can be estimated). Consequently, this confirms that the X-ray production dynamics is rather "fast" within at most a few hundred femtoseconds. Only one measurement of X-ray emission duration has been performed: it gives a duration lower than 700 fs [52]. However, no information on the dynamics of creation of inner shell vacancies is given (by definition) with this plasma code.

Many studies have been limited to spectroscopic analysis of the X-ray emission. However, a precise measurement of **X-ray yields** is essential to reach a complete understanding of the interaction from a fundamental point of view but also for applications (conversion efficiencies and a precise knowledge of the sensitivity of the different parameters governing the interaction allow an optimization of the X-ray photon yields).

1.2.2 ABSOLUTE X-RAY YIELDS

The first quantitative measurements of the X-ray emission ([11], [12] and in Dobosz's PhD thesis [49]) have been obtained with high laser intensities typically from several 10^{16} W/cm^2 up to 10^{18}W/cm^2 irradiating rare gas clusters. A typical evolution of the number of keV photons as a function of the laser peak intensity, I_{peak}, is presented in Figure 1.12 a) for argon clusters. It shows that the experimental result is well fitted by the following power law

Eq. 2

$$N_X \propto I_{peak}^{3/2}$$

Such a behavior, already observed in experiments dedicated to Optical field Ionization (OFI) of rare-gas atoms [53], is associated to a saturation regime: the physical signal grows simply with the number of partners contained in a volume, called the effective focal volume ($V_{eff.foc.}$), where a given intensity threshold (I_{th}) is reached. This saturation regime is also illustrated by the fact that the mean ion charge state is found to be constant (Figure 1.12 b). $V_{eff.foc.}$ is a "physical" volume contrary to the geometrical volume, V_{nom} (also named the nominal focal volume), that depends on the beam waist and the laser wavelength. The physical parameter involved in the evaluation of $V_{eff.foc}$ is the laser intensity threshold, I_{th}, needed to generate a X-ray emission (i.e. an inner shell vacancy) during the laser-cluster interaction. The analytical formula [54] for this volume is given by:

Eq. 3

$$V_{eff.foc} = V_{nom}\left\{\frac{4}{3}\left(\frac{I_{peak}}{I_{th}}-1\right)^{1/2} + \frac{2}{9}\left(\frac{I_{peak}}{I_{th}}-1\right)^{3/2} - \frac{4}{3}\, arctg\left(\frac{I_{peak}}{I_{th}}-1\right)^{3/2}\right\}$$

When $I_{peak} \gg I_{th}$, we find:

Eq. 4

$$V_{eff.foc} \propto I_{peak}^{3/2}$$

Hence, Figure 1.12 indicates that the ionization process in the argon K-shell is already saturated at 10^{17}W/cm^2 and that a laser intensity threshold must exist below this value.

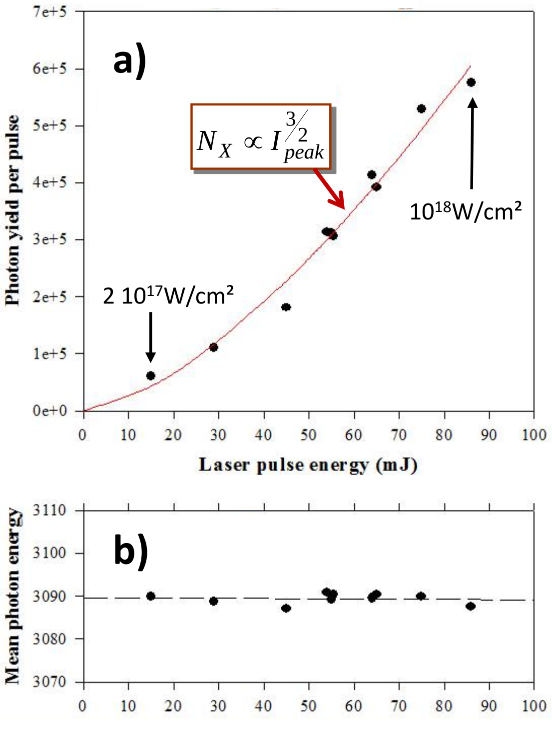

*Figure 1.12: **a)** Evolution of the X-ray yield with the laser pulse energy (proportional to the laser intensity for a given pulse duration; here 70 fs) for argon clusters (P_0 = 25 bar). The experimental results are fitted by a power law $I_{peak}^{3/2}$. **b)** the corresponding mean photon energy emitted by argon ions that reflects the charge state distribution [49].*

This work, however, did not provide us information on the heating mechanisms that remained largely debated in the literature. As a result, we have performed a series of experimental campaigns in order to get quantitative information on the evolution of absolute photon emission yields and complete charge state distributions with different physical parameters governing the interaction; namely intensity, polarization, pulse duration and wavelength of the laser, size and density of the clusters. Two PhD theses in our group are dedicated to these studies: one of Christophe Prigent [55] and the other of Céline Ramond [56]. Their works have allowed us, among other things, to precisely determine the laser intensity threshold (I_{th}) that is a key parameter in the understanding of the dynamics since its value is strongly linked to the efficiency of the heating mechanisms. From a theoretical point of view, no models had been developed at that time to quantitatively predict X-ray yields (except the work of Rose-Petruck *et al* [57] dedicated to clusters of only a few tens of atoms). Nevertheless, the works of Jungreuthmayer *et al* [58] and Fukuda *et al* [59] (and [60]), based on particle in cell simulations and on a mean field approach respectively, have provided some clues on the particle dynamics discussed in §5.1.2. From there and from our knowledge of collisional processes, we have developed, in collaboration with the group of J. Burgdörfer, a new theoretical method based on a mean-field approach ([61], [62] and PhD thesis of C. Deiss [63]) which includes many-particle effects via Monte Carlo events. This approach is, in fact, a generalization of classical trajectory Monte Carlo simulations used to describe the transport of excited ions through solid.

2. STUDY CONDITIONS

To highlight a particular phenomenon, we have to choose the best study conditions so as to determine the most relevant parameters. This is part of the tricky work of an experimentalist! In the context of the dynamics of either an ion or a laser pulse with matter, I give, in this chapter, the arguments that made us to choose the collision systems discussed in this manuscript: Ar^{18+} (v_p =23 a.u.) and Kr^{35+} (v_p =47 a.u.) on carbon solid foils and 800 nm femtosecond laser pulses on rare gas clusters.

2.1 ION-MATTER INTERACTION AT HIGH VELOCITY

2.1.1 CHOICE OF THE COLLISION SYSTEMS

The choice of the collision system, i.e., the ion projectile, the collision velocity and the nature of the solid target, depends on the goal of the study. Here, I focus on:

i) The evolution of the delayed X-ray intensities sensitive to the nℓ-Rydberg state populations (with n as high as 30)
    a) as a function of the ion time of flight behind the target,
    b) as a function of the target thickness or the ion transit time inside the target, i.e., from single collision condition up to equilibrium.

ii) The evolution of the prompt np Lyman intensities (with n < 5) as a function of the target thickness.

iii) The evolution of the fine structure nℓj population sensitive, in particular, to the wake field as a function of the target thickness.

The choice is guided by various criteria. We want to distinguish unambiguously the primary production process of excited states from the ones occurring during the phase of transport. It is then necessary to produce these states through a well defined collisional process and to fulfill the single collision condition with respect to this process whatever the target thickness. The mean free path of other collisional processes has then to be smaller than the one of the primary process to observe collisional transport effects. The sensitivity of an eventual Stark mixing requires several conditions exposed in the following sub-section. We can already mention that the wake field will be effective only if the ion transit time inside the target is long enough compared to the time needed for the establishment of the wake field. Additionally, the time needed to mix significantly excited states by Stark effect must be smaller than the radiative decay time of excited states under study. On the other hand, the delayed X-ray emission will be observable experimentally with a good time resolution only if the de-excitation of the projectile excited states is not too fast. Hence, the choice of an ion not too heavy is preferable since the lifetime of excited states are proportional to Z_p^{-4}. The study of projectile ions with only one electron is much simpler and allows quantitative comparisons with models describing the ion-solid interaction. Finally, it turns out that the criteria mentioned here are most likely reachable in the perturbative regime. Table 2-1 gives the collision systems mainly discussed in this manuscript for which the target is carbon, although other targets have been used, as copper or aluminum (see [29] and [31]).

Collision system	Primary process well identified	Studies performed
Ar^{18+} at 23 a.u. on carbon foils and gaseous (CH_4 and N_2) targets.	Study of the de-excitation of Ar^{17+} initially populated by **single capture.**	• Production and transport of highly excited Rydberg states. • Evolution of np (n < 5) and 2ℓj populations from single collision to equilibrium.
Kr^{35+} (1s) at 47 a.u. on carbon foils.	Study of the de-excitation of Kr^{35+} initially populated by **single excitation**.	• Evolution of np (n < 5) populations and 3ℓj → 2ℓj intensities from single collision to equilibrium.

Table 2-1: Collision systems studied in this manuscript to investigate the ion-solid interaction.

We may check that the criteria K << 1 (Eq. 1) is more or less satisfied for both collision systems (K ~ 0.02 for krypton and 0.08 for argon). In the following sub-sections, I detail the single collision condition and present the characteristic times of all the processes occurring in the ion-solid interaction.

2.1.2 *SINGLE COLLISION CONDITION*

This condition ensures that only one collision occurs during the interaction between projectile ions and a target which is either a solid or a gas for the primary process. The interaction probability of a given process is linked to its cross section σ by:

Eq. 5
$$dP = n_{at}\, \sigma\, dz$$

where n_{at} stands for the target atomic density and dz for the target thickness. Eq. 5 becomes for a target of a thickness d, i.e., for an ion transit time T_{tr}:

Eq. 6
$$P = 1 - e^{-n_{at}\,\sigma\, d} = 1 - e^{-d/\lambda} = 1 - e^{-T_{tr}/t_c}\,,$$

λ being the mean free path ($t_C = \lambda/v_p$). When the single collision condition is satisfied ($P \ll 1$), the probability of double event, which is P^2, is negligible. We have then:

Eq. 7
$$P \approx n_{at}\, \sigma\, d \ll 1$$

For all the range of thicknesses (from ~ 2 to ~ 200 µg/cm^2 of carbon), the single collision condition with respect to the primary process populating the projectile excited states prior to any transport in the solid – single excitation for Kr^{35+} at 47 a.u. and capture for Ar^{18+} at 23 a.u. – is satisfied. Indeed, for the thickest targets, we have:

$P_{excitation} \approx 0.03$ for krypton (see Table 2-4 for the values of t_c and T_{tr})
$P_{capture} \approx 0.09$ for argon (see Table 2-5 for the values of t_c and T_{tr})

In the case of a gaseous target, we must optimize the quantity ($n_{at} \times d$) so as to maximize the physical signal to be recorded while satisfying Eq. 7. In §3.2.1, we will see that the best solution is a high density open gas cell.

2.1.3 *CHARACTERISTIC TIMES: SOME EVOLUTIONS AND SCALING LAWS*

The dynamics of the ion-solid interaction is quite complex. After the primary process (electron excitation or electron capture) takes place, the ion undergoes a sequence of multiple collisions, radiative decay and shell mixing due to the wake field induced by the moving ion. This complexity is then associated with the presence of different time scales. We define below the characteristic times of the various processes involved:

- τ_{AC}, the binary atomic collision time, $\leq 10^{-18}$ s for moderately relativistic ion speeds.
- $\tau_w = {}^{2\pi}/_{\omega_p}$, the characteristic time for the establishment of the wake field, i.e., the wake period related to the plasma frequency $\omega_p = \sqrt{4\pi\, n_e}$ (n_e being the electron density). In the perturbative regime, approximate values for the wake field F_0 at the projectile nucleus and the corresponding plasma frequency can be deduced from measured or tabulated ion stopping power (dE/dx) [6]:

Eq. 8
$$-\frac{dE}{dx} = \bar{Q}\, F_0 \quad with \quad F_0 \approx Z_p \frac{\omega_p}{v_p^2}\, ln\left(\frac{2\, v_p^2}{\omega_p}\right)$$

where $\bar{Q}$ denotes the mean charge state of the projectile at equilibrium. It comes $F_0 \sim 0.133$ a.u. for Kr^{35+} at $v_p = 47$ a.u., $F_0 \sim 0.207$ a.u. for Ar^{17+} at 23 a.u. and $\omega_p \sim 0.97$ a.u. in a carbon foil leading to $\tau_w < 0.16$ fs.

- $\tau_s = {}^{2\pi}/_{|2\,\omega_s|}$, the Stark mixing time where ω_s stands for the dynamical coupling element of the induced wake potential Φ_{ind}:

Eq. 9 $$\omega_s = \left\langle \phi_{n,\ell,m} \middle| -\Phi_{ind} \middle| \phi_{n,\ell'=\ell\pm1,m} \right\rangle \propto \frac{F}{Z_p}$$

A good order of magnitude of ω_s can be found in [64]: $\omega_s \approx \frac{3\,F\,\mathrm{n(n-1)}}{2\,Z_p}$ where n is the principal quantum number.

However, the induced electric field is not uniform at the orbital-size scale [7]. In order to take into account this non-uniformity while keeping a linear approximation of the Stark effect, an effective n-dependent static field is introduced [30] for the calculations of the coupling element with n' = n, $\ell' = \ell \pm 1$ and *m = m'*:

Eq. 10 $$F_{n\ell_{>}m} = F_0\, exp\left(-\alpha_{\ell_{>}|m|}\, n \sqrt{\frac{\omega_p^{1/3}}{Z_p}} \right) \quad with \quad \ell_{>} = max\,(\,\ell, \ell')$$

where $\alpha_{10} = 0.73$, $\alpha_{20} = 0.58$ and $\alpha_{21} = 0.98$. This effective electric field can give rise to a substantial mixing between two states (*a* and *b*) only if

Eq. 11 $$\omega_s \geq |\omega_{ab}/2| \; and \; \omega_s \geq |\Delta\Gamma/4|$$

where ω_{ab} is their energy splitting and $\Delta\Gamma$ the difference between their radiative widths. The Lamb shift and fine-structure splitting are indicated in Figure 2.1 for the Kr^{35+} and Ar^{17+} hydrogen-like ions. Finally, it turns out that τ_s remains smaller than 9 fs for krypton and smaller than 3 fs for argon.

- τ_r, the radiative lifetime of excited states populated during the interaction are given in Table 2-2 and Table 2-3 and also noted in Figure 2.1. We may underline immediately that the radiative decay inside the solid target will play a much more important role for krypton than for argon. We have the following scaling law for an hydrogen-like ion:

Eq. 12 $$\tau_r \propto \frac{n^3 \ell^2}{Z_p^4}$$

- $T_{tr} = d/v_p$, the ion transit time that depends on the foil thickness d. For instance, for Ar^{18+} at 23 a.u. and carbon foils of 2 to 200 μg/cm^2, we have 0.2 fs $\leq T_{tr} \leq$ 20 fs.

Table 2-2 and Table 2-3 give estimated values in atomic unit of the wake field period and the Stark mixing time for the collision systems under study. The experimental observation of a significant Stark mixing is possible only if:

Eq. 13 $$\tau_w \ll \tau_s, T_{tr}, \tau_r \qquad T_{tr}^{min} < \tau_s < T_{tr}^{max} \qquad \tau_s \leq \tau_r$$

The conditions (Eq. 11 and Eq. 13) are roughly satisfied except in the case of krypton for n = 2 for which no Stark mixing will be induced. For argon, since the wake field Stark coupling is larger than the Lamb shift but smaller than the fine structure splitting, the $2p_{3/2}$ state becomes partially "decoupled" from the $2p_{1/2}$ and $2s_{1/2}$ states which, in turn, are strongly mixed. The same conclusions occur for the n = 3 manifold for krypton. Finally, it turns out that the induced potential will only mix fine structure orbitals with the same value of total angular momentum j up to n < 6 in the case of krypton and n < 3 for argon. For this latter case, from n = 3 the induced potential is strong enough to mix different j values. In Figure 2.1 are indicated by red arrows the possible Stark mixing. It comes out that the experimental evolution of the fine structure components of inner shells (n = 2 for Ar and n = 3 for Kr) inside a solid is a good candidate to investigate the role of the wake field.

I remind that 1 atomic unit of time is equal to 0.024 fs.

Kr^{35+} @ 47 a.u. on C foils	wake period τ_w	Stark mixing time τ_s	radiative lifetime τ_r	ion transit time T_{tr}
n		ns_0-np_0	np	$6.4 \leq T_{tr} \leq 403$
2	6.5	370	39	
3		171	132	
4		105	305	

Table 2-2: Characteristic times of the wake field period and of the Stark mixing for Kr^{35+} at 47 a.u. on carbon foils. Radiative decay times as well as the range of the ion transit times are also given. All the characteristic times are given in atomic unit.

Ar^{18+} @ 23 a.u. on C foils	wake period τ_w	Stark mixing time τ_s	radiative lifetime τ_r	ion transit time T_{tr}
n		ns_0-np_0	np	$8.5 \leq T_{tr} \leq 815$
2	6.5	116	628	
3		54	2100	
4		33	5000	

Table 2-3: Same as Table 2-2 for Ar^{18+} at 23 a.u. on carbon foils.

- Additionally to the Stark effects mentioned above, the collisional processes occur as well during the ion transport and may blur the coherent mixing due to the wake field. One defines a mean spacing in time between subsequent collisions, $t_c = \lambda/v_p$, directly linked to the mean free path λ for a given atomic collision process. These mean free times are given in Table 2-4 and Table 2-5. We note that, for the two collision systems discussed here, the collisional effects will be induced through ionization, inter and intra-shell excitation processes, the t_c values for capture being very large compare to the ion transit times in the solid.

Kr^{35+} @ 47 a.u. on C	**single excitation**	ionization	intra-shell excitation		inter-shell excitation	capture	ion transit time T_{tr}
n	1s→np	np	np→nΣℓ' ℓ'≠1	ns→np	np→n'Σℓ' n'=n+1	np	$6.4 \leq T_{tr} \leq 403$
2	$1.2\ 10^4$	1200	926	308	686	$36\ 10^4$	
3	$6.6\ 10^4$	495	123	99	282	$78\ 10^4$	
4	$18.5\ 10^4$	288	58	58	167	$158\ 10^4$	

Table 2-4: Mean free times (tc) of collisional electronic processes in the case of Kr^{35+} at 47 a.u. on carbon. The first column corresponds to the primary process for populating the hydrogenic excited states prior to any transport. The ion transit times in the solid are given in the last column for comparison. Excitation and ionization cross sections calculated from PWBA (with screening and anti-screening effects) and capture with CDW (see §1.1.3). All the characteristic times are given in atomic unit.

Ar^{18+} @ 23 a.u. on C	**single capture**	ionization	intra-shell excitation		inter-shell excitation	ion transit time T_{tr}
n	np	np	np→nΣℓ' ℓ'≠1	ns→np	np→n'Σℓ' n'=n+1	$8.5 \leq T_{tr} \leq 815$
2	8600	167	224	75	132	
3	$2\ 10^4$	77	37	30	67	
4	$4\ 10^4$	48	20	22	46	

Table 2-5: Same as Table 2-4 for Ar^{18+} at 23 a.u. on carbon.

We may give at this point additional remarks. The observation of transport effects on a given ion state will be significant only if its lifetime is long enough so that transport effects take place. For the krypton 2p state, its lifetime (Table 2-2) is shorter than the values of t_c in Table 2-4: no transport effects due to the collisions will occur. Consequently, since no Stark mixing in the n = 2 manifold is possible, no transport effect is expected for this state. However, transport effects should be visible on the 3p and 4p states. For argon, the np state lifetimes (Table 2-3) are much longer. As a result, transport effects will be larger and should be noticeable from n = 2. Additionally, we note that t_c decreases faster than the Stark mixing time τ_S with the principal quantum number n. This implies that the collisional processes will have a dominant role in the study of the production and transport of Rydberg states.

Finally, the branching ratios indicated in Figure 2.1 allow us to take into account the cascade effects on a given level populated by the de-excitation from upper excited levels.

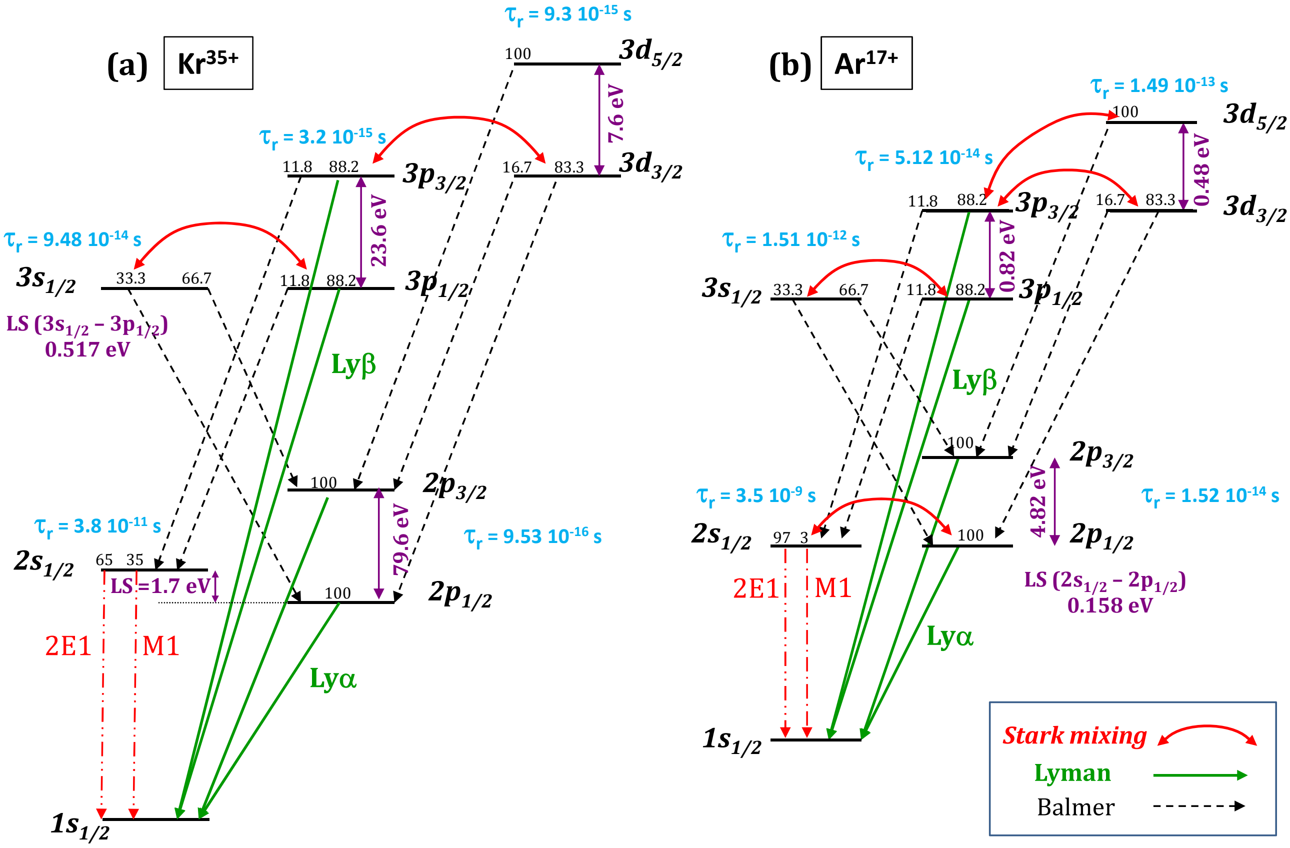

*Figure 2.1: Decay diagrams (n = 2 and 3) of the hydrogen-like Kr^{35+} **(a)** and Ar^{17+} **(b)**. The non relativistic branching ratios (in %) [64] and the lifetimes are indicated above the different $n\ell j$ levels. The Lamb shift (LS) and fine structure splitting values are specified (in purple). The Lyman and Balmer transitions together with the two decay modes of the $2s_{1/2}$ are shown.*

2.2 CLUSTERS UNDER INTENSE LASER PULSES

2.2.1 *WHY NANOMETER SIZED CLUSTER?*

The versatility of atomic clusters in terms of density, size and accessibility to a wide range of species makes them unique physical objects for studying nonlinear response of finite systems. I present mainly results obtained with argon clusters $(Ar)_n$: they are experimentally "easy" to produce and their structure is well-known; they theoretically form a "test system".

Free clusters in a supersonic jet (§3.2.2) combine advantages of both gaseous and solid targets. On the one hand, the low mean atomic density leads to well separated clusters avoiding problem of laser propagation and absorption of the emitted X-rays by the surrounding environment. On the other hand, the local density (density of each cluster) is close to a solid one, the absorption of the laser energy is then locally as strong as in laser-solid interaction.

The laser absorption condition depends on the electronic plasma frequency (ν_{pe}) compared to the laser frequency (λ = 800 nm leads to ν_{laser} = 3.75 10^{14} Hz). For a spherical object, ν_{pe} is estimated to be:

Eq. 14
$$\nu_{pe}(Hz) \sim 9\ 10^3\ \sqrt{n_e\ (cm^{-3})}$$

From there, it is useful to define the critical density obtained when $\nu_{pe} = \nu_{laser}$. This leads to $n_c \sim 1.7\ 10^{21} cm^{-3}$. If $n_e > n_c$, the laser wave is reflected (opacity of the nanoplasma). In our conditions, the time dependant electronic density n_e is at least of the order of $10^{22} cm^{-3}$ (at the beginning of the interaction). As a result, the laser wave will penetrate in the cluster only over a distance called the skin depth. We then choose cluster radii not larger than this skin depth and as this dimension (typically ~ 10 nm) is much smaller than the laser wavelength, the laser field can be described as a uniform time-dependent electric field over the entire cluster.

2.2.2 IONIZATION PROCESSES

As seen in §1.2.1 for argon clusters, highly charged ions with a K-shell vacancy are produced during the laser-cluster interaction. In the following, I examine the different processes of ionization.

- Optical field ionization

The first step in the laser-cluster interaction is the optical field ionization of the atoms inside the cluster. With the laser wavelength (λ = 800 nm) and the intensity range we have used (a few 10^{14} to 10^{17} W/cm^2), the Coulomb potential barrier is lowered by the laser electric field (Figure 2.2) allowing the Tunnel Ionization (TI; the crossing time of the barrier is shorter than the optical cycle time of 2.7 fs and, consequently, the electric field is considered as quasi-stationary) and, for higher intensities, the Barrier Suppression Ionization (BSI; the potential barrier is fully suppressed in this case). The TI probability can be evaluated from the ADK rates [65] while, for BSI, one can simply evaluate the laser intensity needed to ionize an electron with a binding energy E_i of a given ion with a charge q [66] by:

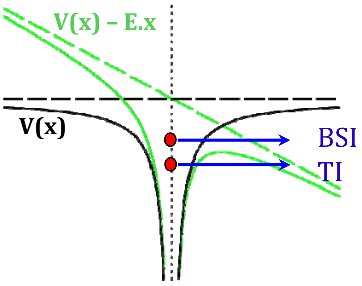

Figure 2.2: Schematic representation of the tunnel (TI) and barrier suppression (BSI) ionization.

Eq. 15
$$I_{BSI}(W/cm^2) = 4\ 10^9\ \frac{E_i^4(eV)}{q^2}$$

In Table 2-6, are reported the values of I_{BSI} for argon ions. What can be underlined is the very high intensity values needed for the ionization of the 2p and 1s electrons in Ar^{9+} and Ar^{16+} respectively. Those values were out of reach in our experiments. This means that we can produce only up to 8 electrons per atom by optical field ionization.

- Electron impact ionization

Electrons produced by optical field ionization have low energy (~ eV). Those electrons may ionize the surrounding ions only if they gain a kinetic energy of the order of the binding energy of the bound electron to be ionized. Driven by the oscillating laser field, one show that the maximum energy an electron can gain due to its oscillatory motion is approximately twice the well-known ponderomotive energy U_p:

Eq. 16 $$T_{max}(eV) \approx 2U_p \approx 1.9\ 10^{-13}\ \lambda^2\ \tilde{I}(W/cm^2)$$

From this formula, we estimate the mean laser intensity (Ĩ) needed for this process of energy gain (see Table 2-6). The extracted intensity values are in the laser intensity range we have used.

Ionization of the nℓ electron in Ar^{q+}	I_{BSI} (W/cm^2)	$\tilde{I}(W/cm^2)$ for $T_{max}(eV) \sim E_i$
Ar^{1+} (3p) (E_i = 16 eV)	2.5 10^{14} W/cm^2	
Ar^{8+} (3s) (E_i = 143 eV)	2.6 10^{16} W/cm^2	1.2 10^{15} W/cm^2
Ar^{9+} (2p) (E_i = 422 eV)	1.6 10^{18} W/cm^2	3.5 10^{15} W/cm^2
Ar^{16+} (1s) (E_i = 4.1 keV)	4.0 10^{21} W/cm^2	3.4 10^{16} W/cm^2

Table 2-6: In the second column are reported the laser intensities for the Barrier Suppression Ionization (Eq. 15) process. In the third column are estimated the laser intensities required to get electrons with kinetic energies close to the binding energy E_i (Eq. 16).

Experimental electron impact ionization cross sections can be found in the literature. In the Prigent's PhD thesis [55] a compilation of data was done for the ionization of argon atoms and ions (Figure 2.3) and the data have been fitted by a revisited Lotz formula [67].

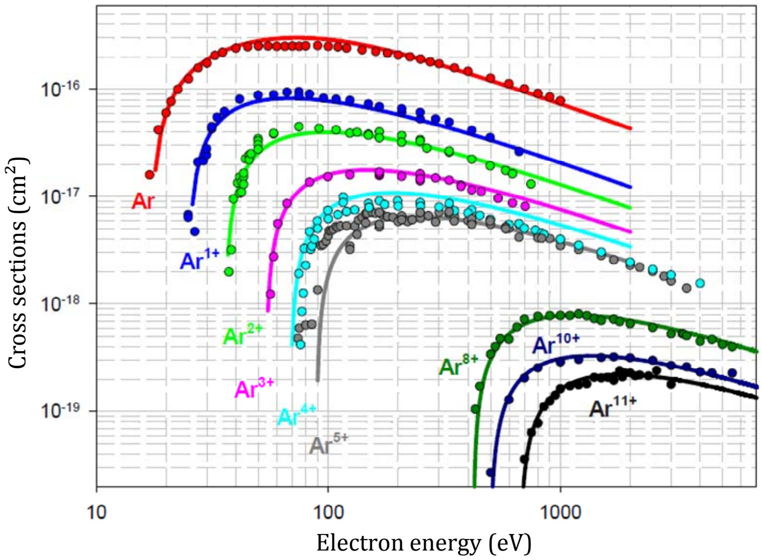

Figure 2.3: Electron impact ionization cross sections as a function of the electron energy. Circles are experimental results and solid lines are the revisited Lotz formula (see [55] for details).

To ionize a K-shell electron in argon ions, the energy of the incident electron must reach an energy between 3.2 and 4 keV (depending on the ionization degree of the ions). In this case, the K-shell ionization cross section has a value of ~ 3 10^{-21} cm^2 [68].

Other ionization processes have to be mentioned as electron impact excitation followed by impact ionization evaluated also from the revisited Lotz formula) and auto-ionization due to Auger decay (all those processes are considered in our theoretical approach (see §5.1.2)).

3. EXPERIMENTAL ENVIRONMENT

In this chapter, I rapidly describe firstly the large scale facilities that provide us the "projectile" (the high velocity ion beams and the intense short laser pulses) and secondly the production systems of "targets" (atoms, clusters and solid foils). After a short description of our X-ray spectrometers, experimental set-ups are displayed and commented.

3.1 LARGE SCALE FACILITIES USED

3.1.1 GANIL FOR THE PRODUCTION OF HIGH VELOCITY ION BEAMS

The French national heavy ion accelerator at Caen GANIL[1] (Figure 3.1) is a large installation dedicated to research in nuclear physics, atomic physics and condensed matter under irradiation. Ions extracted from an ion source are first post accelerated by a small cyclotron (C01 or C02) coupled to two large cyclotrons (CSS1 and CSS2) so as to reach energies up to ~ 8 MeV/u for uranium ions and ~ 95 MeV/u for argon ions. The ion beams are then directed towards experimental rooms. SME (Sortie Moyenne Energie – for interdisciplinary researches with medium energy stable ion beams) and LISE (Ligne d'Ions Super Epluchés – for the selection of highly stripped ions and radioactive nuclei) are the two experimental rooms used for the study of ion-matter interaction in the high velocity regime.

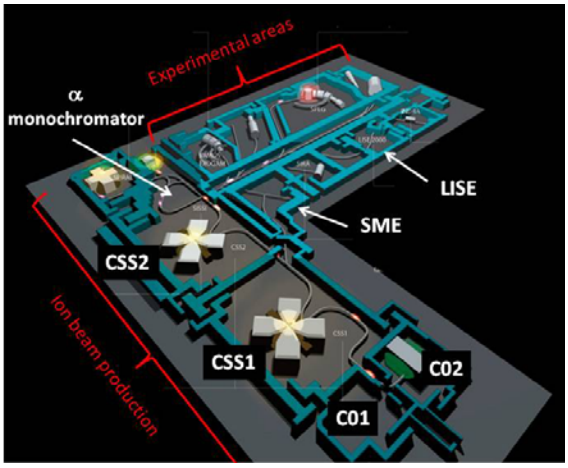

Figure 3.1: GANIL (Grand Accélérateur National d'Ions Lourds - CEA/IN2P3/CNRS) at Caen.

For the ion beams with a usual profile as a circular spot of a few mm, the SME room is well adapted in terms of optic elements. After CSS1, Ar^{10+} ions at 13.6 MeV/u are easy to produce. Strippers (solid foils) placed at the exit of CSS1 or at the entrance of the SME room ensure the production of the desired ion charge state. The experiment dedicated to the study of *the production and transport of long-lifetime excited states of the* Ar^{17+} has been performed in SME with the collision system: Ar^{18+} at 23 a.u. (13.6 MeV/u) on solid C targets.

For the experiments very demanding in terms of counting rate and resolution for our X-ray spectrometers, we have used the LISE line that combines the advantages of high beam intensity, low background, very good optics together with a small energy divergence. To perform measurements with a gas (low density target) under the same experimental conditions as for solid targets, high ion beam intensities (up to 1 eμA on the target) are required. Then to reach a resolution of a few eV (at a few keV) with our X-ray spectrometers, a specific ion beam profile is needed: a very well focused beam in the vertical direction and almost parallel in the other direction. The use of CSS1 "Solo" (for the argon beam) or CSS1+CSS2 (for the krypton beam) combined together with the alpha spectrometer allows, thanks also to the beam optics elements of the LISE beam line, to get high current intensities within a beam spot less than 1 mm of height and an almost horizontal parallel beam of a width around 6 mm. On the LISE beam line, two different ion beams have been used: Ar^{18+} at 23 a.u. (13.6 MeV/u) and Kr^{35+} at 47 a.u. (60 MeV/u). To get the desired charge state, strippers have been placed, in both cases, at the entrance of the α spectrometer. Two experiments dedicated to *the evolution of the excited inner-shell populations with the target thickness* (from "0" obtained with the gaseous target to ~ 200 μg/cm^2) have been performed using the LISE beam line.

---

[1] GANIL : Grand Accélérateur National d'Ions Lourds http://www.ganil-spiral2.eu/leganil/

It is worthwhile to mention that the ETACHA code [24], developed in the group, is well adapted to the GANIL ion energies to predict the stripper thickness necessary for an optimization of the desired charge state.

3.1.2 LUCA FOR INTENSE LASER PULSE PRODUCTION

SLIC[2] (Saclay Laser matter Interaction Center) is a research infrastructure at Saclay including three main facilities among which LUCA[3] (Figure 3.2). The LUCA server, based on Chirp Pulse Amplification technique, provides infrared (800 nm) laser pulses of energy up to 100 mJ, of duration down to 50 fs at full width at half maximum (FWHM) with a repetition rate of 20 Hz. Following the LUCA line, a compressor and an attenuator are installed to vary the pulse duration and the laser energy, respectively. The pulse duration can be varied up to a few ps. The linearly polarized laser beam with a diameter around 50 mm is then focused by a simple focal lens down to a diameter of ~ 20 µm.

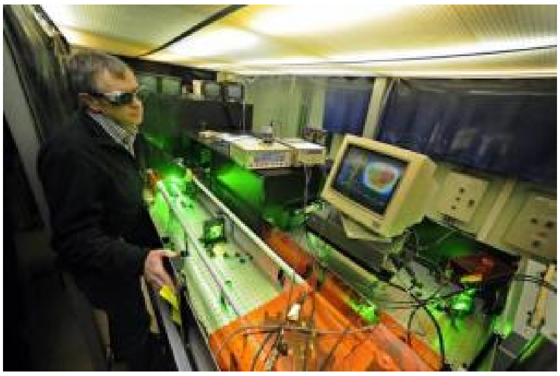

Figure 3.2: LUCA (CEA, Saclay), part of SLIC, is a versatile laser facility with peak power up to 1TW and 50fs pulse duration.

The precise imaging of this focal spot enables us to evaluate the laser peak intensity. We use laser pulses with intensities in the 10^{14} to 10^{17} W/cm^2 range determined with accuracy better than ± 20% [55]. Finally, the laser pulse temporal contrast measured by a third order auto-correlator is found to be much lower than 10^{-4} of the main pulse over an interval of 4 ps (further, the contrast falls down to 10^{-6}). No pre-pulse is observed avoiding a pre-ionization of clusters and providing experimental conditions as clean as possible.

3.2 THE TARGETS

Three types of target have been used: isolated atoms, rare gas clusters and thin amorphous carbon foils. The geometrical and/or thermodynamic characteristics of the production system must be controlled to obtain the desired target system. In the present work, atoms and solid foils have been irradiated by ion beams while clusters have been submitted to strong optical fields.

3.2.1 ATOMIC TARGETS

I remind that the single collision condition is satisfied if $P \approx n_{at}\, \sigma\, d \ll 1$ (Eq. 7 §2.1.2). Two types of gaseous targets may be used in the experiments dedicated to the study of the ion-matter interaction, either a gaseous effusive jet or a gas cell.

In the low velocity regime, the capture cross section is so high ($\sigma \sim 10^{-15}$ cm^2 see §1.1) that we need to have $n_{at} \times d << 10^{15}$ cm^{-2} to fulfill the single collision condition. The use of an effusive jet is then well adapted. An example is given in reference [18]. In the high velocity regime, the cross sections are much smaller ($\sigma \sim 10^{-18}$-10^{-20} cm^2 depending on the process in the case of argon on carbon, see §1.1.3) and in order to maximize the physical signal, a gas cell that ensures a much larger quantity $n_{at} \times d$ is used.

In practice, the gaseous targets (CH_4 or N_2) are in an open cell (diameter of 90 mm) whose input and output are compatible with the ion beam size (Figure 3.3).

---

[2] SLIC is part of the LASERNET network and of the LASERLAB cluster of large scale Laser installations : http://iramis.cea.fr/slic/index.php

[3] LUCA: Laser Ultra Court Accordable

Hence, the ion beam is not modified in terms of charge state, energy and angular dispersion, contrary to what happens with a close cell. The gas inlet is connected to a gas handling system while a pressure sensor measures continuously the cell pressure. The other flanges of the cell for the spectrometers are sealed by 25 µm Mylar foils that allow recording X-ray emission without efficiency loss. The open cell is placed in the collision chamber in which the residual vacuum has to be maintained as low as possible. In that respect, collimators at the input and output of the ion beam improve the residual vacuum by reducing the conductance.

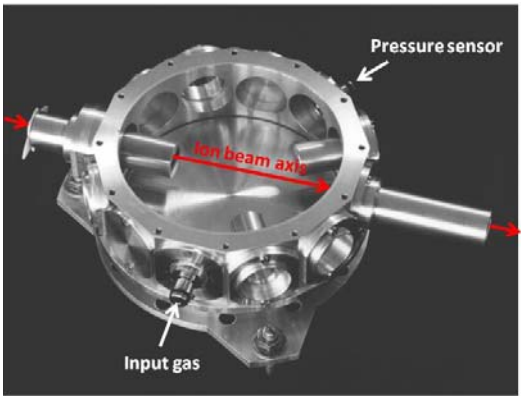

Figure 3.3: Photo of the open gaseous cell cover removed.

With pressures in the cell of a few 10^{-2} to 10^{-1} mbar, we are then able to maintain a residual pressure that does not exceed a few 10^{-4} mbar in the main chamber itself, and less than 10^{-5} in beam lines. Finally, atomic densities of around a few 10^{15} at/cm^3 in the cell are reachable. A precise study is presented in [69].

3.2.2 CLUSTER PRODUCTION

Clusters are generated within a pulsed adiabatic expansion of a gas flow at high pressure (i.e., a baking pressure P_0 from a few to several tens of bar) through a conical nozzle that opens into an expansion chamber maintained at a pressure $P_1 << P_0$. The nozzle is mounted on a solenoid pulsed valve operated at a repetition rate in the 1 - 20 Hz range (Figure 3.4). A minimal opening duration of a few 100 µs insures to reach a stationary regime for the cluster formation. The clusters formed have local density close to the solid one (~ 10^{22} at/cm^3). The mean atomic density of the cluster jet (n_{at}) and the cluster size (the mean number of atoms per cluster $\bar{N}_{at/cl}$) can be estimated by scaling laws. They both depend on the nature of the gas (rare gas are used), on the geometry of the conical nozzle (Figure 3.5), i.e., the diameter d of the hole, the open angle α and on the thermodynamic parameters P_0, T_0.

- $n_{at} \propto \frac{P_0}{T_0} \times \left(\frac{\mathrm{d}}{z \times tan\alpha}\right)^2$ where z is the distance from the hole. For d = 300 µm, α = 7.5° and with P_0 from 1 to 50 bar (at room temperature), typical values of 10^{13} to 10^{15} at/cm^3 are obtained at z = 500 mm, and reach 10^{15} to 10^{18} at/cm^3 at z = 35 mm (close to the exit of the conical nozzle).
- $\bar{N}_{at/cl} \propto P_0^b$ for fixed parameters d and α. In the literature b may vary from 1.6 to 2.3. Rare gas clusters with variable sizes from 10^2 to 10^6 atoms/cluster are generated (i.e. cluster diameter from 1 to 40 nm).

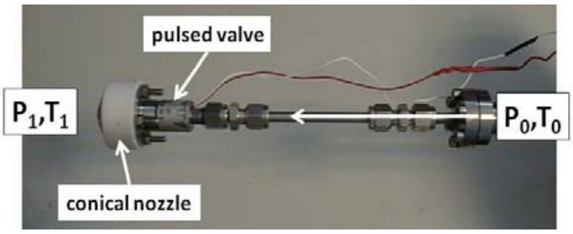

Figure 3.4: Production system of clusters: photo of the pulsed valve and conical nozzle.

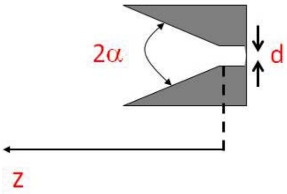

Figure 3.5: Geometrical parameters of the conical nozzle.

A skimmer is also used for large values of z to select the coldest part of the cluster jet. From the mean atomic density and the cluster size, one can estimate the distance between clusters. Typically, for argon with P_0 = 40 bar, the distance varies from ~ 1 µm (at z = 35 mm) up to 10 µm (at z = 500 mm). As a result, the clusters are well separated from each other.

I must add that to go beyond the commonly used scaling laws, as presented in Ramond's PhD thesis [56], a specific experimental work has been performed to determine in absolute the mean atomic density, clustering fraction and time structure profile of the cluster bunches.

3.2.3 THIN SOLID FOILS

Thin solid foils of carbon are relatively easy to manufacture and handle (depending nevertheless upon their thickness). Those solid targets are of amorphous type and are made using a technique of evaporation on glass slides coated with a wetting (typically NaCl). The carbon film is separated from the glass and collected on an aluminum support drilled with a hole of a large size with respect to the ion beam size. As the cross sections of the atomic processes strongly depend on the atomic target number (the capture process roughly varies as Z_t^4 while the ionization/excitation process as Z_t^2 in the high velocity regime), the purity of the foils has to be carefully checked. In consequence, the thickness and the impurity content are measured by means of Rutherford-backscattering analysis with ~ 1 MeV α particles produced by the INSP Van de Graaff accelerator. The most frequent impurity is oxygen, with a relative content varying between 0.3% and 5%. We select targets where impurities contribute less than a few % to the total signal. Self-supported carbon foils of thickness ranging from 2 (±30%) to 210 (±5%) μg/cm^2 have been used (i.e., from 100 Å to 1 μm).

3.3 X-RAY SPECTROMETERS

We employ routinely two types of spectrometers: solid-state detectors and Bragg-crystal spectrometers for which high transmission can be reached. As a result, both types of detectors are very well adapted for precise measurements of transition intensities. The solid-state detectors are used to record the total X-ray emission from 1 to a few tens of keV while the Bragg spectrometer allow performing an efficient zoom of a given X-ray region over a few 100 eV. In the following, I just give a brief description and discuss the total transmission.

3.3.1 BRIEF DESCRIPTIONS, RESOLUTION AND DETECTION EFFICIENCY

a) Solid-state detectors

The first-generation detectors consist of a rather thick semiconductor crystal (a few mm) so as to detect energetic photon of several tens of keV. A voltage of ~ 1 kV applied across the crystal gives rise to a detection zone and to a thin dead layer. Usually there is also a gold layer acting as the front electrode. The ensemble is connected to a liquid nitrogen cryostat for cooling purpose (Figure 3.6). Typically, a 180 eV FWHM resolution is obtained at 3 keV. The new generation detectors (Figure 3.7) are based on the silicon drift detector (SDD) technique which combines a large sensitive area (the entire wafer is sensitive to radiations, i.e., no dead layer is present) with a small output capacitance due to a sub-millimeter crystal thickness. A Peltier element cools the crystal down to a working temperature of around −10°C. A FWHM resolution of around 130 eV at 3 keV is reachable. These detectors have to run under good vacuum conditions (10^{-7} mbar) and are, consequently, isolated by means of a beryllium window.

Figure 3.6: Picture of one Si(Li) detector connected to its liquid nitrogen cryostat.

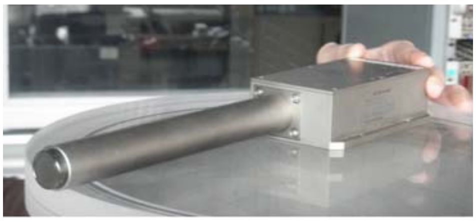

Figure 3.7: Picture of one silicon drift detector with its Peltier unit.

The first-generation detectors have a large energy range from 1.1 to 70 keV while a detection range from 850 eV to 25 keV is obtained with SDD detectors (but they have a better resolution). The detection efficiency of our detectors has been carefully determined [70] and examples are given in Figure 3.8. We may note that at 3-5 keV, the efficiencies exceed 80%. In summary, the solid-state detectors are simple to handle and offer a good compromise between resolution and detection efficiency. In the following, I will name $\boldsymbol{\varepsilon}(\boldsymbol{E})$ the efficiency of a given detector at the photon energy $\boldsymbol{E}$.

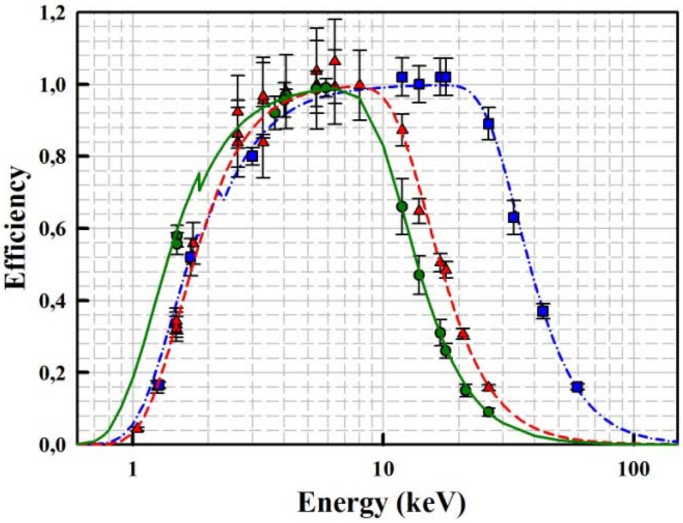

Figure 3.8: Efficiency over the entire energy range of detection for three solid-state detectors: green and red for two SDD detectors and blue for a Si(Li) detector [70].

b) Bragg crystal spectrometers

Our high-resolution high-transmission Bragg-crystal spectrometers (Figure 3.9) are designed to be very flexible so as to be adaptable to the photon energy to be analyzed and to the resolution needed to separate two close photon energies. A detailed description is presented in [69]. High transmission is achieved by combining a mosaic crystal with a large surface localization detector. Highly oriented pyrolytic graphite (HOPG) crystals well adapted for the analysis of 3-5 keV X-rays are used with a mosaic spread (2α) of typically 0.4° - 0.6°. With a mosaic crystal, X-rays of a given energy are reflected (Figure 3.10) within an angular acceptance close to the mosaic spread (much larger than the typical diffraction pattern for perfect crystal).

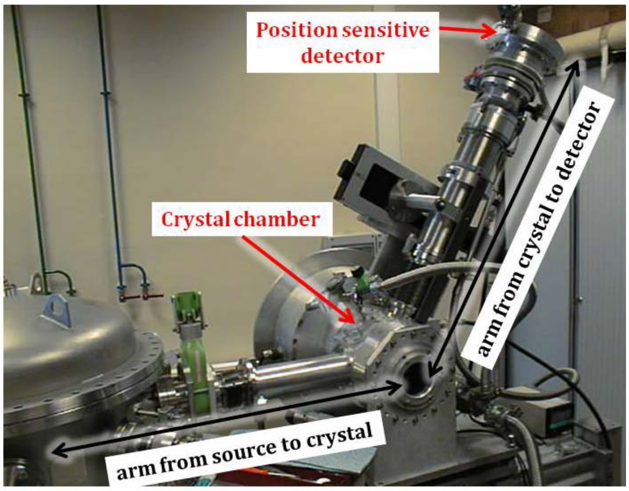

Figure 3.9: Picture of one Bragg-crystal spectrometer.

As a result, the integrated reflectivity (R_θ) of HOPG leads to transmission of almost one order of magnitude greater than the one obtained with a flat Ge(111) crystal, for instance. We have developed a large (60×60 mm^2) home-made multi-wire gas detector. This position sensitive detector, running as a proportional counter, is usually filled with either Ar(CH_4) or Xe(CH_4) at a pressure close to 1 atm and sealed by a thin aluminized Mylar window. An incident X photon generates, by photoelectric effect, an electron further accelerated towards the anode at 1.6-2 kV. It follows an electron avalanche whose opposite induced charge is detected by the cathode. The localization is obtained by charge division and a spatial resolution better than 500 μm can be reached. Characteristic evolutions of the detector efficiency with the photon energy are shown in Figure 3.11. The choice between

$Ar(CH_4)$ and $Xe(CH_4)$ depends on the photon energy to be examined. It is clear that $Ar(CH_4)$, compared to $Xe(CH_4)$, is more suitable to detect the Lyman lines with n > 4 emitted by 13.6 MeV/u argon ions whose energy is around 4.9-5.1 keV. Indeed, in this range, the L-edge absorption coefficient of Xe gives rise to a sudden change in the detection efficiency (see red line in Figure 3.11). On the other side, we use $Xe(CH_4)$ for the detection of the ~ 3.3 keV krypton Balmer α transitions for an optimal efficiency.

The spectrometers are used in a vertical geometry and the detector is tilted to remove, at first order, the line broadening due to Doppler effect. We also choose an appropriate observation angle θ_L in order to be insensitive to the possible polarization of the recorded line intensities (the crystal itself acting as a polarimeter). Moreover, if the two arms of a spectrometer have equal lengths (equal target-to-crystal and crystal-to detector distances), the broadening effects associated with the mosaic spread vanish at first order. Under these conditions, the largest remaining contribution to the resolution comes from the optical quality of the beam. For example, a beam vertically focused down to less than 1 mm and of several mm horizontally leads to a resolution power of about ~ 1500 at 3.8 keV with arms of 1630 mm and a detection performed at θ_L = 30°.

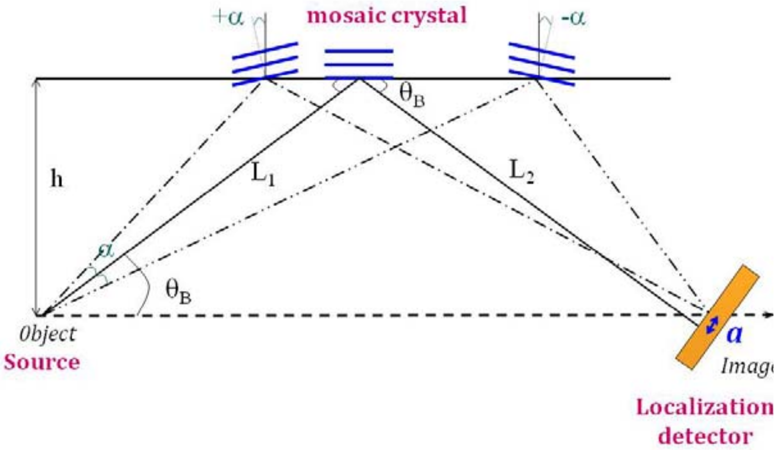

Figure 3.10: Schematic behavior of a mosaic crystal reflecting a given photon energy from a punctual source at a Bragg angle θ_B. Due to the mosaic structure, the image on the localization detector is enlarged by a quantity a. The length L1 and L2 are named arms of the spectrometer.

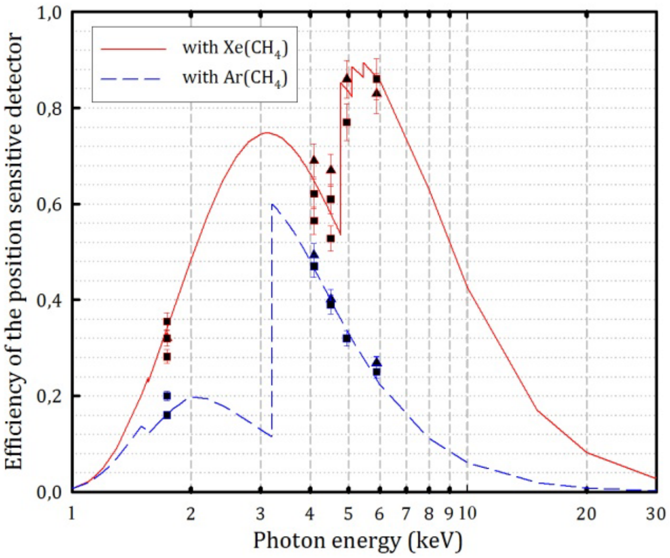

Figure 3.11: Efficiency of our position sensitive detector for two different detection gases with a pressure of 1.15 atm. The detector is sealed with an aluminized Mylar foil (10 µg/cm² of Al and 12 µm of Mylar).

3.3.2 TOTAL TRANSMISSIONS

Control and precise knowledge of the global transmission of the detection system is a key parameter to obtain quantitative measurements. A special care is taken to the absolute calibration in terms of efficiency and solid angle for each detector. Indeed, the global detection transmission $T(E)$ for a given X-ray line is given by the following equation:

Eq. 17
$$T(E) = \varepsilon(E) \times \frac{\Omega_L}{4\pi} \times \frac{d\Omega_p}{d\Omega_L} \times T_{filter} \quad \text{with} \quad \frac{d\Omega_p}{d\Omega_L} = \frac{1-\beta^2}{(1-\beta\, cos\theta_L)^2}$$

where $\varepsilon(E)$ is the detector efficiency given above (Figure 3.8 for the solid-state detectors and Figure 3.11 for the Bragg spectrometers). $\Omega_L/4\pi$ is the relative solid angle in the laboratory frame and $d\Omega_p/d\Omega_L$ corresponds to the relativistic correction of solid angles given by the Lorentz transformations. In the case of the ion-matter interaction, the ion projectile emits X-rays in flight at a velocity of $\beta = v_p/c$ = 0.33 for krypton and 0.17 for argon and the X-rays are detected at the laboratory angle θ_L. Finally, T_{filter} stands for the transmission from an eventual filter placed in front of the detection crystal.

The expression of $\Omega_L/4\pi$ depends on the collimation system used in front of the collision point. In most cases, we use circular diaphragms to collimate the solid-state detectors. The relative solid angle becomes simply:

Eq. 18
$$\frac{\Omega_L}{4\pi} = \frac{S}{4\,\pi D^2}$$

if $S << D^2$ with S the diaphragm surface and D the distance from the diaphragm to the target. For the measurement linked to the de-excitation of the long-lifetime excited states, we have used a slit giving rise to an additional factor explained in §0. For the Bragg spectrometers, the solid angle is proportional to the crystal reflectivity R_θ and the crystal width. Finally, we have:

Eq. 19
$$\frac{\Omega_L}{4\pi} = \frac{h_d}{2\,\pi(L_1+L_2)} R_\theta = \frac{h_d}{2\,\pi(2L)} R_\theta$$

with h_d the detector size (60 mm) and L the arm length. I point out here that additional terms have to be taken into account when dealing with the open cell. All the information is given in [69].

In any case, the transmission is always evaluated experimentally. Indeed, either $\Omega_L/4\pi$ or $\varepsilon(E)$ is determined trough dedicated measurements systematically performed before and after each experiment. Those measurements are usually based on the analysis of the fluorescence yield of solids induced by electron impact. The composition of those solids is well known, as $NaNO_3$, MgF_2, KClAl, Si, CaF_2, Sc, and stainless steel. Typical transmissions of ~10^{-5} - 10^{-6} (with accuracy from a few % to 20%) are attained with photons in the 3-5 keV range.

3.4 EXPERIMENTAL SET-UPS

The aim of our studies is to shed light on phenomena whose cross sections may be rather small. So, high transmission and good resolution for the detectors are necessary. The signal/background ratio must be as high as possible implying a control of all the uncertainty sources and a reduction of the background noise when possible. Therefore, the detectors are electrically isolated from the collision chamber and shielded from external radiation. In this section, I just show some pictures and point out a few specificities for each experiment.

3.4.1 SET-UP AT GANIL

In the case of the ion-matter interaction, details on the set-ups are given in [31] for Kr^{35+} @ 47 a.u. on C and in [27] and [39] for Ar^{18+} @ 23 a.u. on C. Figure 3.12 and Figure 3.13 present pictures of a typical experiment mounted on the LISE facility at GANIL. Five spectrometers were used: (i) two crystal-spectrometers placed at an angle θ_L =30° on each side of the beam axis combined to two solid-state detectors placed at 120° and 150° that record the prompt X-ray emission from excited ions; (ii) one SDD detector regarding the X-ray emission 127 mm behind the target. An electron gun was also mounted so as to check regularly the detection calibration. Control of the ion beam shape at the crossing zone is ensured with profilers placed before and after the collision chamber. Beam intensity in the 10–1000 nAe range on the target is measured by a Faraday cup located after the interaction zone that gives the number of ion projectiles (N_{proj}) with a typical precision better than 1%.

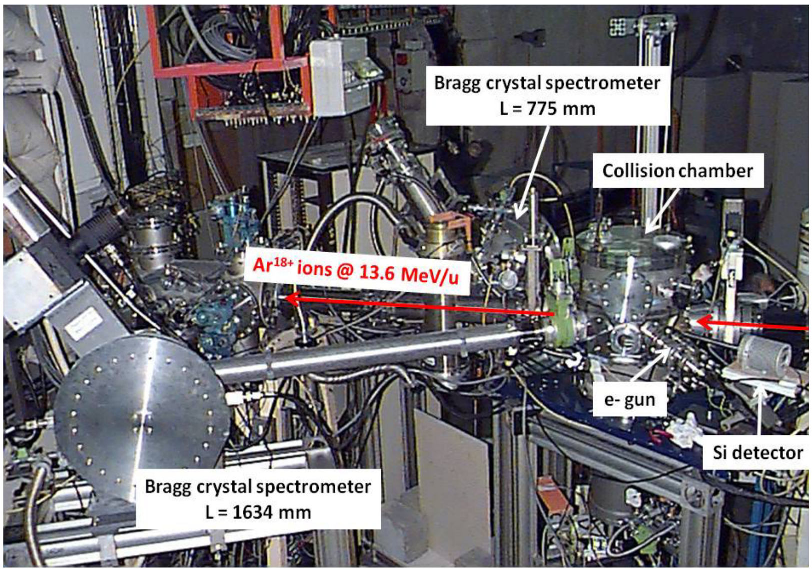

Figure 3.12: Set-up in the LISE room of the experiment dedicated to the study of the interaction of 13.6 MeV/u Ar^{18+} ions with atoms and solids.

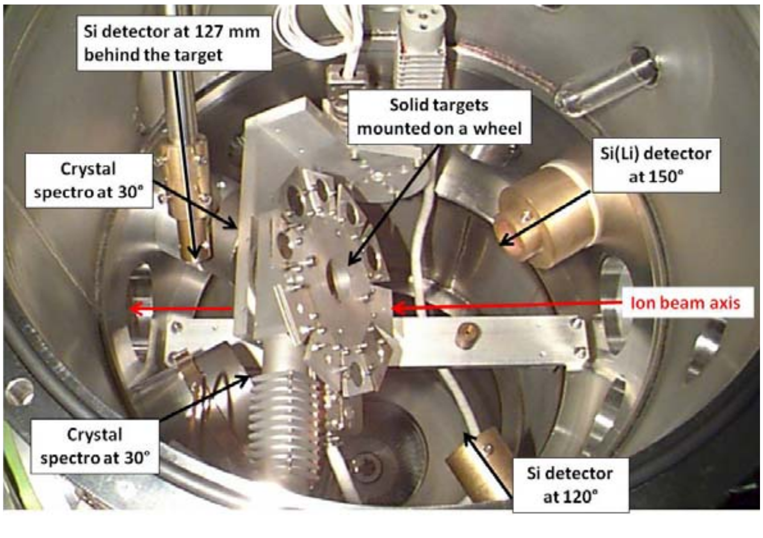

Figure 3.13: Set-up inside the collision chamber (of the experiment in Figure 3.12) with the different solid carbon targets mounted on a rotating wheel.

3.4.2 *SET-UP AT LUCA*

For the laser-cluster interaction, a full description is found in [55]. Figure 3.14 shows pictures of the experimental set-up. Usually, three spectrometers are used: two solid-state detectors to determine the total number of emitted X-rays and one Bragg spectrometer to analyze the charge state distribution of ions responsible for the X-ray emission. As in §3.4.1, an electron gun is positioned for on-line calibration. The linearly polarized laser light with a beam diameter around 50 mm is focused by a 48 cm focal length lens placed in front of the entrance window of our main interaction chamber. The focusing lens and the cluster jet are mounted on translators.

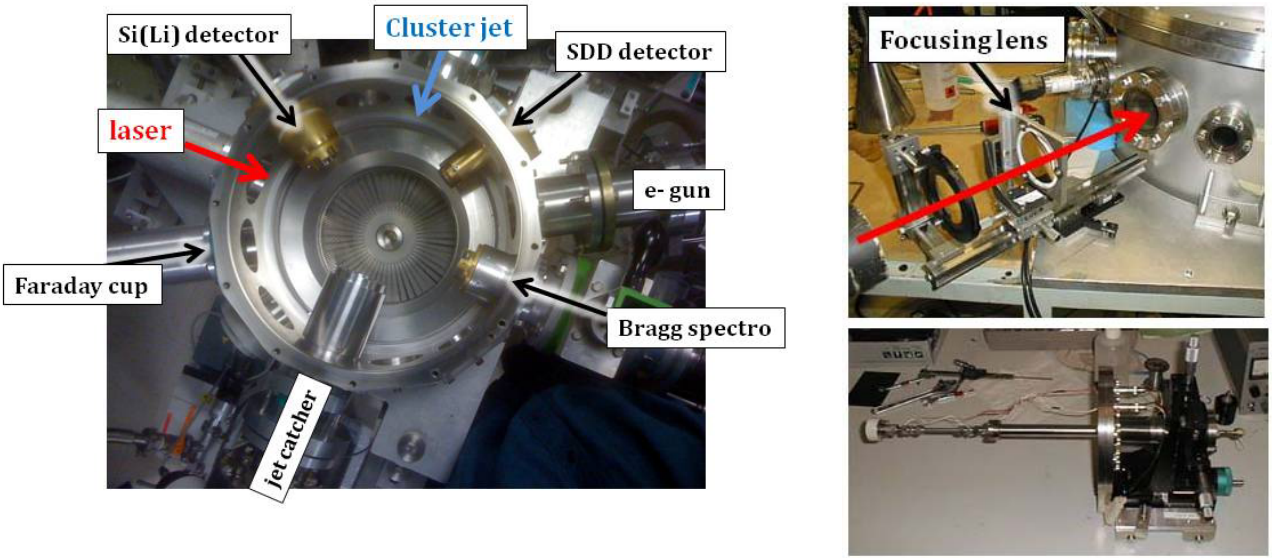

(a) **(b)**

*Figure 3.14: **(a)** Top view of the interaction chamber with the positions of the detectors. **(b)** Focusing lens (top) and cluster jet (bottom) each mounted on a translator.*

Several degrees of freedom in our experimental system allow optimizing the spatial overlap between the laser and the cluster jet (Figure 3.15). The delay (t_{VL}) between the opening of the valve and the incoming laser pulse can be varied so as to scan the cluster jet in the cluster propagation direction (Z). Second, the cluster jet can be translated in the perpendicular direction (XY) to the cluster propagation axis to adjust the position of the incoming clusters with respect to the laser focal spot. Finally, the translation of the focusing lens along the laser propagation axis optimizes the position of the focal spot in the cluster jet. Typical X-ray yield measurements are displayed as well in Figure 3.15 and the optimum is found to be independent on the backing pressure, i.e., the cluster size and the mean atomic density [71]. Indeed, the mean atomic density remains low enough to prevent any problem of laser propagation (the laser focus is not modified) contrary to what may occur when using an ultra dense cluster jet [72]. These adjustments insure reproducible experimental conditions shot by shot (one laser shot impinging on one cluster bunch).

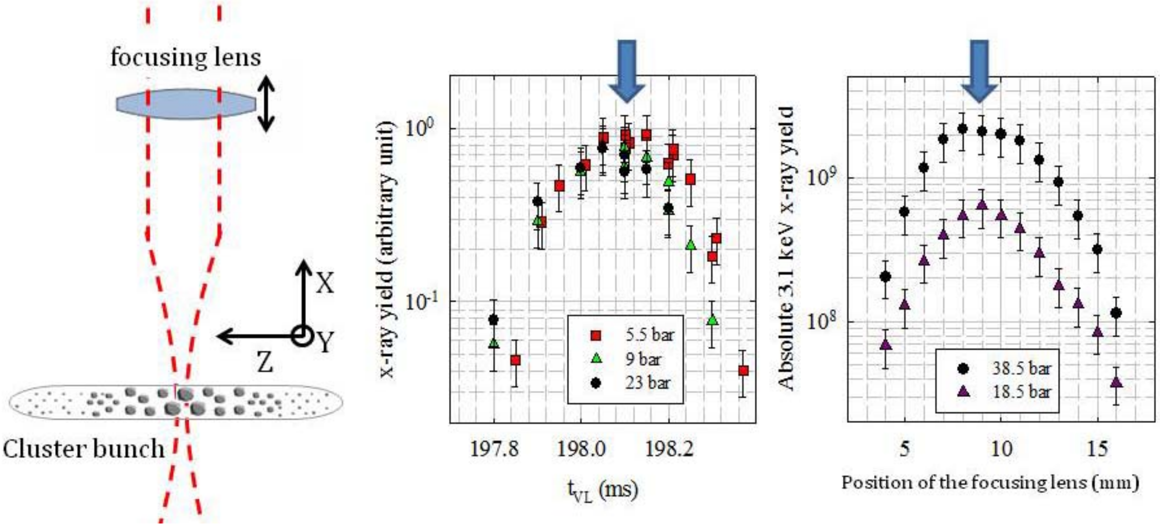

Figure 3.15: Principle for optimizing the X-ray signal in laser-cluster interaction (see text). The large blue arrows indicate the best values of the valve-laser delay time (t_{VL}) and the focusing lens position for this optimization.

4. X-RAY SPECTRA

Additionally to the global transmission, the response function of each detector has been carefully determined and is well understood. This allows us to extract precisely the intensity of each line of a spectrum so as to obtain meaningful absolute values of cross sections. In the following, I present a few X-ray spectra obtained i) when swift bare argon ions collide with either atoms or thin solid foils and ii) when rare gas clusters are submitted to intense infrared laser pulses.

4.1 IN THE CONTEXT OF THE ION-MATTER INTERACTION

The spectra recorded in the case of krypton ions are shown in [29] and [31]: with the solid-state detectors, all the transitions from 1 to a few 10 keV, i.e., the Balmer α and the Lyman series (see Figure 2.1(a) for the decay scheme of the hydrogen-like krypton ion), are recorded, while the high resolution X-ray spectrometers allow performing a zoom of the Balmer α transition. In this sub-section, to illustrate the work performed, I present in more details some X-ray spectra recorded when 13.6 MeV/u Ar^{18+} ions interact with either atoms or solid foils (see Figure 2.1(b) for the decay scheme of the hydrogen-like argon ion).

4.1.1 EMISSION OF PROMPT Ar^{17+} X-RAY TRANSITIONS

Most of the excited states populated during the interaction decay very fast via single photon modes towards the ground state, i.e., inside the solid and immediately after leaving the solid, within a few 10^{-14} s (i.e., < 1 μm) for the np states. With the spectrometers whose solid angle points towards the target, one then measures precisely the intensity of the prompt np → 1s Lyman transitions. A typical X-ray spectrum from a solid-state detector is displayed in Figure 4.1. Two major peaks are clearly visible. They are assigned to the Lyman α and β transitions while the less intense broad peak at higher energy is due to the sum of the remaining np → 1s Lyman lines with n > 3. With the high-resolution spectrometer, an efficient zoom of the low resolution spectrum is achievable, as shown in Figure 4.2. The full series of Lyman lines are recorded and very well separated up to n = 11. In addition, the fine structure components of the 2p level are resolved. In practice, in order to obtain the spectrum of Figure 4.2, we use two high resolution spectrometers. One spectrometer, with two equal arms of 1630 mm length, was specifically designed to record the fine structure components of the $2p_j$ → 1s transition and a resolution of ~2.5 eV at 3.8 keV is achieved. The second spectrometer, with two equal arms of 775 mm length, allows us to obtain precisely either the 3p - 4p → 1s transitions or higher members of the Lyman series from 5p up to the end with a resolution of ~6.5 eV or 8 eV, respectively. The curious reader may compare this spectrum with that of Figure 1 in reference [73] and note the improvement in terms of statistics and resolution mainly due to nowadays the great quality of the ion optics of the GANIL beams. Figure 4.3 exhibits a comparison between a solid foil and a gaseous target in the case of the observation of the $2p_{1/2}$ and $2p_{3/2}$ components. We can already notice that the intensity ratio $I(2p_{1/2})/I(2p_{3/2})$ is different from solid to gaseous target and will evolve with the target thickness highlighting the expected role of the Stark mixing between the $2s_{1/2}$ and $2p_{1/2}$ states (see § 2.1.3). The uncertainty for this ratio is reduced to a few % and is only due to statistical errors (no systematic uncertainties have to be considered since the two lines are recorded by the same detector). That's why this ratio provides a more stringent test than the $I(2p_{1/2})/I(2s_{1/2})$ ratio whose uncertainty is much larger (~ 20%) since the $2p_{1/2}$ and $2s_{1/2}$ → 1s are recorded independently by two different detectors. In addition to this intensity ratio, the entire spectrum enable us to extract the experimental number of emitted photons per incident ion, N_{np}^{exp}, for different thicknesses d via the line intensity $I_{\mathrm{np}\to 1s}$ using the following simple formula:

Eq. 20

$$N_{np}^{exp}(d) = \frac{I_{np\to 1s}(d)}{N_{proj}\,T_{np}}$$

where N_{proj} denotes the number of ion projectiles and T_{np} the total transmission for a line emitted by a given np state. To get the population, P_{np}^{exp}, N_{np}^{exp} is just divided by the branching ratio $B_{\mathrm{np}\to 1s}$.

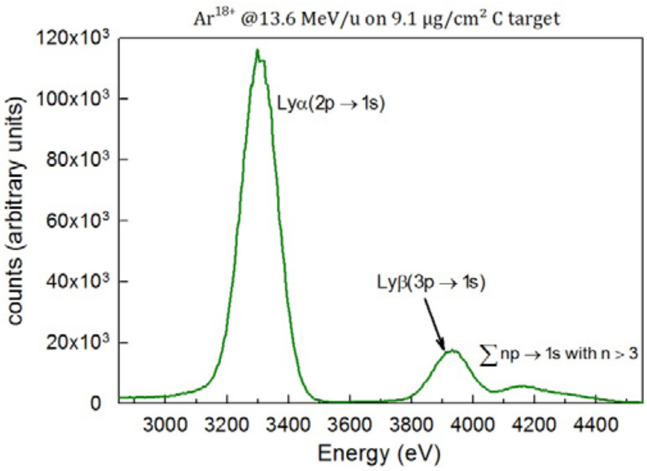

Figure 4.1: Low resolution spectrum of the Lyman series emitted by Ar^{17+} ions produced during the collision of Ar^{18+} ions at 13.6 MeV with a 9.1 µg/cm^2 (42 nm) carbon foil. Note: the photon energy is given in the projectile frame.

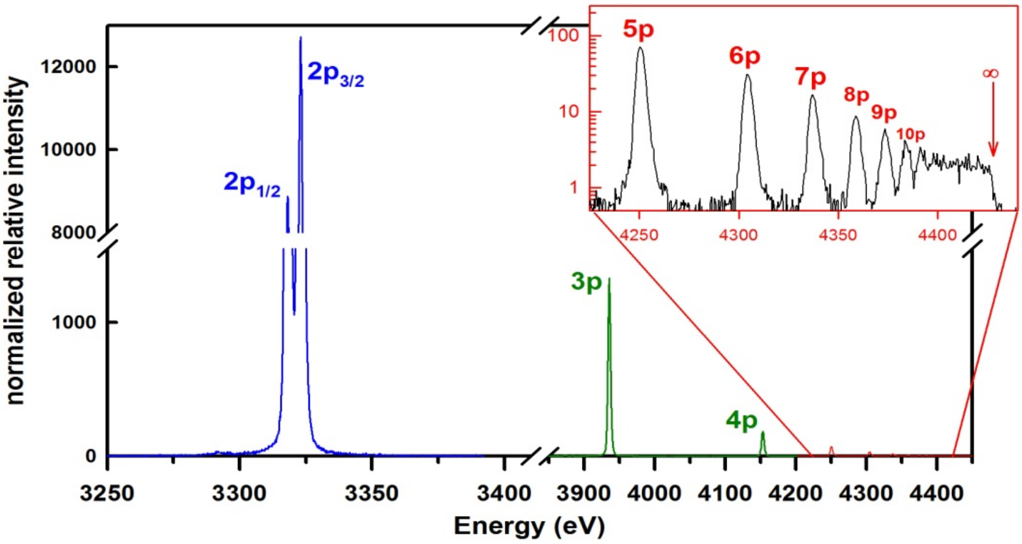

Figure 4.2: High resolution spectra of H-like X-ray transitions produced during the collision of Ar^{18+} ions at 13.6 MeV with a 47.2 µg/cm^2 (i.e. 220 nm) carbon target. All the np → 1s lines with n ∊ [2, ∞[are recorded by accumulating data over different Bragg angle settings of the spectrometer. For the 2p level, the two components 2p$_j$ with j = 1/2 and 3/2 are resolved. Note: the photon energy is given in the projectile frame.

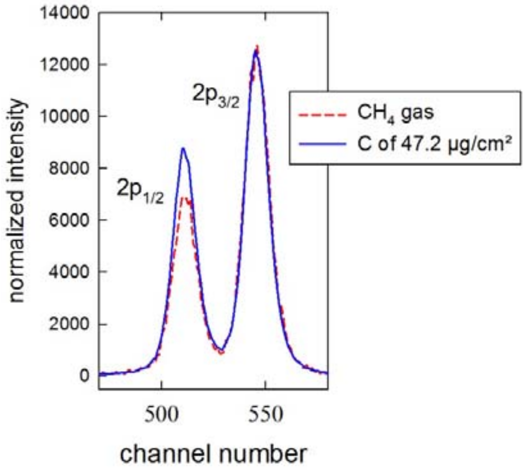

Figure 4.3: Comparison between the 47.2 µg/cm^2 solid foil and a CH$_4$ gaseous target in the case of the observation of the 2p$_j$ → 1s transitions (the two spectra are normalized to the 2p$_{3/2}$ component) emitted by Ar^{17+} ions at 13,6 MeV/u.

4.1.2 EMISSION OF Ar^{17+} DELAYED X-RAY TRANSITIONS

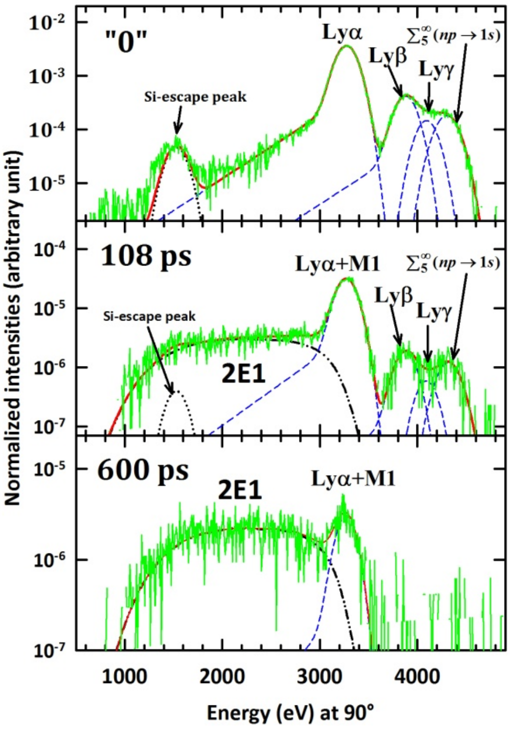

Figure 4.4: Spectra recorded by a Si(Li) detector at various ion times of flight (delay times) behind the 3.5 μg/cm² carbon target.

As seen in §2.1.1, the delayed X-ray emission recorded far from the target signs the production of nℓ-Rydberg states. With a small spatial window *ΔD* around a given distance *D* behind the target, a solid-state detector placed at 90° with respect to the beam direction is used to record the delayed Lyman intensities. Typical spectra obtained at three different distances (*D*) or, in other words at three different ion times of flight (ToF) behind the target, are shown in Figure 4.4 [74] for a given target thickness. For the largest ToF (600 ps), the np → 1s lines with n ≥ 3 have disappeared while the Lyman α is still visible. In fact, the Rydberg states with high angular momentum ℓ populated inside the target de-excite by cascade mainly to the 2p state and with a much smaller fraction to the other np (n ≥ 3) states. A broad peak that characterizes the two-photon decay mode (2E1) of the 2s metastable state is recorded as well. This transition is also visible on spectra shown in Figure 4.5 obtained at ToF ~2.5 ns when using a gaseous target and two different carbon foils. The presence of this peak is accompanied by the M1 (single-photon magnetic) line, the other decay mode of the 2s state, that is characterized by a narrow Gaussian peak at the same energy than the Lyman α line. In the case of the thicker target the helium-like M1 transition appears, revealing the production of the 1s2s metastable state inside the target. The contribution of this state to the X-ray emission from hydrogen-like ions has been subtracted.

Thanks to those spectra, we have measured precisely the evolution of the photon number for a given Lyman line, N_{np}^{exp} given by Eq. 20, with the ion time of flight behind the target. Moreover, for a given target thickness *d*, the 2s state population may be deduced from the 2E1 intensity, I_{2E1}, by:

Eq. 21
$$P_{2s}^{exp}(d) = \frac{I_{2E1}(d)}{2\, B_{2E1}\, N_{proj}\, T_{2s} \int_{D-\Delta D}^{D+\Delta D} e^{-z/z_{2s}}\, dz}$$

where B_{2E1} = 97% is the branching ratio for Ar^{17+}, N_{proj} the number of ion projectiles and T_{2s} the global transmission. I remind that the 2s lifetime of 3.5 ns translates into a propagation time z_{2s} = 173.6 mm with argon ions at 13.6 MeV/u.

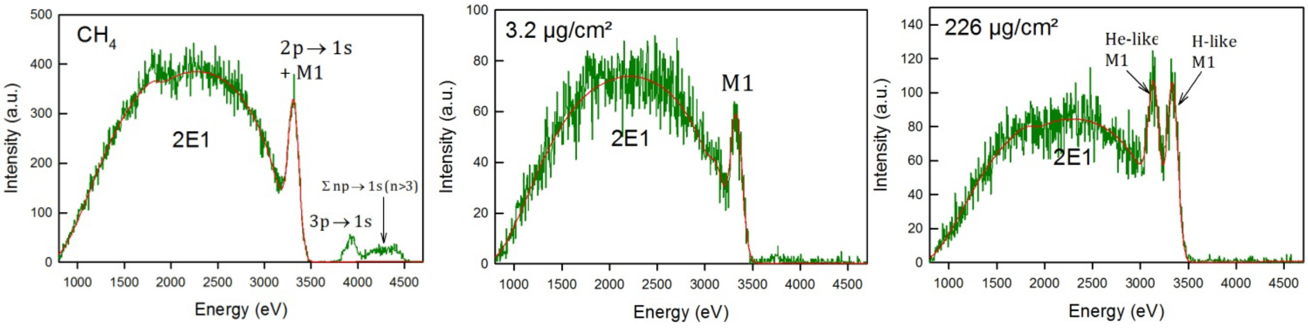

Figure 4.5: Spectra of the delayed X-ray transitions emitted by Ar^{17+} ions at 13.6 MeV and recorded by a solid-state detector placed at D = 127 mm behind the target (corresponding to an ion time of flight of 2.5 ns) for a CH_4 gaseous target and two carbon foils (3.2 and 226 μg/cm²). The 2E1 decay mode as well as the M1 one from the de-excitation of the 2s state are clearly distinguishable. Note: the photon energy is given in the projectile frame.

4.2 IN THE CONTEXT OF THE LASER – CLUSTER INTERACTION

Rare gas clusters of argon, krypton and xenon have been produced and submitted to 800 nm laser pulses of intensity in the 10^{14}-10^{17} W/cm^2 intensity range. X-ray spectra are presented and precisely analyzed in [55]. High resolution spectra obtained with Xe clusters are found in [55] and [48]. Here, I just present spectra obtained with argon clusters. I remind that our goal is to measure i) the absolute X-ray yields and ii) the charge state distribution of ions responsible for this X-ray emission.

4.2.1 LOW RESOLUTION SPECTRA

For an accurate determination of photon yields, one uses two solid-state detectors: one is specially designed to have a low transmission and works in the very low counting rate regime while the other running in parallel is suited to record moderate to high counting rates, taking advantage of the pileup mode. This very clever trick gives access to photon yields over several orders of magnitude without any modification of the experimental setup. Figure 4.6 shows spectra recorded at different counting rates when argon clusters are submitted to 800 nm laser pulses. For single-photon spectra as Figure 4.6(a), the counting rate is significantly reduced (much less than one photon per laser pulse is recorded): the detector signal is just proportional to the mean photon energy $< E_{1h\nu} >$. For higher counting rates (~ 1 photon per pulse), several photons can be detected within one laser shot and pileup occurs: peaks at 2, 3, 4… times the energy of the single photon peak are observed and the intensity of each peak follows a Poisson statistics as shown in Figure 4.6(b). For very high counting rates, the previous Poisson distribution tends to a Gaussian distribution: the mean energy of the distribution $< E_{Nh\nu} >$ corresponds to the pile-up of N photons of $< E_{1h\nu} >$ each (i.e., 3.1 keV in this case). In Figure 4.6(c) almost 20 photons of 3.1 keV are detected simultaneously. Finally, the number of detected photons per laser shot is given by:

Eq. 22
$$\bar{n}_X = \frac{<E_{Nh\nu}>}{<E_{1h\nu}>} \times \frac{N_{counts}}{N_{shots}}$$

with N_{counts} the total number of counts in the spectrum and N_{shots} the number of laser shots. By dividing $\bar{n}_X$ by the total transmission of the detector, we deduce the absolute photon yields recorded for different experimental conditions.

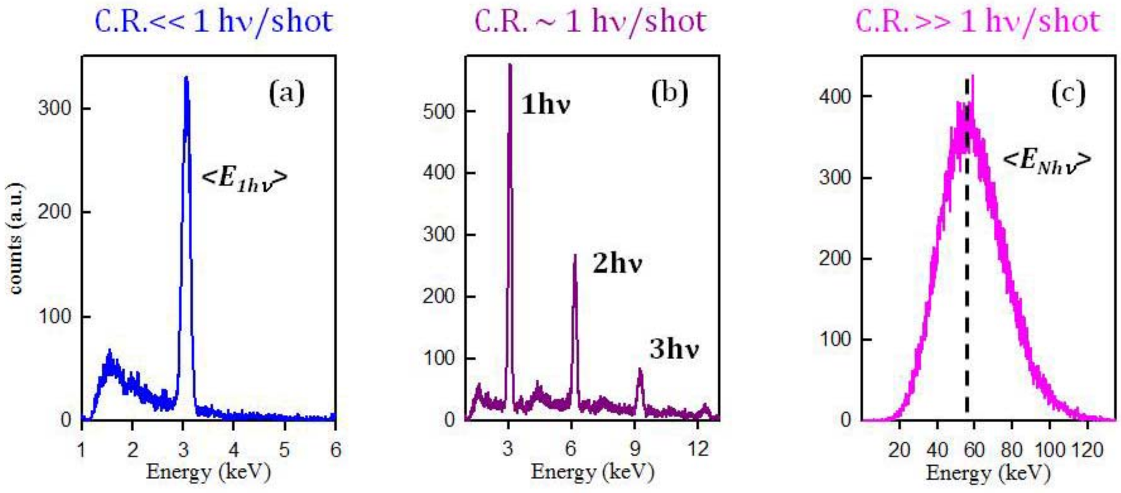

Figure 4.6: X-ray spectra recorded by solid-state detectors and obtained after irradiation of large argon clusters with ~60fs infrared laser pulses. (a) single photon spectrum recorded at a reduced counting rate (C.R.) that gives the value of the mean photon energy $< E_{1h\nu} >$. (b) spectrum at a C.R. close to one photon recorded within one laser shot that exhibits a Poisson distribution. (c) spectrum at a very large C.R. characterized by a Gaussian distribution whose position ($E_{Nh\nu}$) provides the total number of emitted keV photons.

4.2.2 HIGH RESOLUTION SPECTRA

With the crystal spectrometer, one can obtain a zoom of the single photon spectrum. Figure 4.7 displays the $1s2pn\ell \rightarrow 1s^2n\ell$ transitions emitted when argon clusters are under laser irradiation for a given pulse duration. Broad peaks are recorded together with a well separated narrow peak corresponding to the $1s2p\ {}^1P_1 \rightarrow 1s^2\ {}^1S_0$ transition in helium-like argon. The ${}^3P_1 \rightarrow {}^1S_0$ transition is also clearly visible. The broader peaks are assigned to a large set of configurations of ions with a K-shell vacancy and charge states of 15+, 14+, 13+ and 12+ roughly separated by ~ 20 eV (although some configuration mixing occur). This allows us to correctly extract the charge state distribution of ions emitting the keV photons. Figure 4.8 is obtained under the same experimental conditions (same pulse duration, same cluster size) but for an energy/pulse that has been drastically reduced. We can note that even at a laser intensity of $2\ 10^{15}$ W/cm² Ar^{16+} ions are still produced. With a control of the different parameters governing the laser-cluster interaction, we are then able to follow the evolution of this charge state distribution as a function of a given parameter as in Figure 4.9 for which only the pulse duration is varied.

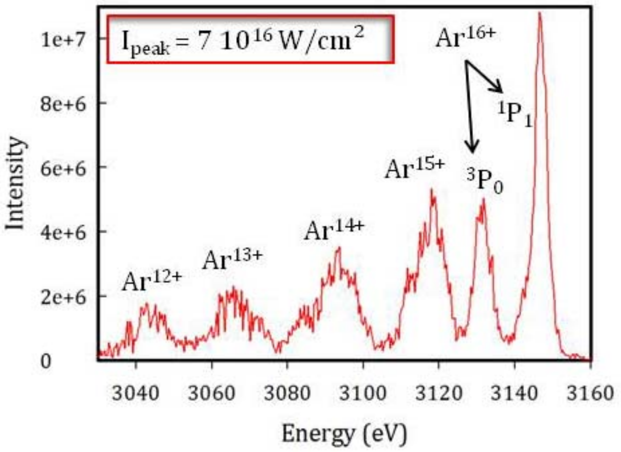

Figure 4.7: $1s2pn\ell \rightarrow 1s^2n\ell$ high-resolution spectrum recorded during the interaction of large argon clusters (P_0 = 40 bar) with 800 nm laser pulses of τ ~ 55 fs. This spectrum is a zoom of the single photon spectrum recorded by a solid state detector.

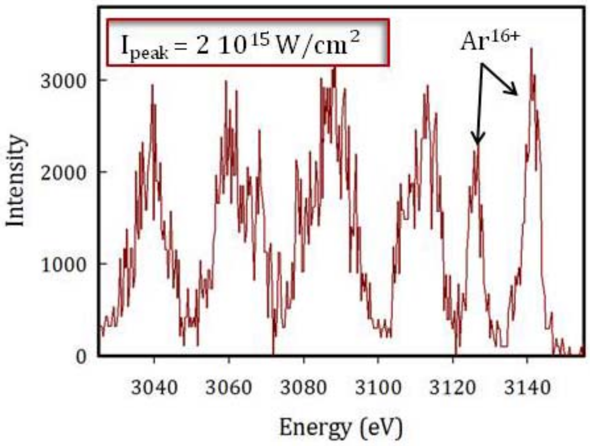

Figure 4.8: same as Figure 4.7 but at laser intensity 35 times lower.

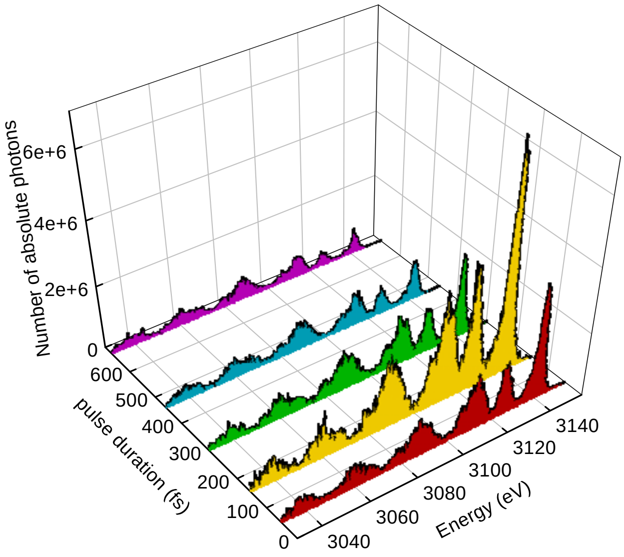

Figure 4.9: Same as Figure 4.7 with laser energy of 20 mJ and for several pulse durations from 60 to 680 fs.

5. THEORETICAL APPROACHES

The description of the interaction of either an ion or an intense laser pulse with complex matter such as a cluster or a solid foil is a theoretical challenge given the number of partners who may be involved in the dynamics and the large variety of processes to be considered.

The ion-solid interaction represents a good example of a small open system in contact with a large reservoir. The open system is the internal state of a fast hydrogen-like ion while the reservoir consists of the radiation field and the particles of the solid that induce energy exchange and decoherence in the small system. The total Hamiltonian is given by:

$$H = H_S + H_R + V_{SR} \tag{Eq. 23}$$

where H_S is the Hamiltonian of the small system, H_R the one of the reservoir (it is worthwhile to mention that the variation of the reservoir state due to its coupling with the small system is negligible) and V_{SR} corresponds to the coupling between the system and the reservoir. The time dependence of the density operator $\rho(t)$ describing the global system (also named the density matrix) is then given by the Liouville von Neumann equation,

$$i\frac{d}{dt}\rho(t) = [H, \rho(t)] \tag{Eq. 24}$$

a solution of which is out of reach. Instead, we focus on the reduced density operator $\sigma(t)$ that contains all the information about the internal state of the ion (the small system). $\sigma(t)$ can be obtained by tracing $\rho(t)$ with respect to the degrees of freedom of the environment. We may then show that the time evolution of $\sigma(t)$ follows the Liouville equation including a dissipative term:

$$i\frac{d}{dt}\sigma(t) = [H_S, \sigma(t)] + R\sigma(t) \tag{Eq. 25}$$

with R the relaxation operator describing the interaction of the small system with the reservoir. In the following paragraphs (§5.1.1 and 5.2), I shortly describe how this equation can be solved.

For the laser-cluster interaction, we examine in a first step the dynamics of a *single* cluster consisting of $\sim 10^4$ – 10^5 atoms. An argon cluster has been considered for the simulations. Contrary to the ion-solid interaction, all the particles of the cluster participate to the interaction dynamics leading to the emission of energetic particles, photons up to hard X-rays and towards a complete disintegration of the cluster. Due to the large number of particles, we therefore opt for an effective mean-field approach using a generalization of classical trajectory Monte Carlo simulations first developed for the ion-solid interaction and presented in the first part of this chapter.

In the following, I just point out the theoretical bases of two methods we used to describe the interaction dynamics. Atomic units are used unless otherwise stated.

5.1 CLASSICAL APPROACH: THE LANGEVIN EQUATION

Using a classical description offers the possibility to solve quite simply the equations of particle motion using Monte Carlo simulations. The classical approach discussed in this manuscript, first developed by J. Burgdörfer and co-workers [75], defines a test-particle ensemble that obeys a stochastic equation of motion, namely the Langevin equation.

5.1.1 TRANSPORT OF FAST HYDROGEN-LIKE IONS IN A SOLID

The theoretical description described in the sub-section has been successfully applied to the stripping of relativistic H^- and H through thin foils [76]. From there, in collaboration with B. Gervais (CIMAP, Caen), I have applied this approach to our collision system of interest (Ar ions on carbon foils). Classically using the Poisson brackets, the equation Eq. 25 becomes:

Eq. 26
$$\frac{\partial}{\partial t}\sigma(\boldsymbol{r},\boldsymbol{p},t) = \{\mathcal{H}_S,\sigma(t)\} + \mathcal{R}\sigma(t) \quad with \quad \mathcal{H}_S = \frac{p^2}{2} - \frac{Z_p}{r} + V_{scr}(\boldsymbol{r})$$

$\sigma(\boldsymbol{r},\boldsymbol{p},t)$ is the reduced probability density in the classical phase space where $\boldsymbol{r}$ and $\boldsymbol{p}$ are the position and momentum vectors of the electron in the frame of its parent ion. $\mathcal{H}_S$ is the atomic Hamiltonian which contains the Coulomb interaction potential possibly modified by the wake potential $V_{scr}(\boldsymbol{r})$ (also named dynamical screening) and $\mathcal{R}$ the operator for the interaction with the environment. Rather than solving this equation, the classical theory developed here proceeds by employing test-particle discretization. At $t = 0$, the probability density is deduced from the primary population process of the ion states providing an ensemble of initial phase points $(\boldsymbol{r_i}(0),\boldsymbol{p_i}(0))$. Chosen by Monte Carlo sampling within this initial ensemble, test particles (electrons) obey then the Langevin equation,

Eq. 27
$$\dot{\boldsymbol{p}} = -Z_p\frac{\boldsymbol{r}}{r^3} + \boldsymbol{F}_{stoc}(t)$$

where the wake potential is first neglected. This equation describes the motion of the electron on a classical orbit disturbed by a stochastic force $\boldsymbol{F}_{stoc(t)}$. The difficulty lies in the determination of this force that includes the dissipative interactions of our open system with its environment so as to establish a full correspondence between Eq. 26 and Eq. 27. We describe $\boldsymbol{F}_{stoc(t)}$ in terms of a sequence of impulsive momentum transfers ("kicks"):

Eq. 28
$$\boldsymbol{F}_{stoc}(t) = \sum_{\alpha=1,2}\sum_i \Delta\boldsymbol{p}_i^\alpha \;\delta(t - t_i^\alpha)$$

with $\Delta\boldsymbol{p}_i^\alpha$ the stochastic momentum transfer per collision at the time t_i^α. The approximation of the collisional interactions of fast projectile electrons with target atoms in terms of instantaneous momentum transfers is based on the fact that the collision time (τ_{AC}) is short compared to the orbital period ($2\pi\,\mathrm{n}^3 Z_p^{-2}$) of the electron in a hydrogenic n level. The determination of $\boldsymbol{F}_{stoc}(t)$ is thereby reduced to that of a stochastic sequence of pairs ($\Delta\boldsymbol{p}_i^\alpha$, t_i^α). Two series of scattering are included:

- elastic scattering calculated using phase shift analysis and corresponding to the projectile electron – screened target nucleus interaction ($\alpha = 1$);
- inelastic scattering obtained through the dielectric response of the medium and describing the projectile electron – target electron interaction ($\alpha = 2$).

Details of the collision kernels determining the momentum transfers and the times in between collisions are extensively described in [75] and [77] and summarized in my PhD thesis [27] for the transport of Ar^{17+} ions at 23 a.u. inside carbon foils. The physical description of the classical transport theory can be visualized as a "random flight" problem along a sequence of Kepler orbits or equivalently as a random walk through bound and continuum states of the Coulomb problem (Figure 5.1). Indeed, such a classical approach has the advantage that electrons in the continuum can be treated exactly including both ionization and electron recombination in the continuum.

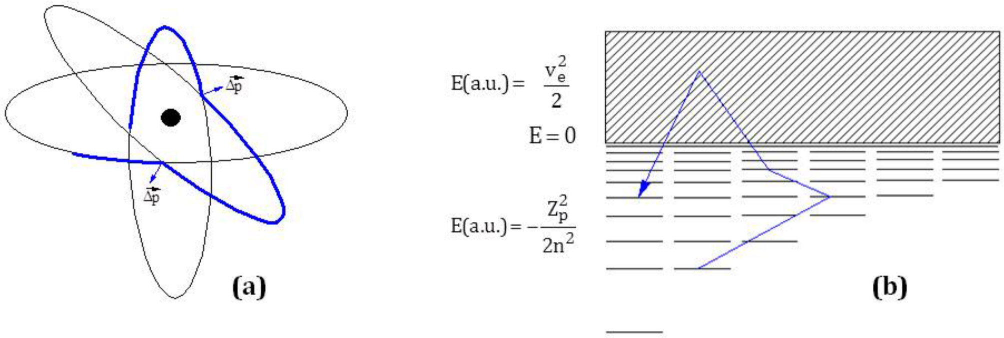

*Figure 5.1: Random walk of an electron in the hydrogen ion due to multiple scattering: **(a)** Sequence of classical Kepler orbits generated by collisional momentum transfers and **(b)** random walk in the Coulomb state space.*

Taking into account the interaction potential of the electron with the wake field gives rise to an additional force in Eq. 27 that is $-\boldsymbol{\nabla}_r V_{scr}(\boldsymbol{r})$. The Coulomb potential symmetries are broken due to the presence of this field and the resulting potential has only the symmetry of revolution around the beam axis defined by $\boldsymbol{v_p}$ making the numerical integration of electron trajectories computationally much slower. We have suggested a method of calculation discussed in [74] for the lowest energy orbits ($\mathrm{n} \leq 3$ for argon) exploiting the secular approximation that gives the evolution of the angular momentum and Lenz vectors while trajectories for higher energy orbits are explicitly calculated.

The final energy distributions at the exit of the foil are continuous. For a comparison with the experimental populations of bound states, it is then necessary to project the classical phase-space defined by $\boldsymbol{r}$ and $\boldsymbol{p}$ on the nℓ quantum phase-space: the energy comprises between $Z_p^2/2(\mathrm{n}-1/2)^2$ and $Z_p^2/2(\mathrm{n}+1/2)^2$ is associated to the principal quantum number n and the angular momentum whose final value is between ℓ and $\ell + 1$ to the integer value ℓ. Figure 5.2 presents population probabilities of Ar^{17+} at 23 a.u. at the exit of a 201 μg/cm^2 carbon foil: Figure 5.2(a) with transport effect only due to collision events ([27] and [78]), Figure 5.2(b) for n = 5 with transport effect including the wake field or not ([79]). From this latter, we clearly observe a huge difference with the population obtained from a binary ion-atom collision that populates predominantly the p ($\ell = 1$) states by capture. Indeed, the subsequent transport process rearranges the mixture of states so that diffusion into larger angular momentum states occurs leading even to a statistical (2ℓ+1) limit for the thickest target when both wake field and collisions are involved. Finally, comparison with experiment is made possible by including in the simulation the post-foil interaction cascade processes.

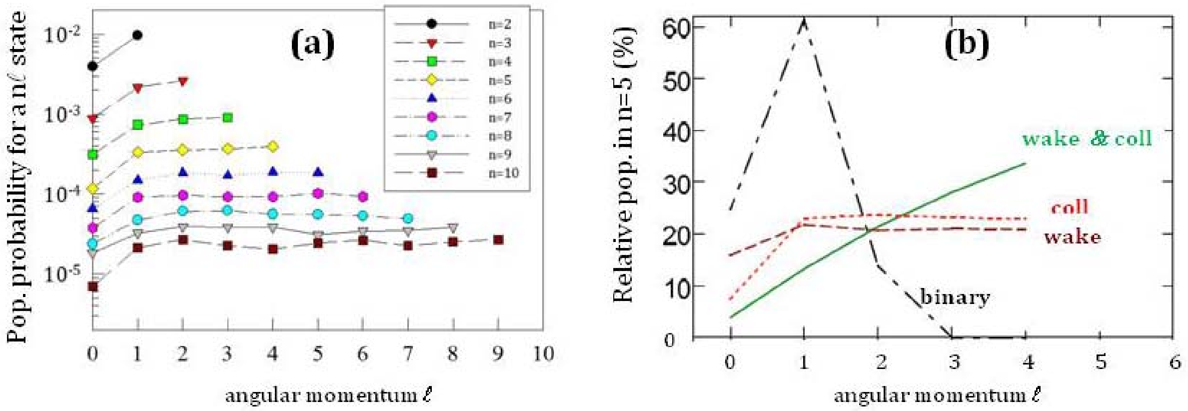

Figure 5.2: P(nℓ) populations of Ar^{17+} at 23 a.u. at the exit of a 201 μg/cm^2 carbon foil from the classical transport theory: ***(a)*** *[27] simulations for n = 2 up to 10 without the wake field effect;* ***(b)*** *[79] simulations for n = 5 involving only the collision events (red curve), only the wake field (brown curve) or both (green curve). For comparison binary ion-atom collision (i.e., without any transport effects) is also presented.*

With this classical method (referred to Classical Transport Theory CTT in the following), we do not represent the effects related to the spin of the electron and the radiative decay. As a result, the classical approximation will be only valid for Z_p ions not too heavy for which the spin-orbit coupling is rather weak and the radiative decay times long enough compared to the ion transit time inside the solid. The transport of Ar^{17+} ions at 23 a.u. in carbon foils has been examined with this approach (only ≈ 4% of excited states -mainly the 2*p* state- decay inside the thickest carbon target). We may add as well that the use of a classical phase space is more suitable to interpret the production of Rydberg states in solids since no limitation in the number of states involved has to be considered.

5.1.2 DYNAMICS OF LARGE CLUSTERS UNDER STRONG FIELD

I remind that among the different approaches developed in the context of the laser-cluster interaction ([58],[59],[80]), none of them were focused on the production of keV X-rays from large clusters. The dynamics of charged particles was considered to try to explain some features observed in ion or electron spectroscopy as, for instance, the ion charge state distribution in the laser-induced Coulomb explosion [81]. Thanks to our knowledge in ion-matter interaction, we have considered a similar approach to model the laser-cluster dynamics. So, still in collaboration with the Vienna's group, we have employed a generalization of classical trajectory Monte Carlo simulations based on a mean-field approach ([61], [82]) so as to be able to treat the dynamics of large clusters. This approach is completely developed in the PhD thesis of C. Deiss [63] (Group of J. Burgdörfer, 2009). As previously discussed, many-particle effects are included via stochastic processes. A representative fraction of ions and electrons obeys the following Langevin equations, respectively:

Eq. 29

$$\dot{\boldsymbol{p}}^{(ion)} = \tilde{q}(t)\left(\boldsymbol{F}_{Laser}(t) + \boldsymbol{F}_{mean}\left(\boldsymbol{r}^{(i)}, t\right)\right) \ \ and \ \ \dot{\boldsymbol{p}}^{(electron)} = -\boldsymbol{F}_{Laser}(t) - \boldsymbol{F}_{mean}\left(\boldsymbol{r}^{(e)}, t\right) + \boldsymbol{F}_{stoc}\left(\boldsymbol{r}^{(e)}, \boldsymbol{p}^{(e)}, t\right)$$

The number of explicitly treated particles (i.e., the representative fraction) depends on computer capabilities, cluster size and pulse length. $\tilde{q}(t)$ is the time-dependent screened ionic charge state estimated by the local number of quasi-free electrons per ion [83]. $\boldsymbol{F}_{Laser}(t)$ stands for the uniform time-dependent laser field linearly polarized while $\boldsymbol{F}_{mean}(\boldsymbol{r}, t)$ is the mean field felt by each particle due to the proximity of other charged particles (the positions of all the test-particles have then to be known). A precise computational evaluation of this mean field on a cylindrical grid is detailed in [63]. Momentum changes of the electrons due to collision processes are taken into account by the stochastic force $\boldsymbol{F}_{stoc}\left(\boldsymbol{r}^{(e)}, \boldsymbol{p}^{(e)}, t\right)$ that includes a large variety of processes. Elastic electron-ion scattering is controlled by the probability of each electron to scatter elastically during a time step which is determined by the energy and charge state dependent total elastic scattering cross-section, the local ionic density and the velocity of the electron. If the electron scatters, the scattering angle is determined randomly according to the differential cross-sections for which an example is given in Figure 5.3 ([61] and [63]). Note that the use of parameterized Hartree-Fock potentials ensures a proper description of large angle scattering. Further contributions are electron impact ionization, electron-impact excitation from L-shell to M-shell followed by impact ionization (both being evaluated through the Lotz formula [55]), electron-electron scattering as well as further ionization mechanisms like Auger decay of L-shell vacancies, over barrier field ionization and tunnel ionization. The key point is that the necessary input data can be determined and tabulated independently from the simulation.

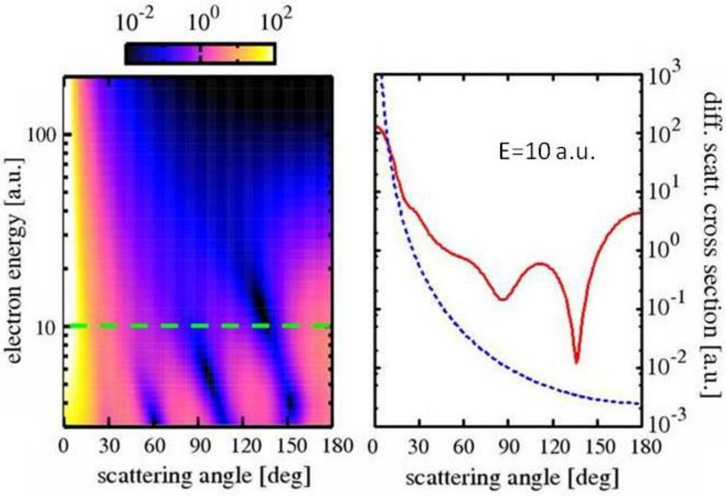

Figure 5.3: Left: Differential cross-section distribution $d\sigma_e/d\Omega$ in a.u. for elastic electron scattering at Ar^{2+} ions. Right: $d\sigma_e/d\Omega$ for an electron with fixed kinetic energy E =10 a.u. (solid red line) using partial wave analysis of parameterized Hartree-Fock potentials. For comparison, the Rutherford cross section is also displayed (dashed blue line).

As the ionic and electronic dynamics proceed on different time scales, the onset of cluster expansion can be taken into account through the parametric variation of the radius $R(t)$ of the uniform spherical charge $Q(t)$ background representing the ions of mass M in their time-dependent mean charge state $\tilde{q}(t)$:

Eq. 30

$$M\frac{d^2}{dt^2}R(t) = \frac{\tilde{q}(t)\,Q(t)}{R^2(t)}$$

Simulations with an argon cluster submitted to short ($\tau_{pulse} \geq 50fs$) infrared (800 nm) laser pulses linearly polarized have been performed to predict X-ray yields and the ionic charge state distribution responsible for this emission.

The most striking result from the simulations comes from the observation of the electron dynamics inside and around the cluster [62]. As soon as the laser pulse reaches the threshold intensity for optical field ionization of neutral atoms (i.e., a few 10^{14} W/cm^2), a nanoplasma of high electronic density ($\sim 10^{22}$ cm^{-3}, i.e., ~ 1 electron/atom)) is formed providing the initial conditions for the propagation of Eq. 29. Then, the electron cloud is collectively driven by the laser field with respect to the ionic background. The number of electrons rapidly increases due to efficient further ionization. In the same time, efficient heating of a sub-ensemble of electrons up to energies in the keV range take place. Indeed, strong enhanced electric fields at the cluster poles due to the combined action of the cluster charging up coming from outer ionization (some electrons may leave the cluster) and the polarization of the cluster (due to the rapid motion of electrons compared to the ions) are found to cause the production of these fast electrons. In Figure 5.4 an example of the strong asymmetry of the electric field strength is shown; the situation at the cluster poles is inversed after half each laser cycle (see [62]). When following the electron dynamics during half a laser cycle, we may observe that a fraction of slow electrons can leak out of the cluster. As soon as the strong enhanced electric field builds up, these electrons are strongly accelerated back into the cluster and travel through the cluster with energy high enough to ionize the Ar atoms or ions inside the cluster.

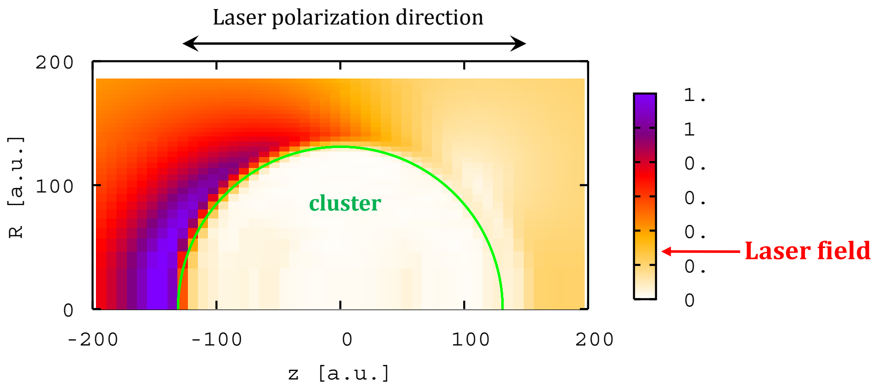

Figure 5.4: Spatial distribution of the electric field strength (the color scale is given in a.u.) exhibiting a strong asymmetry.

For a comparison with the experimental data, the probability for an electron with energy E and velocity $v^{(e)}$ during the step time Δt to produce K-shell ionization is evaluated by:

Eq. 31

$$P_K = \sigma_K(E)\rho^{(ion)}(t)\, v^{(e)}\, \Delta t$$

where $\rho^{(ion)}(t)$ is the time dependant ionic density. Furthermore, by taking into account the fluorescence yield and the laser intensity profile, i.e., the number of clusters submitted to a given laser intensity linked to the effective focal volume (Eq. 3 §1.2.2), we obtain the absolute X-ray yield directly comparable with what is extracted from the experiment (Eq. 22 §4.2).

5.2 QUANTUM DESCRIPTIONS FOR ION-SOLID INTERACTION: HOW TO SOLVE THE QUANTUM LIOUVILLE EQUATION?

The classical approach in §5.1.1 gives only access to the nℓ populations of projectile excited states after the transport phase in a solid while the explicit treatment of coherences requires to apply quantum transport methods. Two approaches have been used to solve the quantum Liouville equation Eq. 25: the Master Equation Approach ([31], [30]) developed by our group in collaboration with L.J. Dubé and the Quantum Transport Theory ([39], [84]) initiated by the groups of J. Burgdörfer and C.O. Reinhold.

5.2.1 *MASTER EQUATIONS APPROACH (MEA)*

First of all, I would like to mention that the simplest approximation to the Liouville equation consists of neglecting the couplings between the off-diagonal matrix elements and the diagonal matrix elements of the reduced density matrix. This reduces the problem to the resolution of differential coupled equations giving the time evolution of the excited nℓ state populations of a hydrogen-like ion,

Eq. 32
$$\frac{d}{dt}\sigma_{aa}(t) = \sum_{a'\neq a}\left[\Gamma_{a'a}\,\sigma_{a'a'}(t) - \Gamma_{a\,a'}\,\sigma_{aa}(t)\right].$$

where a denotes a given nℓ state. $\Gamma_{a'\,a}$ stands for the transition rates per unit time from state a' to state a induced by the environment through the collisions and the radiative decay. This set of equations is usually referred to as *rate equations*. Atomic cross sections of capture, ionization, intra-shell (Δℓ = ±1 and ±2) and inter-shell (Δn = ±1 and ±2) excitation, as well as radiative transitions are first calculated. By taking into account all the states up to n = 10, 54 coupled equations are hence obtained. Those rate equations provide a reasonable description of the major part of the nℓ population evolution with the solid target and of the evolution of the delayed X-ray emission behind a target (see §6.1.1 and 6.1.2). The ETACHA code predicting the evolution of the ion projectile charge state distributions with the solid target thickness is also based on rate equations [24].

However, clear evidence of limitation appears when dealing with the observation of the fine structure components due to the disregard of coherences. Nevertheless, still by using an approach of coupled differential equations (possible when the approximation of independent variation velocities is satisfied, see the work of C. Cohen-Tanoudji, J. Dupont-Roc and G. Grynberg [85]), one may establish the time evolution of coherences $\sigma_{ab}(t)$ (coherence between states a and b) and of populations $\sigma_{aa}(t)$ both being coupled. These coupled equations, named *master equations*, may be succinctly written in a given sub-space as,

Eq. 33
$$\frac{d}{dt}\sigma_{ab}(t) = \{i\omega_s(a,b)[\sigma_{aa}(t) - \sigma_{bb}(t)]\} + \left\{-i\omega_{ab}\sigma_{ab}(t) - \frac{\Gamma_{ab}}{2}\sigma_{ab}(t)\right\} \quad for\ a \neq b$$

Eq. 34
$$\frac{d}{dt}\sigma_{aa}(t) = \{i\,\textstyle\sum_c \omega_s(c,a)[\sigma_{ac}(t) - \sigma_{ca}(t)]\} + \{\textstyle\sum_{c\neq a}[\Gamma_{ca}\,\sigma_{cc}(t) - \Gamma_{ac}\,\sigma_{aa}(t)]\}$$

$\omega_s(a,b)$ is the Stark mixing element (Eq. 9 §2.1.3). $\omega_{ab} = E_a - E_b$ represents the Bohr frequency between states a and b. All the transitions rates Γ_{ij} are calculated via the cross sections in a nℓ$\mathrm{jm_j}$ basis. For the coherences, the first term in Eq. 33 denotes the coupling with the populations induced by the wake field while the second term includes radiative and collisional damping. For the populations, the coupling with the coherences appears in the first term of Eq. 34 while the second term is fully equivalent to Eq. 32. We must add that Eq. 33 neglects the collisional couplings between σ_{ab} with density matrix elements involving states c other than a and b. In other words, the damping of coherences through collisions is probably not so well taken into account with this approach. So far, all the sub-states of the n = 1 – 6 shells are included in the treatment. Actually, we found that convergence of calculations is reached around n = 6 (changes when going from n = 5 to 6 do not exceeds a few %). The number of atomic cross sections and coherence terms, that should be calculated, is of 4195 cross sections and 245 terms of coherence for the transport of argon ions in carbon giving indeed a limitation to this type of treatment. Nevertheless as soon as those elements are calculated, a few minutes on a PC computer are enough to solve the master equations. Figure 5.5 shows the transport effects on the Ar^{17+} (23 a.u.) 2p and 2s populations. It can be noted that the 2s state is much more rapidly (i.e., for a small target thickness) affected than for the 2p state by those effects. For this latter, transport effects start to be important only from a carbon thickness of $\sim 20\ \mu g/cm^2$. Moreover, the $2s_{1/2}$ population is more sensitive to the wake field than the 2p one that represents an average population between the $2p_{1/2}$ and $2p_{3/2}$ sub-states. More generally, the nℓ populations are expected to be less sensitive to the coherence terms than the fine structure components. Indeed, the sensitivity to the coherence parameter and to the coherence phase values appears in the study of fine structure population ratios as, for instance, $2p_{1/2}/2p_{3/2}$ in the case of argon or $3p_{1/2}/3s_{1/2}$ in the case of krypton. This is illustrated in Figure 5.6 that exhibits the variation of the $3p_{1/2}/3s_{1/2}$ population ratio for Kr^{36+} at 35.6 a.u. on carbon foils when the coherence phase between the $3s_{m=0}$ and $3p_{m=0}$ states of the primary population process (here the capture) is varied from 0° to 270°. This theoretical method is part of the PhD thesis of C. Fourment [31].

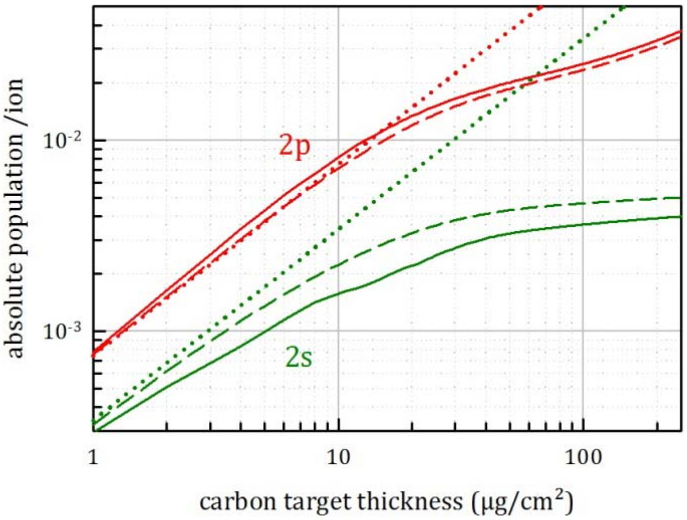

Figure 5.5: Evolution of the Ar^{17+} (23 a.u.) 2p and 2s populations with the target thickness obtained with the Master Equation Approach: solid line for the full calculations and dashed line for calculations without the wake filed. The dotted lines are for the binary ion-atom collision, i.e., without any transport effects.

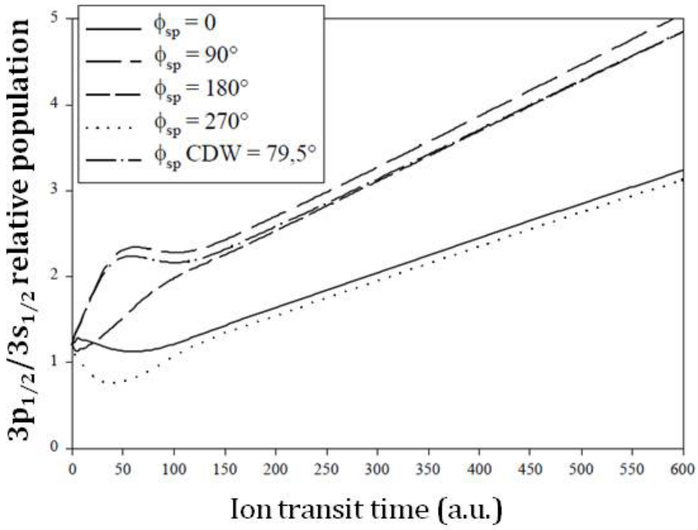

Figure 5.6: Evolution the $3p_{1/2}/3s_{1/2}$ ratio predicted by the Master Equation Approach with the ion transit time (i.e., the target thickness) for the collision system Kr^{36+} at 35.6 a.u. on carbon. Various coherence $3s_0 3p_0$ phases of the initial capture process (the value given by the CDW approximation is 79.5°) is taken in the calculations.

5.2.2 QUANTUM TRANSPORT THEORY (QTT)

The quantum transport theory (QTT) described here has been developed after the Master Equation Approach to eventually overcome the problem of coherence transport and its limit in the number of states to be considered. The QTT method can be considered as a quantized version of the corresponding classical transport theory (CTT in §5.1.1). The starting point of such a description is the possibility to write the relaxation operator R in Eq. 25 using the Lindblad approach ([86] and [84]). This insures the possibility to solve the quantum Liouville equation by means of a quantum trajectory Monte Carlo technique (first used in quantum optics for the description of few-state atomic systems interacting with the radiation field, see for example J. Dalibard et al [87]). The reduced density operator $\sigma(t)$ of the system is constructed from the independent evolution of an ensemble of N_{traj} pure states

Eq. 35
$$\sigma(t) = \frac{1}{N_{traj}} \sum_{\mu}^{N_{traj}} |\psi^{\mu}(t)\rangle\langle\psi^{\mu}(t)|$$

where μ labels the different stochastic realizations of quantum trajectories. Each of the wave functions $|\psi^{\mu}(t)\rangle$ is called a quantum trajectory and describes a different random sequence of interactions with the environment. The time evolution of $|\psi^{\mu}(t)\rangle$ is governed by a non-linear stochastic Schrödinger equation. Alternatively, it can be calculated from the corresponding time evolution operator, $U^{\mu}(t,0)$, which can be decomposed into a sequence of products of continuous time evolution operators and discontinuous jump operators. As a result, we have:

Eq. 36
$$|\psi^{\mu}(t)\rangle = U^{\mu}(t,0)|0\rangle \quad with \quad U^{\mu}(t,0) = U^{\mu}_{cont}(t,t_n) \prod_{j=1}^{n} U^{\mu,j}_{jump}\, U^{\mu}_{cont}(t_j, t_{j-1})$$

where $|0\rangle$ is an initial state populated by a stochastic feeding process. The operators $U^{\mu,j}_{jump}$ represent discontinuous changes of the wave function, i.e., stochastic jumps at randomly chosen times t_j (from the corresponding mean free paths of various involved processes). The operators $U^{\mu}_{cont}(t_j, t_{j-1})$ describe the continuous change of the wave function during the time period (t_{j-1}, t_j) between stochastic "jumps". This approach accounts for both the transient build-up and destruction of coherences by stochastic processes but is finally also limited by the number of states that can be taken into account (due to time consuming for the calculations). Figure 5.7 illustrates the application of the QTT to the transport of 47 a.u. Kr^{35+} ions through carbon foils initially populated by the single excitation process. It shows the time development of the electron density matrix as the ion propagates through the foil, i.e., for four different propagation lengths. Specifically, density plots of the coherence parameters, C_{ab}, are displayed in the *a,b* plane of the bound states of the electron with

Eq. 37
$$C_{ab} = \frac{|\sigma_{ab}|}{\sqrt{\sigma_{aa}\,\sigma_{bb}}}$$

We have $0 \leq C_{ab} \leq 1$ (a fully coherent ensemble is characterized by $C_{ab} = 1$). Hence, C_{ab} only provides information about the relative strength of off-diagonal coherences. For increasing propagation length the system becomes nearly incoherent (i.e. C is nearly diagonal), but for short propagation lengths many coherences reach their maximal amplitudes [84] and [88].

A full description of this theoretical method is included in the PhD thesis of M. Seliger [32] (Group of J. Burgdörfer, May 2005).

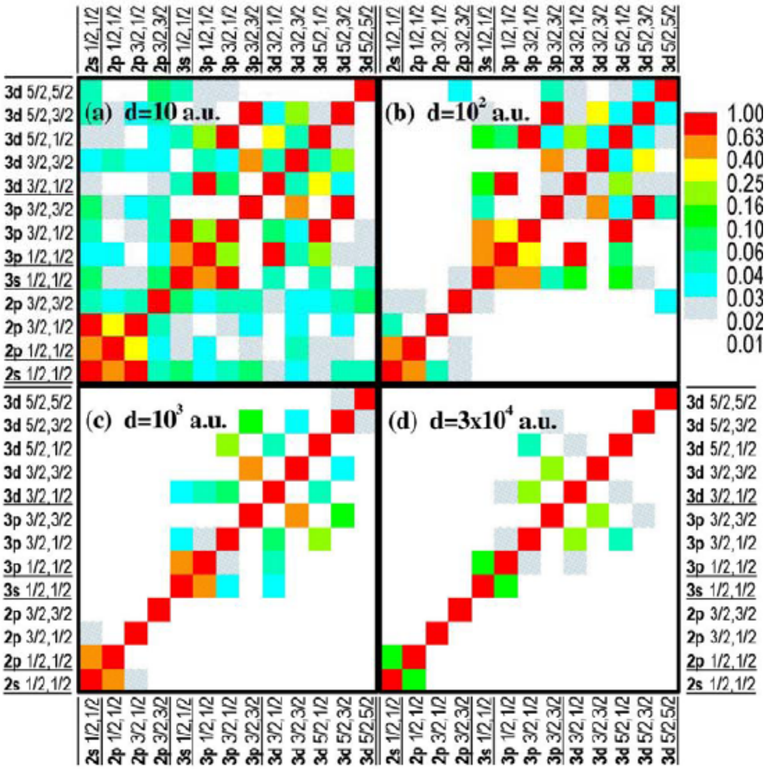

Figure 5.7: Relative coherences C_{ab} of the density matrix in the fine structure basis for the internal state of a 60MeV/u Kr^{35+} ion traversing amorphous carbon following various propagation lengths (d from 10 to 3 10^4 a.u.).

6. MAIN RESULTS

Our experimental results have initiated new theoretical developments that have been worked out in the group or/and in collaboration of J. Burgdörfer and collaborators. One of our major contributions to the topics treated here is to have been able to confront theoretical approaches with experimental data in an absolute scale. Great cares have been taken to extract absolute experimental cross sections. In parallel, in the theoretical developments, efforts have been made to include all the ingredients so as to treat the complete dynamics of the interactions. Finally, we have attained a successful description of the ion transport in matter in the high velocity regime. We were even able to distinguish and quantify the role of the competing processes: the Stark mixing induced by the wake field that populates states coherently and that dominates at short ion transit times while the collisional mixing induces mainly decoherence (see §6.1) and becomes important at long ion transit times. For the laser-cluster interaction, by applying concepts issued from the collision domain, we have developed the first model that is able to provide absolute X-ray yields. The good agreement with the experiment (see §6.2) has allowed us identifying the heating mechanisms responsible for the X-ray emission even for unexpected low laser intensities.

In the following, I present first the main results obtained for the ion-solid interaction. I start by the Rydberg state production followed by the study of the evolution of the inner-np state populations and I end up with the behavior of the $n\ell j$ fine structure components. We'll see that this progress goes with an increase of the sensitivity to the dynamical mixing, i.e., the Stark mixing. In the last paragraph, I highlight results in the context of the laser-cluster interaction obtained with short laser pulse durations and argon clusters dedicated to the evolution of the X-ray yield with the laser intensity.

6.1 ION-SOLID INTERACTION

6.1.1 *RYDBERG STATE PRODUCTION*

A complete experimental study of the production and transport of Rydberg excited states has been done for Ar^{18+} on solid carbon targets, at a velocity of 23 a.u., and for a range of thicknesses allowing us to vary the transport conditions from single collision to equilibrium (3.5 to 201 μg/cm^2). In this case, the number of collisions the projectile electron suffers in the solid is extensively varied from ~ 0.6 to 60 collisions in average. I want to start by pointing out the cascade contribution on the different np states presented in Table 6-1 and estimated through the simulations based on the classical transport theory (CTT): the 2p state has the largest cascade contribution from upper levels that decay behind the target probing the production of Rydberg states with high angular momentum (such levels decay preferentially via the Yrast cascade, namely transitions from $n, \ell = n - 1$ to $n' = n - 1, \ell' = \ell - 1$).

	3.5 μg/cm^2 target		98 μg/cm^2 target	
np state	% direct	% cascade	% direct	% cascade
2p	60	40	51	49
3p	89	11	86	14
4p	≈ 100		99	1

Table 6-1: Respective contribution of direct and cascade population to the total population for different np states and two target thicknesses. The direct contribution corresponds to the population at the exit of the foil. The cascade contribution corresponds to the population coming from upper levels by radiative decay behind the foil.

In Figure 6.1 are plotted the normalized evolutions of the delayed Lyman line emission as a function of the distance behind the target (*D*). It clearly shows that the cascade contribution decreases when the principal quantum number n increases, as expected from Table 6-1, and the fewer cascades contribute to the np-state population, the faster the decay. Indeed, the decay slope for the np → 1s transitions with $n > 3$, for which no deviation from a binary ion-atom collision is observed, is greater than the ones for the two other transitions (with $n = 2$ and 3). Regarding the 2p slope dependence on target thickness, departure of the experimental data from a binary ion-atom collision proves its significant sensitivity to transport effects. Additionally, we have observed that a stationary regime is reached quite rapidly at approximately 20 μg/cm^2. In other words, equilibrium in high-ℓ Rydberg state population is established quickly, after typically six collisions, i.e., an ion transit time in the solid of 2 fs ([27]). The decay slopes predicted by the CTT are in very good agreement with the experimental data (blue and red lines in Figure 6.1).

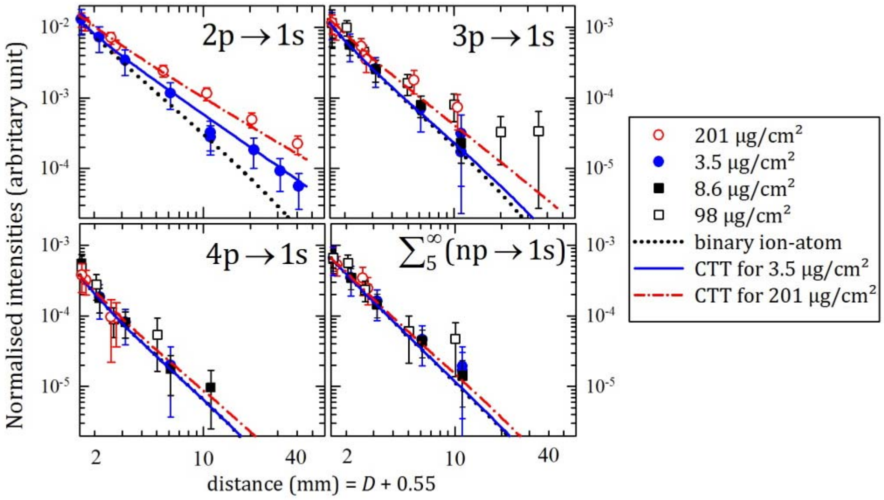

Figure 6.1: Normalized evolution of the delayed Lyman line emission as a function of the distance behind the target [74]. Symbols are the experimental data. Blue and red curves are the predictions of the classical transport theory (CTT) with wake off for the targets of 3.5 μg/cm^2 and 201 μg/cm^2. Binary ion-atom conditions, i.e., including cascade contribution without any transport effects, are also plotted. The distance behind the target has been arbitrarily shifted by 0.55 mm for sake of clarity.

We have also demonstrated that the experimental delayed Lyman intensities are, in fact, sensitive to all the excited states up to $n = 30$ even if only 3% of excited states have a principal quantum number $n > 10$ ([78] and [89]). A more rigorous comparison between the simulations and the experimental data is achieved when the absolute photon intensities are examined. In Figure 6.2 and Figure 6.3, we present the number of photons per ion as a function of the ion time of flight behind the target (named also the delay time) for the thinner and thicker targets (a series of results for the other target thicknesses are given in [74]). In each figure, the experimental data are compared with the rate-equation model and the classical simulation (CTT) with or without the wake field included, respectively, “wake on” and “wake off” (§5.1.1). Note that for delay times < 9 ps, the evolution of the experimental data is mostly governed by geometrical effects while the intensity is sensitive to the X-ray auto-absorption. For the rate equation approach (§5.2.1), I remind that only nℓ states up to $n = 10$ are accounted for. Hence, in order to overcome this intrinsic limitation, we assume a n^{-3} law ([25]) for states with $n > 10$ for the initial capture process. At a first stage, one can see that the three different types of *ab initio* calculation reproduce very well the observed behaviors. For the rate equation model, as expected, the inter- and intra-shell collisional excitation (and ionization) processes not included for $n > 10$ are missing for the thicker targets (for the inter-shell excitation the cross sections with $\Delta n > \pm 1$ become even as high as those with $\Delta n = \pm 1$ for levels of high n value). Finally, comparisons with theory demonstrate that the evolution of the population of these highly excited states during the transport is mostly governed by multiple scattering (i.e., multiple collisions). Indeed, the classical simulation with or without the wake field does not exhibit large differences. Regarding the curve behavior, the slight differences for the thicker targets (see the delayed Lyman α in Figure 6.3) between both simulations are too small to be conclusive in spite of good statistics, at least for the present collision system.

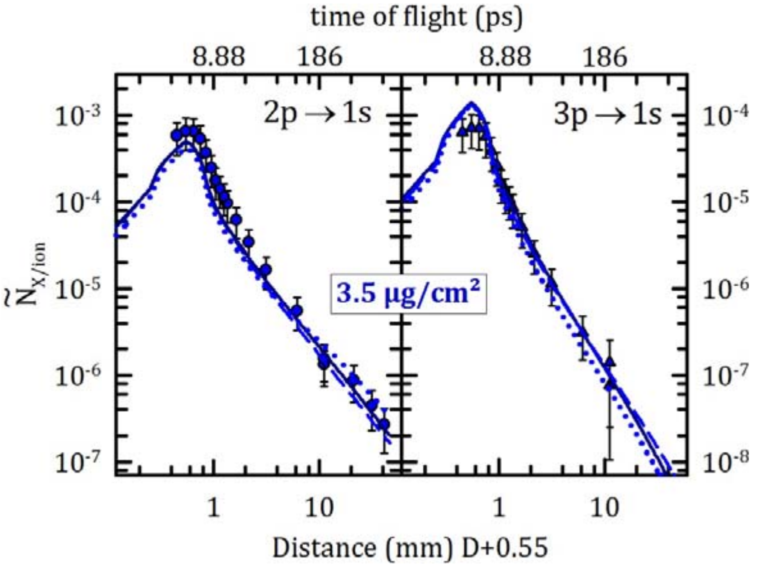

Figure 6.2: Evolution with the ion time of flight behind the target of the Ar^{17+} Lyman line intensities, i.e., number of emitted photons per ion, for the 3.5 µg/cm2 carbon target. Experimental results: symbols, CTT simulations with wake off (dashed lines) and wake on (solid lines), rate-equation model (dotted lines). In the simulations, the CDW calculations have been used to account for the primary capture processes. The distance behind the target has been arbitrarily shifted by 0.55 mm for sake of clarity.

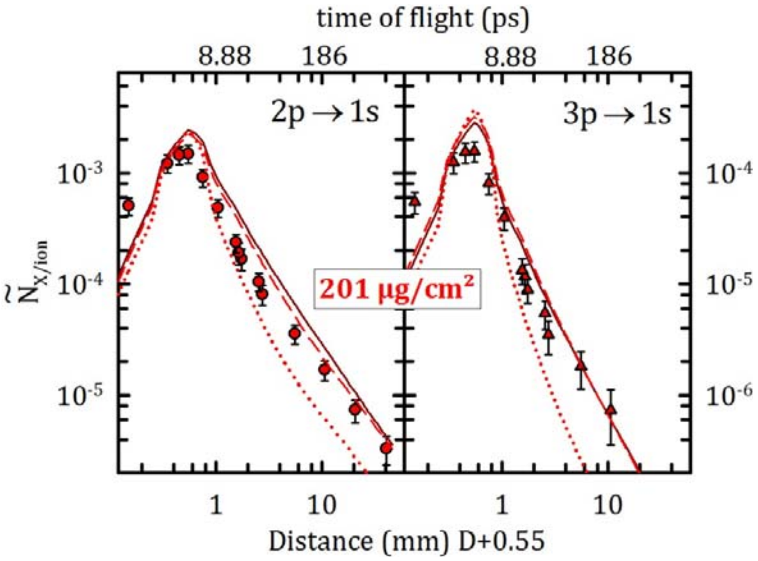

Figure 6.3: Same as Figure 6.2 for the thicker target (201 µg/cm²)

6.1.2 POPULATIONS OF INNER STATES

The absolute Lyman lines (or populations) at different target thicknesses are shown in Figure 6.4 where comparisons with the master equation approach (MEA, §5.2.1) taking into account or not the effect of the wake field are exhibited. As previously, the binary ion-atom collisions excluding any transport effects are also plotted. As expected, the role of transport effects becomes more and more important when the n quantum number increases. This sensitivity starts at n = 3 in the case of krypton while it is very pronounced already for the 2p state for argon. The multiple collisions represent the dominant source of transport effects. The sensitivity to the wake field increases as well with n and starts to play a role from n = 4 for krypton and n = 2 for argon. For krypton the energy splitting in n = 2 are too large for an efficient Stark mixing while this mixing is compensated in n = 3 when looking at the total population in 3p (see §2.1.3). For argon, the energy splitting are much smaller resulting in a higher sensitivity to the wake field. Moreover, I remind that the dynamical coupling element is inversely proportional to the square of the collision velocity (Eq. 8 and Eq. 9 in §2.1.3) making the collision system argon at 23 a.u. on carbon more sensitive to the wake field than krypton at 47 a.u.. The MEA calculations with "wake on" are then in better agreement with the experimental data. In the following, only calculations taking into account the effect of the wake field are shown.

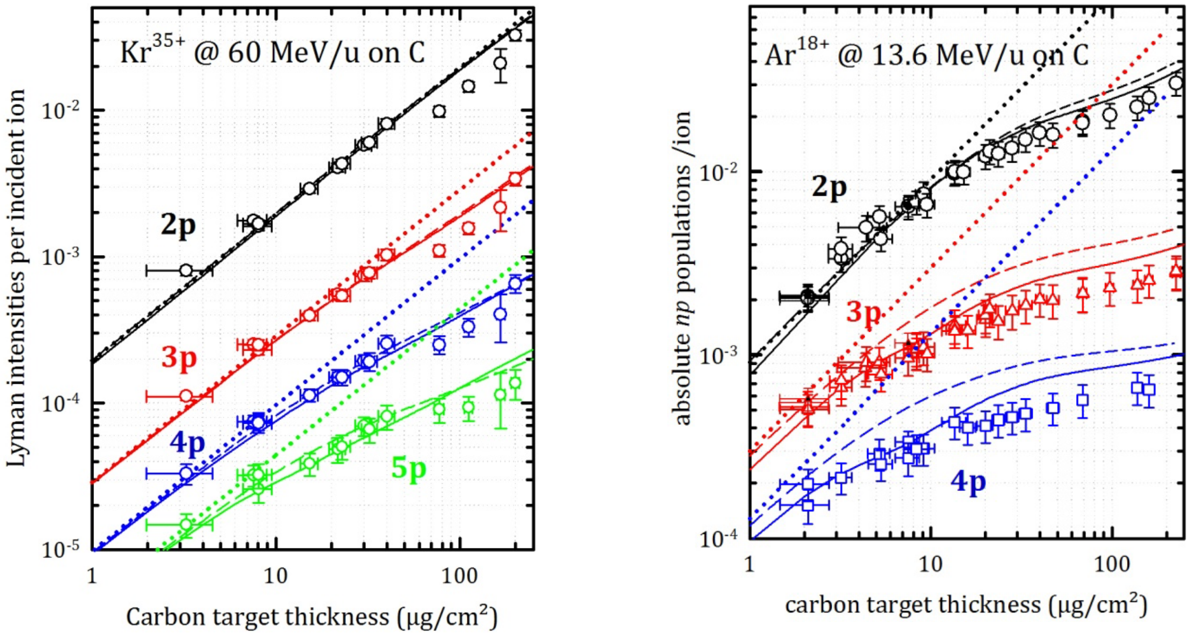

(a) ***(b)***

Figure 6.4: Absolute Lyman intensities (or populations) as a function of carbon target thickness. The full and dashed lines correspond to the predictions of the master equations approach (MEA) with "wake on" and "wake off" respectively. The dotted lines account for binary ion-atom collisions (i.e., without any transport effects). ***(a)*** *Lyman lines emitted by Kr^{35+} at 14 a.u. - [28]- (in this case PWBA calculations are used for the initial conditions of populations, i.e., the 1s → nℓ excitation process).* ***(b)*** *Lyman lines emitted by Ar^{17+} at 23 a.u. -partially in [39] and [89]- (in this case CDW calculations are used for the initial conditions of populations, i.e., the capture process).*

The dependence of these experimental populations on the initial density matrix has also been examined. In the case of the single 1s → nℓ excitation process for krypton, the two calculations (§1.1.3), PWBA (plane wave Born approximation) and CC (close coupling predictions), predicting nℓ cross sections rather similar, are in good agreement with these experimental data. For the capture process acting as the primary process, three approaches discussed in §1.1.3, namely CTMC (classical trajectory Monte Carlo), CDW (continuum distorted wave) and LTDSE (lattice time-dependent Schrödinger equation) predict different initial electron capture density matrices (I remind that CDW and LTDSE give results not so different). In Figure 6.5, I present the results issued from the Monte Carlo quantum transport theory (QTT, §5.2.2) when those three calculations are used as the source term. Transport simulations using CDW and LTDSE agree well with the experimental populations (2s and np with n = 2, 3 et 4) in the entire range of interaction times. Since CTMC cross sections for capture into p states are higher than those obtained with LTDSE or CDW, populations calculated using CTMC are larger than the present measurements. In contrast, results using CTMC are within the experimental uncertainty for the 2s intensity in the single collision regime (i.e., for thin carbon foils) but the discrepancy increases during transport as the 2s state mixes with other states, and especially with the 2p state.

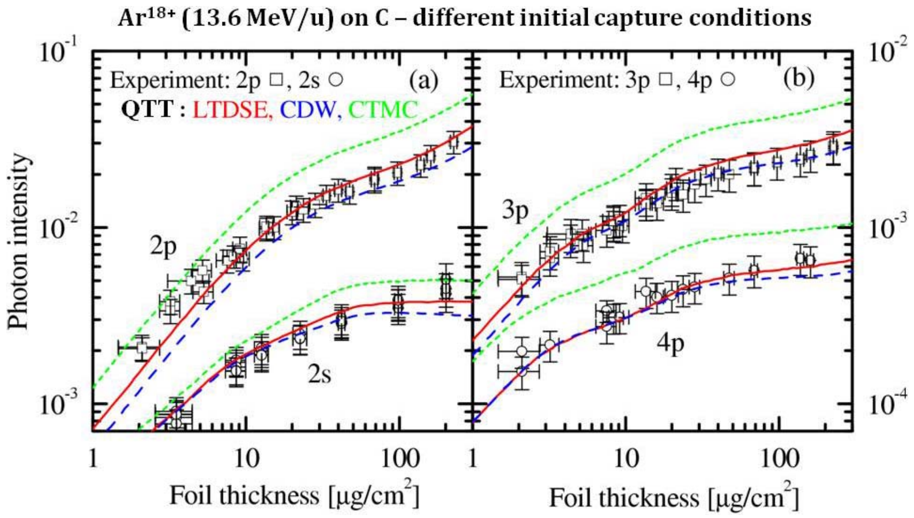

Figure 6.5: Absolute number of photons per ion $N_{np,2s}$ of excited Ar^{17+} ions as a function of the carbon foil thickness for (a) n = 2 sub-levels and (b) np with = 3, 4. Symbols: experimental data; lines: results from full simulation (i.e., with "wake on") within the QTT method using different capture density matrices as input: solid red lines for LTDSE; dashed blue lines for CDW; short dashed green lines for CTMC (§1.1.3).

In the case of the collision system Ar^{18+} (13.6 MeV/u, i.e., 23 a.u.) on carbon, we can compare the three approaches we have developed to describe the ion transport, namely, QTT, MEA and CTT as shown in Figure 6.6. For the two quantum approaches, QTT and MEA, the same initial conditions are used and they give comparable results for thin carbon foils below ~ 10 μg/cm^2. For larger thicknesses, the MEA calculations overestimate the np populations. This discrepancy is probably due to the damping of coherences through collisions that is not explicitly taken into account in the MEA predictions (see discussion of the Eq. 33 §5.2.1). The CTT approach gives rather reasonable evolutions ([79]) and the differences with respect to the quantum methods are not dramatic for the nℓ sub-level populations discussed here. The largest ones are observed for increasing foil thickness for the 2s, 3p, and 4p intensities. These differences are mainly due to the fact that the CTT simulations neglect (i) coherences in the electron capture source and (ii) the radiative decay while ion is inside the solid.

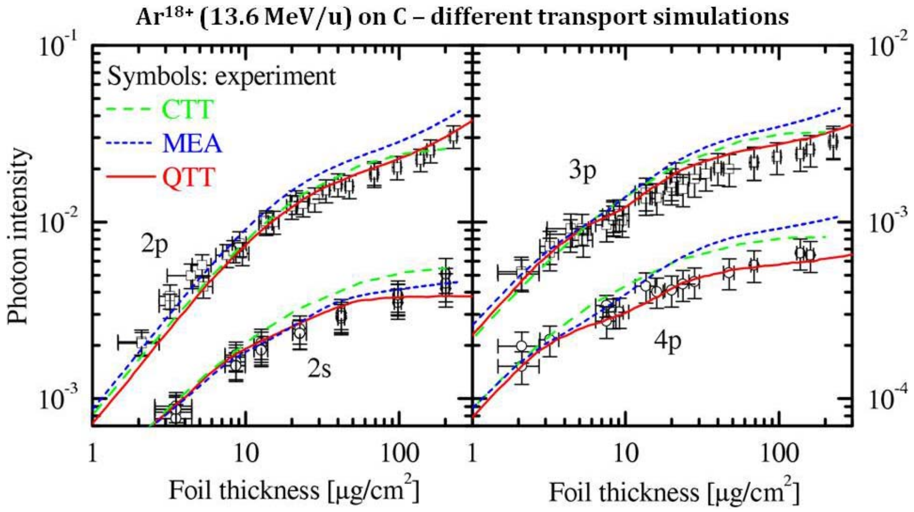

Figure 6.6: Absolute number of photons per ion $N_{np,2s}$ of excited Ar^{17+} ions as a function of the carbon foil thickness for (a) n = 2 sub-levels and (b) np with = 3, 4. Symbols: experimental results. Lines: results of three different transport calculations namely CTT (§5.1.1), MEA (§5.2.1) and QTT (§5.2.2). Initial capture density matrix: predictions from LTDSE for MEA and QTT and from CDW for CTT.

6.1.3 FINE STRUCTURE COMPONENTS: STUDY OF RATIOS

The evolution of the fine structure components, i.e., the nℓj states, directly sensitive to the Stark mixing and consequently to the coherence terms of the density matrix offers the opportunity to test our transport models with unprecedented accuracy (the y-axis of our plots is linear in this sub-section).

In the case of Ar^{18+} (13.6 MeV/u) on carbon, we have experimentally access to the ratio of Ar^{17+} Lyman intensities $I(2\mathrm{p}_{1/2}\to 1\mathrm{s}_{1/2})/I(2\mathrm{p}_{3/2}\to 1\mathrm{s}_{1/2})$ named $2\mathrm{p}_{1/2}$ / $2\mathrm{p}_{3/2}$. For the primary process of charge transfer, the non relativistic calculations used in this manuscript include only spin-independent interactions. As a result, the nℓj populations ($P(\mathrm{n}\ell\mathrm{j})$) are linked to the n$\ell$ populations ($P(\mathrm{n}\ell)$) through statistical factors:

Eq. 38
$$P(n\ell j) = \frac{1}{2}\,\frac{2j+1}{2\ell+1}\,P(n\ell)$$

For n = 2, Eq. 38 yields a ratio $P(2\mathrm{p}_{1/2})/P(2\mathrm{p}_{3/2})$ = 0.5. Since upper excited states are also statistically populated and by taking into account branching ratios, we note that cascade feeding does not bring any change of this value when focusing on the intensity ratio. Therefore, for the very thin foils, the $2\mathrm{p}_{1/2}$ / $2\mathrm{p}_{3/2}$ ratio must reach a value close to 0.5. When increasing the foil thickness, deviations from this value occur due to transport effects. Figure 6.7(a) displays the results of the experiment and of full simulations (including all the transport effects) based on the QTT approach for three different initial capture density matrixes. When comparing these full simulations with simulations with no coherence (green line), we underline the major role of the wake field or more precisely the interplay between the wake field and the relativistic splitting of the energy level for this collision system. Otherwise, as expected, all of the full simulations tend toward a value close to 0.5 in the single collision limit but lead to different results after a transit time for the ion of ~ 0.3 fs corresponding to ~ 3 μg/cm^2. Nevertheless, none of them give results in agreement with the experiment and this from the first μg/cm^2 of the solid target.

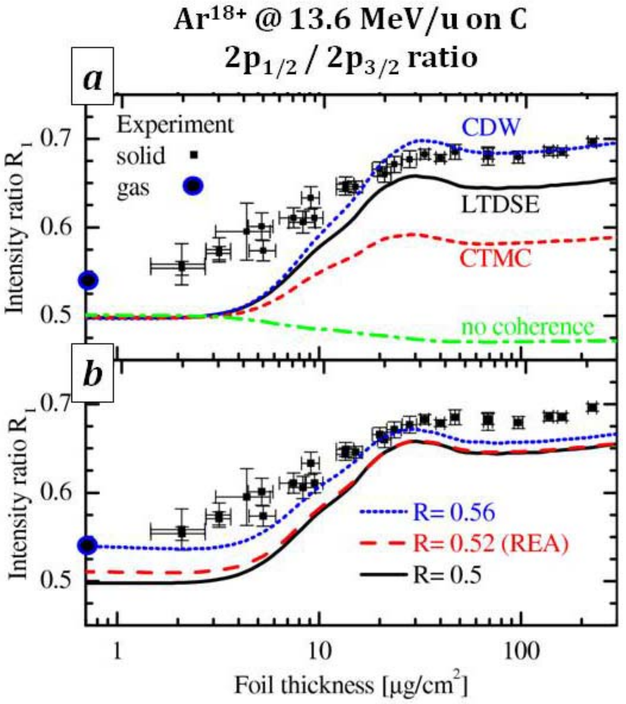

Figure 6.7: Lyman α photon intensity ratio between $2p_{1/2}\to 1s$ and $2p_{3/2}\to 1s$ following transport of Ar^{17+} ions (initially Ar^{18+}) through carbon foils as a function of foil thickness [90]. Symbols are the experiment data with solid and gaseous (CH_4 or N_2) targets. Lines are the QTT results: (a) calculations with different capture density matrices as source (CDW, LTDSE and CTMC) and one neglecting the wake field (equivalent to neglecting coherences); (b) calculations using LTDSE but with adjusted ratios $R = \sigma_{2p1/2}/\sigma_{2p3/2}$ *(see text).*

In order to identify the experimental single collision limit, we have measured the $2p_{1/2}$ / $2p_{3/2}$ ratio using gaseous targets. Whatever the gas (CH_4 or N_2), we have found a value of 0.54 ± 0.01, ∼ 10% larger than expected. To estimate whether relativistic effects are present during the primary capture process, we have used the relativistic eikonal approximation (REA) to evaluate the ratio $R = \sigma_{2p1/2}/\sigma_{2p3/2}$ where σ are cross sections [90]. The REA predicts a ratio R = 0.52 different from 0.5 giving a hint that additional relativistic effects could be present. This ratio is nevertheless still insufficient to account for the data (see Figure 6.7(b)). To have a better agreement for the thinner foils, a shift to a value of 0.56 is necessary. Relativistic calculations of the one-electron capture density matrix at moderately relativistic velocities are missing to bring a final conclusion, the unprecedented accuracy for this type of measurement requiring these new calculations.

In the case of krypton, we have studied the $3p_{1/2}$ / $3s_{1/2}$ and $3d_{3/2}$ / $3d_{5/2}$ population ratios (details of data analysis can be found in [31] and [29]). This collision system is very interesting in a sense that, in this case, the initial density matrix evaluated with PWBA calculations is well known. Hence, we test only the transport phase of our various theoretical approaches. Figure 6.8 represents the evolution of the relative $3p_{1/2}$ / $3s_{1/2}$ line intensity as a function of the krypton ion propagation length. Comparisons with transport simulations (QTT for Figure 6.8) demonstrate that good agreement with experiment can be achieved, only when radiative and collisional processes together with the wake effect are taken into account on an equal footing. Unlike the case of argon but as expected, the radiative decay inside the solid is far to be negligible and plays an important role (the radiative lifetime being proportional to Z_p^{-4}): if no radiative decay is accounted for, the $3p_{1/2}$ / $3s_{1/2}$ ratio decreases from an ion propagation length around 5000 a.u. while it strongly increases experimentally. This propagation length is close to the radiative propagation length of the 3p state (τ_r (3p)∼ 130 a.u. - see Table 2-2 – corresponding to a length of ∼ 6000 a.u.).

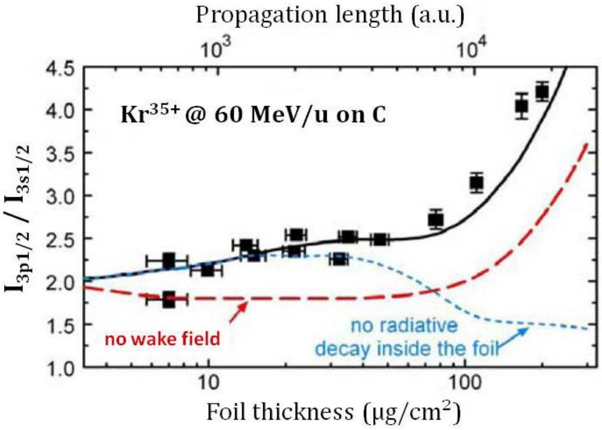

Figure 6.8: Relative line emission intensities from the $3s_{1/2}$ and $3p_{1/2}$ states for Kr^{35+} ions populated initially by the single excitation process as a function of the foil thickness. Experimental data are given by symbols with error bars; solid black line for the full QTT simulations, dashed red line for QTT with wake off, short dashed blue line for QTT with no radiative decay inside the foil ([88] and [91]).

In Figure 6.9, the evolution of the experimental $3d_{3/2}/3d_{5/2}$ ratio is plotted as well and I compared the experimental results with our two quantum transport simulations (MEA and QTT) that give similar tendencies. With this figure, we better appreciate the sensitivity of the collisional effects on one hand and of the effect of the wake field on the other hand (the x-axis is linear compared to Figure 6.8). For the $3p_{1/2}$ / $3s_{1/2}$ ratio, simulations with "wake off" (i.e., pure collisional approaches) predict first a decrease up to ∼ 25 μg/cm^2 in clear contradiction with the observed increase very well reproduced by the complete calculations that take into account the Stark coupling. This demonstrates that we control the contribution of the wake field on the hydrogen-like excited states. For larger thicknesses, the role of the collisional processes becomes more significant. For the $3d_{3/2}/3d_{5/2}$ ratio that implies two states of the same nℓ shell, as expected, collisional approaches predict no evolution with the ion transit time. Taking into account the Stark mixing gives a good estimation of the asymptotic value. The ratio is slightly over estimated for intermediate thicknesses (~ 50-100 μg/cm^2) but the disagreement is found to be around 10% at maximum.

Comparisons between the experiment and the models are rather satisfying keeping in mind all the ingredients included (especially, cross sections, coherences and wake field intensity) in the simulations and that there is no adjustable parameter.

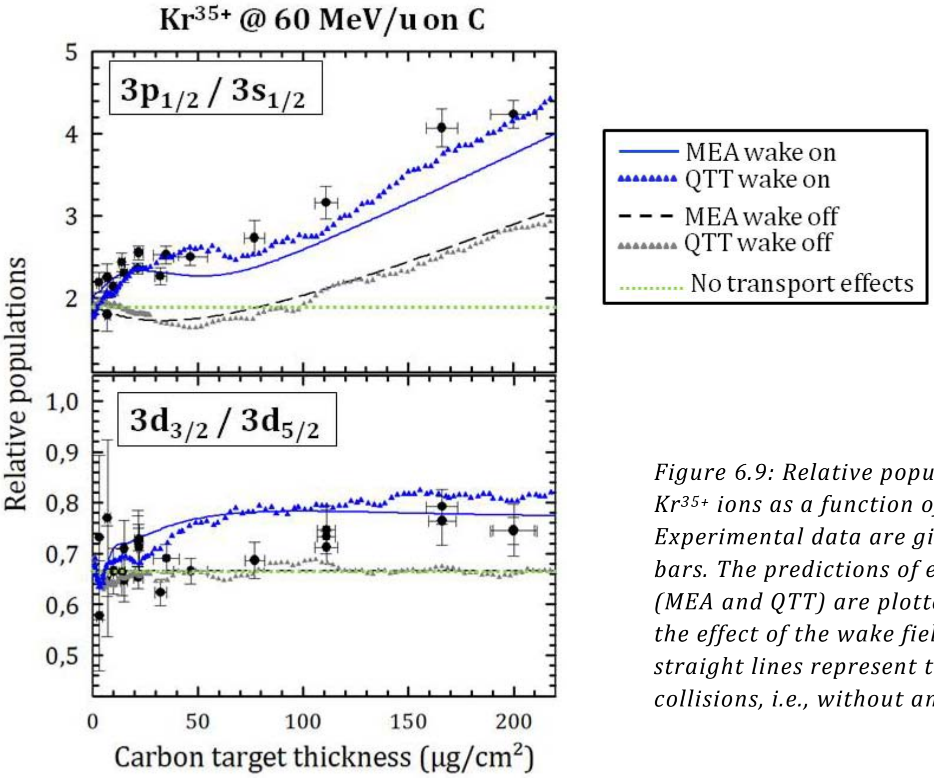

Figure 6.9: Relative population ratios in n = 3 for Kr^{35+} ions as a function of the foil thickness. Experimental data are given by symbols with error bars. The predictions of each quantum approaches (MEA and QTT) are plotted only with and without the effect of the wake field. The green dashed straight lines represent the binary ion-atom collisions, i.e., without any transport effects.

6.2 LASER-CLUSTER INTERACTION: ABSOLUTE X-RAY YIELD VERSUS LASER INTENSITY

During the last decade, we have performed many experimental campaigns dedicated to the study of the X-ray emission occurring during the interaction of intense laser pulses with rare gas clusters. The influence of many physical parameters has been carefully examined as the laser intensity (with $10^{14} \leq I_{peak} \leq 10^{17}$ W/cm^2), the pulse duration (at fixed laser energy with durations from 50 fs to 1 ps), the laser polarization and the cluster size. Results are presented in details in [55] and [62]. More recently, we have performed experiments by changing the laser wavelength from 800 nm to 400 nm [56].

As already mentioned, I restrict this paragraph only to the evolution of the X-ray yield as a function of the laser intensity with a laser wavelength of 800 nm.

6.2.1 EVOLUTION AS THE EFFECTIVE FOCAL VOLUME

One of the goals of the work performed by Prigent [55] was to examine more carefully the evolution of the X-ray yield as a function of the laser intensity so as to determine the laser intensity threshold for the X-ray emission. A typical evolution of the absolute number of keV photons per laser shot in 4π (N_X) with the laser intensity is shown in Figure 6.10. The data are obtained by tuning only the laser energy keeping the pulse duration constant. As expected and already discussed in §1.2.2: i) N_X is found to follow the power law $I_{peak}^{3/2}$ at high intensities (dashed blue line in Figure 6.10) indicating that a saturation regime is reached and ii) a clear intensity threshold I_{th} is observed. More precisely, what has been found is the clear identification and determination of the intensity threshold which requires measuring the X-ray yield over more than four orders of magnitude. This behavior is in agreement with the evolution of the effective focal volume averaged over the pulse duration (red line in Figure 6.10). Indeed, above the threshold, N_X simply grows with the number of heated clusters inside this volume noted $V_{eff.foc}$ once the laser intensity I_{peak} is greater than I_{th}. It is worthwhile to mention that whatever the cluster size and nature (xenon or krypton), the laser wavelength and the pulse duration ([56] [62] [71] [92]), we found always:

Eq. 39
$$N_X \propto V_{eff.foc}(I_{peak}/I_{th})$$

Hence, only the determination of I_{th} fixes the number of clusters emitting the X-rays. At τ = 55 fs, λ = 800 nm and cluster size of 3. 10^5 at/cl, the experimental intensity threshold for the production of characteristic K X-rays lies at a laser intensity as low as I_{th} = 2.2 10^{15} W/cm^2. By comparison, the ponderomotive energy of a free electron in an oscillating laser field of this intensity is U_p = 130 eV, more than an order of magnitude below the binding energy of the K-shell electrons (see Table 2-6 in §2.2.2). As a consequence, additional heating mechanisms very efficient have to be considered. The main question raised was then: are the heating mechanisms emphasized through the electrons dynamics presented in §5.1.2 efficient enough to correctly predict N_X?

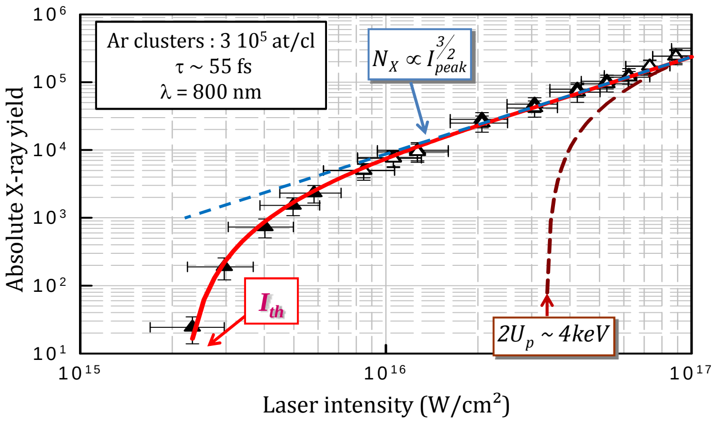

Figure 6.10: Evolution of the absolute 3.1 keV X-ray yield with the laser intensity for a fixed pulse duration of 55 fs. Blue dashed line represents the power law $I_{peak}^{3/2}$; brown dashed line is the expected behavior when considering $2U_p$ required to accelerate electrons up to an energy greater than the binding energy of a K-shell electron in argon; red solid line is the evolution of $V_{eff.foc}$; I_{th} marks the experimental laser intensity threshold.

6.2.2 COMPARISON WITH THE SIMULATIONS

The approach briefly described in §5.1.2 consists in treating the dynamics of a *single* large cluster to extract the K-shell ionization probability per cluster ($P_{K/cluster}$). The laser intensity threshold I_{th} is then determined allowing the evaluation of the effective focal volume $V_{eff.foc}$. The absolute X-ray yield N_X is then given by:

Eq. 40
$$N_X \propto \int_{I_{th}}^{I_{peak}} P_{K/cluster}(I) \times V_{eff.foc}(I/I_{th})\, dI$$

In Figure 6.11, a comparison with the experiment is shown for three different short pulse durations (in [62] and [56], the influence of the pulse duration on the laser intensity threshold has been precisely examined). For pulse durations of 55 and 140 fs, the agreement with the experiment is very satisfying: the evolution over several orders of magnitude is well reproduced and the predictions of the I_{th} values are very good (keeping in mind that there is no adjustable parameter in the theory [56]). As a result, we can consider that within the new approach we have developed, the heating mechanisms are well identified: strongly enhanced electric fields formed at the cluster poles by the combined action of cluster charging and polarization allow a fraction of electrons to be accelerated through back the cluster up to energies in the keV range. Electrons initially produced at rest by optical field ionization gain then enough energy to produce, in return, K-shell vacancies by electron impact ionization and, this, even at low laser intensity.

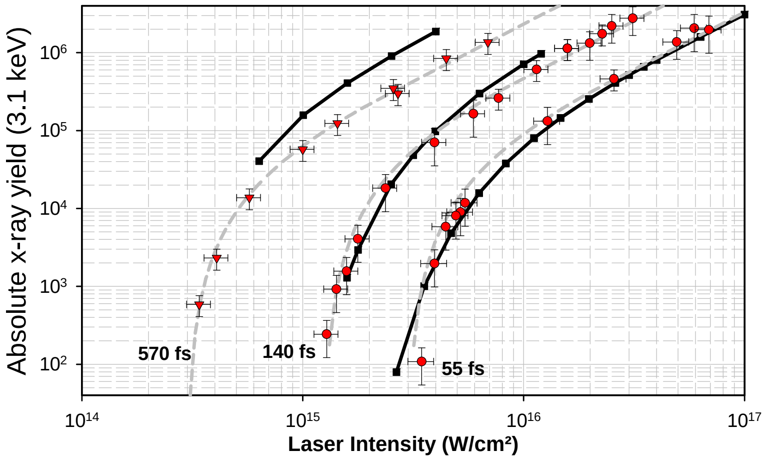

Figure 6.11: X-ray yield from argon clusters (~ 4 10^4 at/cl) as a function of laser peak intensity at 800 nm for three different pulse durations 55 fs, 140 fs and 570 fs. Gray dashed lines correspond to the fitted effective focal volume and full lines with squares to the simulation data.

For the longer pulse τ = 570 fs, the model overestimates the absolute X-ray yields by approximately a factor 3 but, nevertheless, reproduces the intensity dependence. This comparison underlines the role of the ion dynamics. Indeed, by increasing the laser pulse duration, the competition between electron heating mechanisms and the cluster expansion is revealed. A better description of the ionic motion has to be considered and, notably, the effective shielding of the repulsive ion-ion interaction driving the cluster expansion is not accurately represented by our approach. This point is under discussion with our colleagues from Vienna.

CONCLUSION

The use of X-ray spectroscopy has allowed us to probe the ultra-fast dynamics of both the ion-solid and laser-cluster interactions. In the case of the interaction of fast highly charged ions with solid, the X-ray emission is directly linked to the projectile excited state populations. The study of their evolution with the ion transit time inside the solid gives access to the response of the target electrons to the passage of the ion. The choice of collision partners (i.e., the projectile ion and the target whose thickness is varied) and of the collision velocity has allowed us to shed light on both features of the ion-solid interaction: the ***collisional aspect*** due to binary ion-atom processes (solid seen as an assembly of atoms) and the ***collective response*** via the wake field induced by the projectile. In this manuscript, I have presented two experiments performed at GANIL (Caen) sensitive to the production of high-ℓ Rydberg states as well as to the core $n\ell$ and $n\ell_j$ levels. In the case of the study of heated rare gas clusters by intense laser pulses, the generation of keV X-rays is due to the production of highly charged ions with inner shell vacancies. Since these vacancies are produced by electron-impact ionisation, X-ray spectroscopy provides insight into the ***electron dynamics*** and, more precisely, on the ***heating mechanisms*** which allow electrons to gain energies as high as the inner-shell binding energies. Hence, the characteristic X-ray production can be viewed as a thermometer for hot electrons inside the cluster. Our experiments, performed on the LUCA facility (CEA Saclay), has allowed us to measure the absolute X-ray yield evolution with various physical parameters as intensity, polarization, pulse duration and wavelength of the laser as well as the size of the clusters. The evolution with the laser intensity, presented in this manuscript, has brought out a laser intensity threshold in the X-ray production that is a key point to test the competing heating mechanisms.

The theoretical description of those two types of interactions has been a great challenge to treat on the same footing all the competing processes. We have opted for two stochastic approaches based on Monte Carlo calculations (the classical transport theory CTT and the quantum transport theory QTT) and for a master equation approach (MEA) that includes equations of rate-like type. The two quantum theories, namely QTT and MEA, have been developed exclusively in the context of the ion-solid interaction so as to describe the evolution of a small open system (the hydrogen-like projectile ion) in contact with a large reservoir (the solid). The MEA approach, built up in our group, consists of resolving master equations for the density matrix representing the small-system. MEA is an extension of Bloch equations. In QTT, developed in collaboration with J. Burgdörfer and co-workers, the density matrix is replaced by a wave function evolution governed by a non-linear stochastic Schrödinger equation. Those two approaches are well suited to the study of the evolution of coherences between states inside the solid. I must say that it is remarkable to realize that theoretical approaches first developed for dissipative processes in quantum optics implying a two- or three-level atom in interaction with an electromagnetic field may be generalized to a multi-level system in interaction with a reservoir including not only electromagnetic field but also collisions. For the classical Monte Carlo approach, CTT, the projectile ion trajectory is governed by the Langevin equation that takes into account the collisional processes through a stochastic force that I have evaluated for the collision system hydrogen-like argon ion at 23 a.u. on carbon foils. Such a simulation has no limitation in the number of states to be considered. Hence, it is well suited to the study of Rydberg state populations. To treat the dynamics of large clusters irradiated by intense laser pulses, we have employed a generalization of this classical simulation based on a mean-field approach in which a representative fraction of ions and electrons obeys the Langevin equation, the goal being to predict absolute X-ray yields.

The predictions of these various simulations are in good agreement with our absolute experimental measurements. The theory-experiment comparisons have allowed us to draw general conclusions. First, we have obtained a successful description of the ion transport in solid in the high velocity regime. A collisional picture of the interaction can be used to describe the high-ℓ Rydberg state populations and the major part of $n\ell$ core state populations (for those observables, it is worthwhile to mention that a classical transport gives similar results to those obtained with a quantum approach provided the radiative decay during the transport is negligible). Regarding in more details those $n\ell$ states and above all the $n\ell_j$ sub-state populations, we have shown that a pure collisional approach completely fails to reproduce their evolution inside the solid. It turns out that the dynamical mixing is very sensitive to initial conditions, i.e., the primary process as seen in the case of Ar^{17+} at 23 a.u. populated by capture in carbon, and to the effective wake field that mixes the sub-levels via the Stark effect. What is remarkable is that, when the initial conditions are well known as in the case of Kr^{35+} at 47 a.u. populated by the single excitation mechanism in carbon, the contribution of this electric field extracted from ion stopping power measurements is well controlled. Indeed, by inducing a Stark coupling, it explains the evolution of the fine structure components with the target thickness. In fact, our results can be considered as the first direct measurement of this wake field.

For the laser-cluster interaction, the absolute X-ray yield is found to be governed by the collision dynamics inside a single cluster and also by the variation of the effective focal volume. I remind that this volume is proportional to the number of clusters experiencing laser intensities that exceed the intensity threshold for x-ray production. Our Monte Carlo mean-field simulation predicts absolute X-ray yields in agreement with the experiment over more than four orders of magnitude and pulse duration shorter than 150 fs. This interaction leads to well identified electron heating mechanisms that turn out to be very efficient even at low laser intensities (< a few 10^{15} W/cm^2): the combined action of the cluster charging up and polarization gives rise to an enhanced electric field at the cluster poles that, in turn, allows a fraction of electrons be strongly accelerated through the cluster. For longer pulse durations (> 150 fs), the competition between electron heating mechanisms and ionic motion (i.e., the cluster expansion) becomes significant and a better description of the ion-ion interaction with ions shielded by slow electrons is necessary.

PERSPECTIVE: THE FISIC PROJECT

In the future, I will continue to be involved in the research topics of the group: the study of the interaction of slow highly charged ions with clusters and magnetic surfaces (experiments to be carried out at SIMPA[4] and/or ARIBE[5]) and the study of the X-ray emission induced when nano-sized clusters are submitted to intense femtosecond laser pulses so as to reveal the competition between heating mechanisms (electron motion) and the cluster explosion dynamics (ionic motion) (experiments at the LUCA facility with the help of the SPAM[6] laboratory or other light sources). In this section, I focus on the FISIC project for which I am the scientific coordinator. This project has been first selected by the Scientific Advisory Committee of GANIL to be one of the devices of the new SPIRAL2 accelerator[7]. Then, we have proposed to incorporate it in the S^3 room. Now, this project is part of the EQUIPEX S^3 (GANIL, CEA-Irfu, CNRS-IN2P3, UPMC & Université Paris-Sud)[8] and is also included as such in the Labex PLAS@PAR[9].

The study of fast ion–slow ion collisions (FISIC) is motivated by the fact that ion-ion collisions are strongly correlated to the ion energy transfer in various plasmas such as inertial confinement fusion plasmas or stellar and interstellar plasmas. Furthermore, the strongest effects on material modifications (including biological material) are detected at the maximum ion stopping power, when all the primary electronic processes (electron capture, loss and excitation) are at a maximum (see Figure 1.2 §1.1.1). This occurs in "the intermediate velocity regime." There, as already presented in §1.1.1, the cross sections of all the elementary processes are of the same order of magnitude, and none of the available theories is able to treat this complex issue. This circumstance gives rise to a paradoxical situation where, for this velocity regime, cross sections are very hard to predict, while knowledge of these cross sections is of critical importance. In fact, beyond a pure three-body case (a bare ion and a hydrogenic target), none of the present most sophisticated available theories is able to treat these three processes together on the same footing. Consequently, a strong demand for ion-ion collision experiments exists. Besides the possibility to reach the three-body problem as a benchmark, we can explore the role of additional electrons to quantify a series of effects:

- Closure and/or opening channels
- Influence of the screening and anti-screening effects via the role of the electron-electron interaction
- Coulomb interaction in entrance/exit channels also called the dynamical screening
- Role of multiple processes

To illustrate this latter point, I present in Figure 0.1 the evolution of the single excitation cross section with the target atomic number obtained when helium-like argon ions at 13.6 MeV/u collide with various targets from He to Xe allowing to investigate a range from the perturbative regime to the strong interaction regime. Multiple processes are also plotted showing that the contribution of the capture-ionization mechanism, for instance, can reach 54% of the single excitation process [69] and [93].

Existing limitations in the investigation of ion-ion collisions are due to the very low density of the available ion targets. Moreover, ion beams of selected charge state and of high quality in terms of optics and intensity are required.

---

[4] SIMPA : Source d'Ions Multichargés de Paris site Jussieu devenue plateforme de l'UPMC depuis 2009 : http://www.insp.jussieu.fr/La-source-d-ions-muticharges-de.html.

[5] ARIBE : Accélérateurs pour Recherches avec des Ions de Basses Energies Caen : http://cimap.ensicaen.fr/spip.php?article803.

[6] SPAM: Service des Photons, Atomes et Molécules du CEA Saclay. http://iramis.cea.fr/spam/.

[7] Système de production d'Ions Radioactifs en Ligne de 2ème génération : http://www.ganil-spiral2.eu/spiral2.

[8] Equipment of Excellence "Super Separator Spectrometer": http://irfu.cea.fr/Phocea/Vie_des_labos/Ast/ast_technique.php?id_ast=943.

[9] Laboratory of Excellence « Plasmas à Paris, au-delà des frontières » : http://plasapar.upmc.fr/.

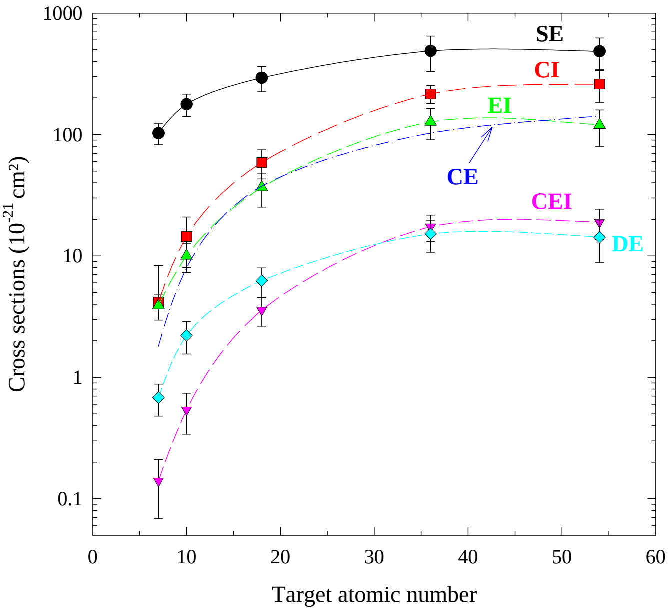

Figure 0.1: Evolution of the single excitation (SE) cross section and of multiple processes as capture ionization (CI), excitation-ionization (EI), capture excitation (CE), capture-excitation-ionization (CEI) and double excitation (DE) when Ar^{16+} at 13.6 MeV/u collide with gaseous targets.

So far, ion-ion collisions have been performed at Giessen University (Germany) or at Kansas State University (USA) but only in the case of slow ions (typically at center-of-mass energies of a few keV up to a few 100 keV) in the context of magnetically confined plasmas [94], [95], [96], [97] and[98]. Until recently, investigation of the intermediate velocity regime has been limited to the interaction of heavy ions in hydrogen or deuterium plasmas (see for instance [99]). It has been shown that ionization of the medium leads to strongly reduced capture cross sections, an increase of projectile charge state and a resultant increase in stopping power, but many charge states are present at the same time in "conventional" plasma mode of relatively light ions. It soon becomes very hard to extract precise information about changes in elementary processes based on an average of charge states in the plasma. Extension of such investigations to heavier ions are foreseen using high power lasers like PHELIX[10] or LULI 2000[11], which can be coupled respectively to the GSI ion beams or to energetic laser accelerated ions. Fully ionized carbon plasma, for example, has been crossed with heavy ion beams using PHELIX at GSI [100]. However, it is obviously increasingly difficult to produce fully ionized media and the former techniques are applicable only for particular targets (to get a dense plasma, a solid target prior to irradiation by a powerful laser is required). Finally, two key points need to be reached: the production of "clean" plasmas where the ionization state is known and the ability to work with a large variety of plasmas.

The development of ion sources with high performance and the construction of new generation accelerators as SPIRAL2 at GANIL provide new opportunities to perform ion-ion collisions in the intermediate regime which are of great interest in atomic and plasma physic research. We propose, with the FISIC project, an alternative and competitive method to the one foreseen at GSI. The installation of the complete proposed device fits in very well with the S^3 facility (a new instrument for fundamental research in nuclear and atomic physics), Figure 0.2. We intend to use crossed beams of high intensities for which the charge state of both the incoming projectile ions and the target ionized medium are under control. Ions from carbon to xenon, delivered by SPIRAL2 (the "high energy" beam), with energies ranging between 4 and 14 MeV/u, will collide with ions from helium to argon delivered by an ion source and its ion beam line (the "low energy" beam). For the high energy beam, with the S^3 facility we should be able to vary the projectile ion charge state by means of "strippers". We have started a collaboration with the Plasma Physics division of GSI to perform numerical simulations of heating of strippers under beam impact

---

[10] PHELIX: Petawatt High Energy Laser for Ion eXperiments at the GSI facility, Darmstadt (Germany) (https://www.gsi.de/forschung/pp/index_e.html).

[11] LULI 2000: High power laser system located at LULI laboratory Ecole Polytechnique : http://www.luli.polytechnique.fr/.

due to the large specific power deposition by the projectile ions in the material. Since the carbon or aluminum stripper must remain intact during the experimental campaign over a long period of time, we have shown that a wheel shaped stripper rotating at a rate of a few 1000 rpm is necessary [101] and [102]. After stripping, the line will be equipped with optical elements of new generation and cooled slits providing ion beams of selected charge state of high intensity with good optical qualities. With regard to the low energy beams, a SUPERNANOGAN ECR[12] source connected to a low energy line would enable delivery of beams with energies less than or equal to 20 qkeV, with sufficient intensities of the required charge state. More precisely, this complete part should provide ion bursts with a well controlled time structure and profile. Indeed, to extract absolute measurements, an accurate imaging of the beam profile and intensity is one of the key parameters. To combine high resolution profile measurements with the advantage of absolute current values, we consider using the new system recently developed by IEAP[13] at the University of Kiel. It consists of an array of multiple tiny Faraday cups easily movable to scan the complete ion beam area. We are establishing a new collaboration with the group of IEAP to make this device working under ultra-high vacuum and compatible with the GANIL acquisition system. We will take care, as well, of the conception, design and manufacture of the ultra-high vacuum collision chamber (a pressure of 10^{-11} mbar is mandatory) in which electrostatic deflectors, an inner zone at high voltage and an electrostatic detection system will be placed.

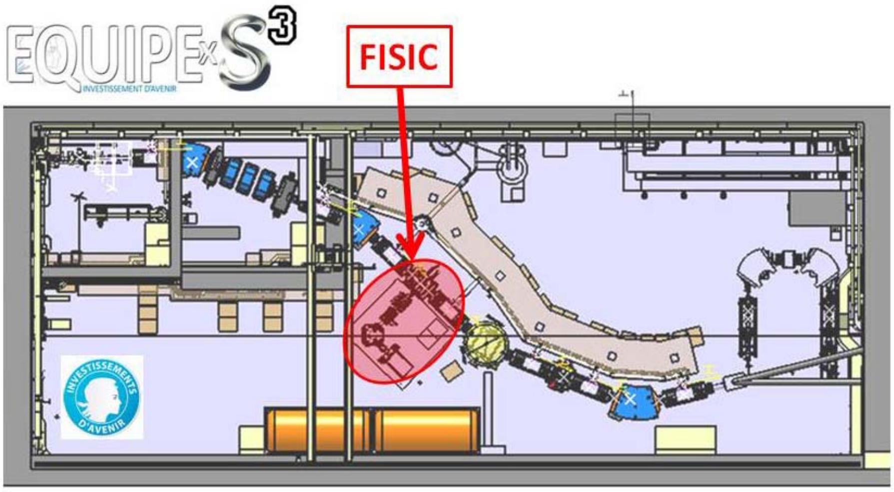

Figure 0.2: View of the S3 room with the location of the FISIC set-up.

From a theoretical point of view, the prediction of accurate cross sections in the energy regime under consideration requires non perturbative (close-coupling) treatments of the electronic dynamics. In a first step, with the group of A. Dubois from LCPMR[14], we suggest to extend our present models and computer codes (mostly dedicated to light ions collision systems) in order to deal with high velocity scattering as well as very large number of bound and positive energy pseudo-continuum states which can be populated during the process.

FISIC is an ambitious program to measure cross sections of elementary collisional processes, never attempted so far and to provide theoretical treatments available in the intermediate velocity regime. The experimental set-up and protocol have to be ready in 2016 according to the schedule of SPIRAL2. An international collaboration to make FISIC a success consists of : the "Centre de Recherche sur les ions, les Matériaux et la Photonique (CIMAP) and the GANIL (IN2P3) in Caen, the Irfu department at CEA Saclay, the Atomic Physics Division of GSI and Members of the Helmholtz Institute EMMI (ExtrEme Matter Institute), Darmstadt, Germany; The Atomic Physics

---

[12] ECR: Electron Cyclotron Resonance

[13] IEAP: Institute for Experimental and Applied Physics at Kiel University (Germany)

[14] Laboratoire de Chimie Physique Matière et Rayonnement (UPMC-CNRS), Equipe « Evolution temporelle de systèmes quantiques en champs intenses »

Group of KVI (Kernfysisch Versneller Instituut in Groningen (the Netherlands) and experts on ion beam detection of the University of Kiel (Germany) which should join soon the collaboration. The achievement of the whole scientific program should give rise to the establishment of a complete database together with theoretical interpretations.

REFERENCES

[1] H. Bethe, «Zur theorie des durchgangs schneller korpuskularstrahlen durch materie,» *Annalen der Physik,* vol. 5, p. 325, 1930.

[2] G. Olivera, A. Martinez, R. Rivarola et P. Fainstein, «Electron capture contribution to the stopping power of low-energy hydrogen beams passing through helium,» *Phys. Rev. A,* vol. 49, p. 603, 1994.

[3] G. Schiwietz, U. Wille, R. Díez Muiño, R. Fainstein et P. Grande, «Comprehensive analysis of the stopping power of antiprotons and negative muons in He and H2 gas targets,» *J. Phys. B,* vol. 29, p. 307, 1996.

[4] N. Bohr, «The penetration of atomic particles through matter,» *K. Dansk. Vidensk. Selsk. Mat. Fys. Medd.,* vol. 18, pp. 1-144, 1948.

[5] J. Neufeld et R. Ritchie, «Passage of charged particles through plasma,» *Phys. Rev.,* vol. 98, p. 1632, 1955.

[6] P. Echenique, F. Flores et R. Ritchie, Solid State Physics vol 43, New York Academic p 229: H Ehrenreich and D Turnbull , 1990.

[7] J. Fuhr, V. Ponce, F. Garcia de Abajo et P. Echenique, «Dynamic screening of fast ions moving in solids,» *Phys. Rev. B,* vol. 57, p. 9329, 1998.

[8] T. Ditmire, J. Tisch, E. Stringate, M. Mason, N. Hay, R. Smith, J. Marangos et M. Hutchinson, «High energy ion production in explosion of superheated atomic clusters,» *Nature,* vol. 386, p. 54, 1997.

[9] E. Springate, S. Aseyev, S. Zamith et J. Vrakking, «Electron kinetic energy measurements from laser irradiation of clusters,» *Phys. Rev. A,* vol. 68, p. 053201, 2003.

[10] K. Kondo, A. Borisov, C. Jordan, A. McPherson, W. Schroeder, K. Boyer et C. Rhodes, «Wavelength dependence of multiphoton-induced Xe(M) and Xe(L) emissions from Xe clusters,» *J. Phys. B,* vol. 30, p. 2707, 1997.

[11] S. Dobosz, M. Lezius, M. Schmidt, P. Meynadie, M. Perdrix, D. Normand, J. Rozet et D. Vernhet, «Absolute keV photon yields from ultrashort laser-field-induced hot nanoplasmas,» *Phys. Rev. A,* vol. 56, p. R2526, 1997.

[12] J. Rozet, M. Cornille, S. Dobosz, J. Dubau, J. Gauthier, S. Jacquemot, E. Lamour, M. Lezius, D. Normand, M. Schmidt et D. Vernhet, «State Selective Measurements of HCI Produced by Strong Ultrashort Laser-Clusters,» *Physica Scripta,* vol. T92, p. 113, 2001.

[13] M. Toulemonde, C. Dufour, A. Meftah et E. Paumier, «Transient thermal processes in heavy ion irrdiation of crystalline inorganicc insulators,» *Nucl. Instr. and Methods B,* Vols. %1 sur %2166-167, p. 903, 2000.

[14] H. Ryufuku, K. Sasaki et W. Tsutomu, «Oscillatory behavior of charge transfer cross sections as a function of the charge of projectiles in low-energy collisions,» *Phys. Rev. A,* vol. 21, p. 745, 1980.

[15] W. Fritsch et C. Lin, «Atomic-orbital-expansion studies of electron transfer in bare nucleus Z (Z=2, 4-8) hydrogen-atom collision,» *Phys. Rev. A,* vol. 26, p. 3039, 1984.

[16] T. Winter et C. Lin, «Triple-center treatment of electron transfer and excitation in p-H collisions,» *Phys. Rev. A,* vol. 29, n° %1567, 1984.

[17] F. Errea, J. Gomez-Llorente, M. Mendez et A. Riera, «Convergence study of He2++ H and He++ H+ charge exchange cross sections using a molecular approach with an optimised common translation factor,» *J. Phys. B,* vol. 20, p. 6089, 1987.

[18] M. Trassinelli, C. Prigent, E. Lamour, F. Mezdari, J. Mérot, R. Reuschl, J. Rozet, S. Steydli et D. Vernhet, «Investigation of slow collisions for (quasi)symmetric heavy systems: what can be extracted from high resolution x-ray spectra,» *J. Phys. B,* vol. 45, p. 085202, 2012.

[19] H. Betz, F. Bell, H. Panke, G. Kalkoffen, M. Welz et D. Evers, «New Technique for the Measurement of Lifetimes of Heavy-Ion Inner-Shell Vacancies,» *Phys. Rev. Lett,* vol. 33, p. 807, 1974.

[20] J. Rozet, A. Chetioui, P. Bouisset, D. Vernhet, K. Wohrer, A. Touati, C. Stephan et J. Grandin, «Anomalous population of deep capture states of fast ions emerging from solid foils,» *Phys. Rev. Letter,* vol. 58, p. 337, 1987.

[21] H. Betz, D. Röschenthaler et J. Rothermel, «Production of highly excited states of fast ions emerging from solid targets,» *Phys. Rev. Lett,* vol. 50, p. 34, 1983.

[22] R. Schramm, P. Koschar, H. Betz, M. Burkhard, J. Kemmler, O. Heil et K. Groeneveld, «Charge state dependence of convoy-electron yields in fast ion-foil interaction,» *J. Phys. B,* vol. 18, p. L507, 1985.

[23] J. Rozet, A. Chetioui, P. Piquemal, D. Vernhet, K. Wohrer, C. Stéphan et L. Tassan-Got, «Charge-state distributions of few-electron ions deduced from atomic cross sections,» *J. Phys. B,* vol. 22, p. 33, 1989.

[24] J. Rozet, C. Stephan et D. Vernhet, «ETACHA: a program for calculating charge states at GANIL energies,» *Nuclear Instruments and Methods in Physics Research B,* vol. 107, n° %167, 1996.

[25] P. Nicolaï, M. Chabot, J. Rozet, M. Politis, A. Chetioui, C. Stéphan, A. Touati, D. Vernhet et K. Wohrer, «Contribution of intrashell excitation to the l mixing of excited states of one electron ions in solids,» *J. Phys. B,* vol. 23, p. 3609, 1990.

[26] I. Despiney, Mélange cohérent et mélange collisionnel des états de structure fine d'ions lourds rapides en mileiux condensés, PhD Université Pierre et Marie Curie, 1994.

[27] E. Lamour, Production et transport des états excités du projectile en interaction ion-solide, PhD Université de Caen Basse Bormandie, 1997.

[28] D. Vernhet, C. Fourment, E. Lamour, J. Rozet, B. Gervais, L. Dubé, F. Martin, T. Minami, C. Reinhold, M. Seliger et J. Burgdorfer, «Transport of Kr35+ Inner-Shells Through Solid Carbon Foils,» *Physica Scripta,* vol. T92, p. 233, 2001.

[29] D. Vernhet, J.-P. Rozet, I. Bailly-Despiney, C. Stephan, A. Cassimi, J.-P. Grandin et L. Dubé, «Observation of dynamical substate mixing of fast ions in solids,» *Journal of Physics B: Atomic, Molecular and Optical Physics,* vol. 31, p. 117, 1998.

[30] J. Rozet, D. Vernhet, I. Bailly-Despiney, C. Fourment et L. Dubé, «Dynamical substate mixing of fast ions in solids: a density matrix approach,» *J. Phys. B: At. Mol. Opt. Phys.,* vol. 32, p. 4677, 1999.

[31] C. Fourment, Transport d'ions hydrogénoïdes rapides dans les solides: mise en évidence de l'écrantage dynamique, PhD Université Pierre et Marie Curie, 2000.

[32] M. Seliger, Open quantum system approach to transient coherence in ion-solid transport, PhD Thesis Technishe Universität Wien, 2005.

[33] W. Braithwaite, D. Matthews et C. Moore, «Delayed X-ray emission in the Lyman and Lyman-like series of one and two-electron oxygen,» *Phys. Rev. A,* vol. 11, p. 465, 1975.

[34] J. Kemmler, J. Burgdörfer et C. Reinhold, «Theory of the l-state population of Rydberg states formed in ion-solid interaction,» *Phys. Rev. A,* vol. 44, p. 2993, 1991.

[35] D. Crothers et L. Dubé, «Continuum distorted wave methods in ion-atom collisions,» *Adv. At. Mol. Opt. Phys.,* vol. 30, p. 287, 1992.

[36] H. Brandsen et M. McDowell, Charge exchange and the theory of ion-atom collisions, Oxford Science Publications, 1992.

[37] R. Olson, «n,l distributions in Aq+ on H electron-capture collisions,» *Phys. Rev. A,* vol. 24, p. 1726, 1981.

[38] T. Minami, C. Reinhold, D. Schultz et M. Pindzola, «Coherence parameters for charge transfer in collisions of protons with helium calculated using a hybrid numerical approach,» *Journal of Physics B,* vol. 37, p. 4025, 2004.

[39] M. Seliger, C. Reinhold, T. Minami, D. Schultz, M. Pindzola, S. Yoshida, J. Burgdörfer, E. Lamour, J. Rozet et D. Vernhet, «Electron capture and electron transport by fast ions penetrating solids: An open quantum system approach with sources and sinks,» *Phys. Rev. A,* vol. 75, p. 032714, 2007.

[40] D. Rule, «Total born-approximation cross sections for single-electron loss by atoms and ions colliding with atoms,» *Phys. Rev. A,* vol. 16, p. 19, 1977.

[41] R. Anholt, «Atomic collisions with relativistic heavy ions.II. Light-ion charge states,» *Phys. Rev. A,* vol. 31, p. 3579, 1985.

[42] F. Martin, «Excitation of atomic hydrogen by protons and multicharged ions,» *J. Phys. B,* vol. 32, p. 501, 1999.

[43] U. Saalmann, C. Siedschlag et J. Rost, «Mechanisms of cluster ionization in strong laser pulses,» *J. of Phys. B,* vol. 39, p. R39–R77, 2006.

[44] T. Fennel, K. Meiwes-Broer, J. Tiggesbäumker, P. Reinhard, P. Dinh et E. Suraud, «Laser-driven nonlinear cluster dynamics,» *Reviews of Modern Physics,* vol. 82, p. 1793, 2010.

[45] T. Ditmire, E. Springate, J. Tisch, Y. Shao, M. Mason, N. Hay, J. Marangos et M. Hutchinson, «Explosion of atomic clusters heated by high-intensity femtosecond laser pulses,» *Phys. Rev. A,* vol. 57, p. 369, 1998.

[46] M. Hirokane, S. Shimizu, M. Hashida, S. Okada, S. Okihara, F. Sato, T. Iida et S. Sakabe, «Energy distributions of ions emitted from argon clusters Coulomb-exploded by intense femtosecond laser pulses,» *Phys. Rev. A,* vol. 69, p. 063201, 2004.

[47] R. Rajeev, K. Rishad, T. Madhu Trivikram, V. Narayanan, T. Brabec et M. Krishnamurthy, «Decrypting the charge-resolved kinetic-energy spectrum in the Coulomb explosion of argon clusters,» *Phys. Rev. A,* vol. 85, p. 023201, 2012.

[48] L. Adoui, O. Gobert, P. Indelicato, E. Lamour, P. Meynadier, D. Normand, M. Perdrix, C. Prigent, J. Rozet et D. Vernhet, «Xe(L) X-ray emission from laser–cluster interaction,» *Nucl. Instr. and Methods in Physics Research*

B, vol. 205, p. 341, 2003.

[49] S. Dobosz, Interaction d'agrégats de gaz rare avec un champ laser intense, PhD Université Paris Sud, 1998.

[50] G. Junkel-Vives, J. Abdallah, F. Blasco, F. Dorchies, T. Caillaud, C. Bonte, C. Stenz, F. Salin, A. Faenov, A. Magunov, T. Pikuz et I. Skobelev, «Evidence of supercritical density in 45-fs-laser-irradiated Ar-cluster plasmas,» *Phys. Rev. A,* vol. 66, p. 033204 , 2002.

[51] A. Bar-Shalom, M. Klapisch et J. Oreg, «Electron collision excitations in complex spectra of ionized heavy atoms,» *Phys. Rev. A,* vol. 38, p. 1773, 1988.

[52] F. Dorchies, F. Blasco, C. Bonté, T. Caillaud, C. Fourment et O. Peyrusse, «Observation of Subpicosecond X-Ray Emission from Laser-Cluster Interaction,» *Phys. Rev. Lett,* vol. 100, p. 205002, 2008.

[53] T. Auguste, P. Monot, L. Lompré, G. Mainfray et C. Manus, «Multiply charged ions produced in noble gases by a 1 ps laser pulse at 1053 nm,» *J. Phys. B.,* vol. 25, p. 4181, 1992.

[54] S. Larochelle, A. Talebpour et S. Chin, «Non-sequential multiple ionization of rare gas atoms in a Ti:Sapphire laser field,» *J. Phys. B,* vol. 31, p. 1201, 1998.

[55] C. Prigent, L'émission X: un outil et une sonde pour l'interaction laser-agrégats, PhD Université Pierre et Marie Curie, 2004.

[56] C. Ramond, Probing the femtosecond dynamics of laser-cluster interaction via X-ray and electron spectroscopy, PhD Sorbonne Université - Université Pierre et Marie Curie, 2012.

[57] C. Rose-Petruck, K. Schafer, K. Wilson et C. Barty, «Ultrafast electron dynamics and inner-shell ionization in laser driven clusters,» *Phys. Rev. A,* vol. 55, p. 1182, 1997.

[58] C. Jungreuthmayer, M. Geissler, J. Zanghellini et T. Brabec, «Microscopic Analysis of Large-Cluster Explosion in Intense Laser Fields,» *Phys. Rev. Lett,* vol. 92, p. 133401, 2004.

[59] Y. Fukuda, Y. Kishimoto, T. Masaki et K. Yamakawa, «Structure and dynamics of cluster plasmas created by ultrashort intense laser fields,» *Phys. Rev. A,* vol. 73, p. 031201, 2006.

[60] Y. Fukuda, Y. Kishimoto, T. Masaki et K. Yamakawa, «Erratum: Structure and dynamics of cluster plasmas created by ultrashort intense laser fields,» *Phys. Rev. A,* vol. 81, p. 019904, 2010.

[61] C. Deiss, N. Rohringer, J. Burgdorfer, E. Lamour, C. Prigent, J. Rozet et D. Vernhet, «Laser-Cluster Interaction: X-Ray Production by Short Laser Pulses,» *Phys. Rev. Letter,* vol. 96, p. 013203, 2006.

[62] C. Prigent, C. Deiss, E. Lamour, J. Rozet, D. Vernhet et J. Burgdorfer, «Effect of pulse duration on the x-ray emission from Ar clusters in intense laser fields,» *Phys. Rev. A,* vol. 78, p. 053201, 2008.

[63] C. Deiss, Simulation of the dynamics of laser-cluster interaction, PhD Technischen Universitat Wien, 2009.

[64] H. Bethe et E. Salpeter, Quantum mechanics of one- and two-electron atoms, New York: Plenum/Rosetta Edition, Plenum Publishing Corporation, 1977.

[65] M. Ammosov et V. Krainov, «Tunnel ionization of complex atoms and of atomic ions in an alternating electromagnetic field,» *Sov. Phys JETP,* vol. 64, p. 1191, 1986.

[66] S. Augst, D. Meyerhofer, D. Strickland et S. Chint, «Laser ionization of noble gases by Coulomb-barrier supression,» *J. Opt. Sc. Am B,* vol. 8, p. 858, 1991.

[67] A. Mûller, E. Salzborn, R. Frodl, R. Becker, H. Klein et H. Winter, «Absolute ionisation cross sections for electrons incident on O+, Ne+, Xe+ and Ar i+ (i=1,...5),» *J. Phys. B,* vol. 13, p. 1877, 1980.

[68] M. Uddin, A. Haque, K. Karim et A. Basak, «Empirical model for the ionization cross sections of H- and He-like ions,» *Physica,* vol. 72, p. 389, 2005.

[69] L. Adoui, Mécanismes d'excitation d'ions Ar16+ en colission avec des cibles gazeuses à vitesse intermédiaire, PhD Université Pierre et Marie Curie, 1995.

[70] E. Lamour, C. Prigent, B. Eberhardt, J. Rozet et D. Vernhet, «2E1 Ar17+ decay and conventional radioactive sources to determine efficiency of semiconductor detectors,» *Rev. of Scient. Instr.,* vol. 80, p. 023103, 2009.

[71] E. Lamour, C. Prigent, J. Rozet et D. Vernhet, «X-ray production in short laser pulse interaction with rare gas,» *Journal of Physics: Conference Series,* vol. 88, p. 012035, 2007.

[72] T. Caillaud, F. Blasco, C. Bonté, F. Dorchies et P. Mora, «Study of intense femtosecond laser propagation into a dense Ar gas and cluster jet,» *Phys. of Plasmas,* vol. 13, p. 033105, 2006.

[73] J. Rozet, P. Chevallier, P. Legagneux-Piquemal, A. Chetioui et C. Stephan, «Capture cross sections in highly excited p states of Ar17+ in high-velocity collisions of 250 MeV A18+ on N,» *J. Phys. B,* vol. 18, p. 943, 1985.

[74] E. Lamour, B. Gervais, J.-P. Rozet et D. Vernhet, «Production and transport of long-lifetime excited states in preequilibrium ion-solid collisions,» *Phys. Rev. A,* vol. 73, p. 042715, 2006.

[75] J. Burgdorfer et J. Gibbons, «Electron transport in the presence of a Coulomb field,» *Phys. Rev. A,* vol. 42, p. 1206, 1990.

[76] D. Arbo, C. Reinhold, P. Kurpick, S. Yoshida et J. Burgdorfer, «Quantum transport theory for atomic states through solids,» *Phys. Rev. A,* vol. 60, p. 1091, 1999.

[77] B. Gervais, C. Reinhold et J. Burgdorfer, «Simulation of excited-state formation of hydrogen in transmission of relativistic H- ions through thin foils,» *Phys. Rev. A,* vol. 53, p. 3189, 1996.

[78] D. Vernhet, J. Rozet, E. Lamour, B. Gervais, C. Fourment et L. Dubé, «Core and Rydberg state populations for HCI projectiles in solids,» *Physica Scripta,* vol. T80, p. 83, 1999.

[79] C. Reinhold, D. Arbo, J. Burgdorfer, B. Gervais, E. Lamour, D. Vernhet et J. Rozet, «Enhanced population of high-l states due to the interplay between multiple scattering and dynamical screening in ion-solid collisions,» *J. Phys. B,* vol. 33, pp. L111-L117, 2000.

[80] F. Megi, M. Belkacem, M. Bouchene, E. Suraud et G. Zwicknagel, «On the importance of damping phenomena in clusters irradiated by intense laser fields,» *Phys. Rev. A,* vol. 36, p. 273, 2003.

[81] M. Krishnamurthy, J. Jha, D. Mathur, C. Jungreuthmayer, L. Ramunno, J. Zanghellini et T. Brabec, «Ion charge state distribution in the laser-induced Coulomb explosion of argon clusters,» *J. Phys. B,* vol. 39, p. 625, 2006.

[82] C. Deiss et J. Burgdorfer, «Simulation of the dynamics of laser-cluster interaction,» *J. of Phys: conf. Series,* vol. 88, p. 012036, 2007.

[83] C. Deiss, N. Rohringer et J. Burgdorfer, «Interaction of ultra-short laser pulses with clusters: short time dynamics of a nanoplasma,» *AIP Conf. Proc.,* vol. 876, p. 143, 2006.

[84] T. Minami, C. Reinhold et J. Burgdorfer, «Quantum-trajectory Monte Carlo method for internal-state evolution of fast ions traversing amorphous solids,» *Phys. Rev. A,* vol. 67, p. 022902, 2003.

[85] C. Cohen-Tanoudji, J. Dupont-Roc et G. Grynberg, Processus d'interaction entre photons et atomes, Inter Editions/Editions du CNRS, 1988.

[86] G. Lindblad, «On the generators of quantum dynamical semigroups,» *Com. Math. Phys.,* vol. 48, p. 119, 1976.

[87] J. Dalibard, Y. Castin et K. Molmer, «Wave-function approach to dissipative processes in quantum optics,» *Phys. Rev. Lett,* vol. 68, p. 580, 1992.

[88] C. Reinhold, M. Seliger, T. Minami, S. Yoshida, J. Burgdörfer, J. Mestayer, W. Zhao, J. Lancaster et F. Dunning, «Open quantum system approach in multiple atomic collisions in solids and gases,» *J. Phys.: Conf. Series,* vol. 88, p. 012030, 2007.

[89] D. Vernhet, J. Rozet, E. Lamour, B. Gervais et L. Dubé, «Dynamical and collisional approaches to the transport of core and Rydberg projectile states in solids,» *AIP Conference proceedings,* vol. 500, p. 666, 2000.

[90] M. Seliger, C. Reinhold, T. Minami, D. Schultz, S. Yoshida, J. Burgdörfer, E. Lamour, J. Rozet et D. Vernhet, «Occupation of fine-structure states in electron capture and transport,» *Phys. Rev. A,* vol. 77, p. 042713, 2008.

[91] C. Reinhold, M. Seliger, T. Minami, D. Schultz, J. Burgdorfer, E. Lamour, J. Rozet et D. Vernhet, «Quantum and classical transport of excited states of ions,» *Nucl. Instr. and Methods B,* vol. 261, p. 125, 2007.

[92] E. Lamour, C. Prigent, J. Rozet et D. Vernhet, «Physical parameter dependence of the X-ray generation in intense laser – cluster interaction,» *Nucl. Instr. and Methods in Physics Research B,* vol. 235, p. 408, 2005.

[93] D. Vernhet, L. Adoui, J. Rozet, K. Wohrer, A. Chetioui, A. Cassimi, J. Grandin, J. Ramillon, M. Cornille et C. Stephan, «Multielectron Processes in Heavy Ion–Atom Collisions at Intermediate Velocity,» *Phys. Rev. Lett,* vol. 79, p. 3625, 1997.

[94] K. Rinn, F. Melchert et E. Salzborn, «Measurements of charge transfer in H+-He+ collisions,» *J. Phys. B,* vol. 18, p. 3783, 1985.

[95] S. Meuser, F. Melchert, S. Krüdener, A. Pfeiffer, K. von Diemar et E. Salzborn, «Crossed-beams arrangement for the investigation of charge-changing collisions between multiply charged ions,» *Rev. Sci. Instrum.,* vol. 67, p. 2752, 1996.

[96] D. Skiera, R. Trassl, K. Huber, H. Braüning, E. Salzborn, M. Keim, A. Achenbach, T. Kirchner, H. Lüdde et M. Dreizler, «Charge changing processes in collisions between Li-like ions and He2+,» *Physica Scripta,* vol. T92, p. 423, 2001.

[97] C. Chen, C. Cocke, J. Giese, F. Melchert, I. Reiser, M. Stöckli, E. Sidky et C. Lin, «Studies of charge exchange in symmetric ion–ion collisions,» *J. Phys. B,* vol. 34, p. 469, 2001.

[98] H. Braüning et E. Salzborn, *AIP Conf. Proc.,* vol. 771, p. 219, 2005.

[99] M. Chabot, D. Gardés, P. Box, J. Kiener, C. Deutsch, G. Maynard, V. André, C. Fleurier, D. Hong et K. Wohrer, «Stripping properties of a plasma medium for MeV/u chlorine ions,» *Phys. Rev. E,* vol. 51, p. 3504, 1995.

[100] A. Franck, A. Blažević, P. Grande, K. Harres, T. Heßling, D. Hoffmann, R. Knobloch-Maas, P. Kuznetsov, F. Nürnberg, A. Pelka, C. Schaumann, G. Schiwietz, A. Schökel, M. Schollmeier, D. Schumacher, J. Schütrumpf, V. Vatulin, O. Vinokurov et M. Roth, «Energy loss of argon in a laser-generated carbon plasma,» *Phys. Rev. E,* vol. 81, p. 026401, 2010.

[101] N. Tahir, V. Kim, E. Lamour, I. Lomonosov, A. Piriz, J. Rozet, T. Stöhlker, V. Sultanov et D. Vernhet, «Two-dimensional thermal simulations of an aluminum beam stripper for experiments at SPIRAL2,» *Nucl. Instr. and Methods in Physics Research B,* vol. 276, p. 66, 2012.

[102] N. Tahir, V. Kim, E. Lamour, I. Lomonosov, A. Piriz, J. Rozet, T. Stöhlker, V. Sultanov et D. Vernhet, «Two-dimensional thermal simulations of aluminum and carbon ion strippers for experiments at SPIRAL2 using the highest beam intensities,» *Nucl. Instr. and Methods in Physics Research B,* vol. 290, p. 43, 2012.

LIST OF FIGURES

LIST OF TABLES